A Search For Fast Moving Magnetic Monopoles with the MACRO Detector

Thesis by
Rongzhi Liu

In Partial Fulfillment of the Requirements
for the Degree of
Doctor of Philosophy

California Institute of Technology
Pasadena, California

1995
(Submitted on February 27, 1995)

To my wife, Hongmin

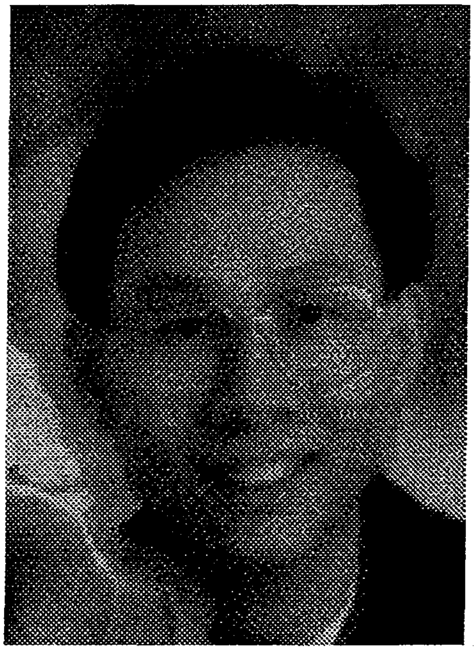

Rongzhi Liu

Born on March 3rd, 1965, in Hefei, Anhui province, in southeastern China. Enrolled in Caltech physics PhD program since summer 1989. Worked on MACRO experiment, the world's largest underground physics experiment, in central Italy.

Acknowledgments

The world has changed, and so has China. When I was a pupil in an elementary school in the southeastern China countryside, I could never have thought that one day I could come to the United States to learn physics under the guidance of world class scientists. I could never have dreamed that my wife would accompany me all the way from China to the US and to Italy—where we spent one year in an isolated but beautiful mountain area doing the magnetic monopole experiment which was interesting to me but made less sense to her. I owe her many thanks for the rest of my life. I also appreciate my parents and my brothers for their support during our family's hard time in the 1970's because of the "Cultural Revolution."

I feel that I am extremely fortunate to have been taken as a graduate student by my advisor, Dr. Barry C. Barish, who not only is an outstanding physicist but also has a style which would make many students love to work for him. His profound understanding of modern physics principles and his commitment and leadership in research have greatly influenced me. I thank him for his more than five years of generous support.

Born in a typical China countryside, I was educated in classical Chinese culture. One of the Chinese philosophies of thinking is that some things cannot be explained and do not need to be explained; instead, one, as a learner, has to experience them himself. I have to confess that I have been educated that way, and this became quite significant after I came to Caltech. However, I feel that I have been changing since then. I have been changing to a more scientific way—a way which explains and describes things more precisely. Among many teachers, Dr. Charles W. Peck is the one to influence me most. He is the most excellent teacher I have ever met. He used his outstanding professional knowledge to teach me in detail how to do experiments, to pick up physics, and even to drink a good wine. In addition, he spent a lot of his precious time teaching me how to write good English. I cannot appreciate his kindness more.

I am grateful to be a student at Caltech where we have a very good group and got much attention from senior people as well as each other. I would like to thank Dr. Gary Liu who helped me in many ways including teaching me how to live in this nation. I would thank D. Michael, N. Longley, K. Scholberg, R. Nolty, S. Mrenna, C. Walter, N. Pignatano, E. Katsavounidis, S. Kyriazopoulou, and the whole MACRO collaboration listed in Appendix C; especially Dr. N. Longley, K. Scholberg, R. Nolty, and Dr. J. Hong who made many comments on my thesis. I also thank Dr. G. Tarlé and his group at the University of Michigan where the ERP trigger system was designed and developed.

Five and half years at Caltech is not a short time compared with the lifetime of a human being. However, it appears short because of many happy things and memories. I enjoyed having many friends and enjoyed many activities organized by the Caltech Chinese community. I would like to thank all of them and wish them my best.

Abstract

From Dirac monopole theory to modern GUT's (Grand Unified Theories), magnetic monopoles have attracted much attention from physicists. While Dirac had demonstrated the consistency of magnetic monopoles with quantum eletrodynamics, 't Hooft and Polyakov demonstrated the necessity of monopoles in GUT's. Furthermore, the GUT's supply more clues about magnetic monopoles, including their exceptionally heavy masses $\sim 10^{16}$ GeV. Both current theories and previous monopole experiments have suggested that the flux of magnetic monopoles is likely to be very small, so it is necessary to have a large area detector to search for them. This thesis presents a search for fast moving magnetic monopoles with the MACRO detector.

The MACRO detector is a large underground detector located at Gran Sasso, Italy. Its primary goal is to search for magnetic monopoles at a flux level beyond the Parker bound. It is underground at 3,000 meters water equivalent depth, with a nominal acceptance of 10,000 m^2 sr. It employs liquid scintillator counters, streamer tubes and track-etch detectors which can supply both independent and cross checks for fast monopole candidate events.

This search is mainly based on the liquid scintillator counters with primary event selection and energy reconstruction from the ERP system. The 6.2 μs trigger time is based on the time of flight of a fast moving monopole diagonally through one supermodule with a velocity $\sim 10^{-2}c$. The search uses the "six-month-run" data which were taken from December of 1992 to July of 1993 with the operation of the lower part of the detector. With energy reconstruction ability up to 8 GeV with 22% error, we apply a double-face high energy requirement to reject most muon events from the data sample. We then apply the WFD, streamer tube and strip information to reject non-monopole events.

The live time for this analysis is 5,300 hours, with acceptance of 4050 m^2 sr. With no fast monopole candidate event found, we establish an upper flux limit for the fast moving magnetic monopole at 90% confidence level of 3.03×10^{-15} $\text{cm}^{-2}\text{sr}^{-1}\text{s}^{-1}$ for velocities from $10^{-2}c$ to $1.0c$.

Contents

List of Tables

List of Figures

Chapter 1

Introduction

Five thousand years ago, when the Emperor called Huang led his tribesmen into battle against a neighboring tribe in today's central China, his advances were checked by a heavy fog which hid his enemy and disorganized his army. Emperor Huang was desperate for a breakthrough until he found a magic stone which always pointed to the south. He placed this magic stone inside a chariot and led his army to victory. Aided by the stone, he conquered many tribes and eventually unified central China in the Yellow River region. This magic stone was called the "magnetic stone," and was written into Chinese history more than 3,500 years ago. Since then, human beings have found many applications of magnets.

One of the most productive uses of the magnet is to generate electricity. This followed the discovery of the connection between electric current and magnetic field by Oersted [1] as later formulated by Ampere [2] in his famous Ampere's law. A picture of a magnet is always drawn with two nonseparable poles regardless of the fact that magnetic monopoles are formally permitted by physics theory. As every college freshman has been taught in an introductory physics course, the normal Maxwell's equations are formulated under the assumption that there is no isolated magnetic monopole. Magnetic monopoles were generally ignored until Dirac published his paper in 1931 [3]. Since then, many physicists have worked on the problem of finding magnetic monopoles and understanding their origins. So far, all searches have been fruitless. Even now in the 1990's, people are still puzzled by the lack of evidence for magnetic monopoles and work to prove their existence. With the guidance of modern physics theory and technology, a group of people including this author have labored in a deep underground tunnel in central Italy trying to find any evidence for the existence of magnetic monopoles. This thesis describes a search for fast moving magnetic monopoles with the MACRO experiment, the largest underground physics experiment in the world, based on the technology of liquid scintillator and streamer tubes.

1.1 Dirac Monopoles

For centuries, physicists have felt very strongly that magnetic monopoles could exist. One reason is the symmetry between electricity and magnetism which suggests the existence of isolated magnetic monopoles should be true like the existence of positive and negative electrical charge particles. In 1931, P. A. Dirac [3] published a paper in which he put forward an argument for the existence of magnetic monopoles for the first time based on quantum physics theory.

Dirac used a fundamental quantum physics conclusion that *the change in phase of a wave function around any closed curve must be the same for all wave functions, and it must be an arbitrary integral multiple of* 2π. This leads to the quantization of the total flux of magnetic field crossing a small closed surface, and further leads to the magnetic monopole quantization condition:

$$g_m e = \frac{n}{2}, \tag{1.1}$$

where e = electron charge,

g_m = magnetic monopole charge, and

n = is any integer such as ± 1, ± 2 ...

Here we use the Gaussian unit system with the additional simplification that of $\hbar = c = 1$; the fine structure constant is thus $\alpha = e^2$ in this system.

Dirac pointed out that this result could have two different interpretations. On one hand, it indicates that the theory allows isolated magnetic monopoles and the strength of such monopoles must be quantized with the quantum $g_D = e/2\alpha$. On the other hand, it indicates that electric charge must be quantized if there is even a single monopole in the entire universe. The observed phenomenon that the electric charge can only be some integral multiple of the electron charge e supports the conclusion that magnetic monopoles must exist. It should be pointed out that the fractional charge of quarks is consistent with Dirac's conclusion because quarks are confined [4]. Further, as reference [4] has pointed out, in correspondence to the theory of quantum chromodynamics (QCD) which indicates that quarks have color charge, the magnetic monopole should also have color charge.*

Dirac envisaged a magnetic monopole as a semi-infinitely long, infinitesimally thin solenoid, but he did not indicate any other characteristics for magnetic monopoles such as mass, spin, structure, possible sources, or the flux of magnetic monopoles in cosmic rays.

1.2 Grand Unified Theory and Monopoles

Physicists have dreamed of a unified theory which can explain all four fundamental interactions: strong, weak, electromagnetic, and gravitational (Table 1.1). The

---

*As J. Preskill pointed out, the "color magnetic field" of the monopole would become screened by the nonperturbative strong-interaction effects at distances greater than 10^{-13} cm.

success of the GSW (S. Glashow, A. Salam, S. Weinberg) model of electro-weak interactions has helped to encourage more efforts toward this grand unification. An exceptional discovery by 't Hooft [5] and Polyakov [6] not only demonstrates the existence of the magnetic monopole as a natural result of most GUT's (Grand Unified Theories) but also predicts many properties of these magnetic monopoles which were not determined in Dirac's theory. In this section we give an overview of GUT's and discuss briefly GUT monopoles. An excellent review of the monopole theory given by J. Preskill can be found in reference [4].

Interaction	Strong	Electromagnetic	Weak	Gravitational
Coupling constant dimensionless	1	1/137	1.02×10^{-6}	0.53×10^{-38}
Range (m)	$\leq 10^{-15}$	∞	10^{-18}	∞
Source	"Color charge"	Electric charge	"Weak charge"	Mass
Typical cross-section (m^2)	10^{-30}	10^{-33}	10^{-44}	—
Typical lifetime of decay (s)	10^{-23}	10^{-20}	10^{-8}	—

Table 1.1: The four fundamental interactions. The typical cross-sections are calculated at 1 GeV. The table is from reference [7].

1.2.1 Grand Unified Theory

One of the profound insights in understanding the unification of different interactions is the principle of gauge symmetry. Using gauge symmetry, physicists successfully combine the electromagnetic interaction and the weak interaction into a single interaction: the electro-weak interaction or GSW model. It, together with the QCD strong interaction model, composes the "standard model" of particle physics. The success of the standard model inclines more people to believe that the dream of unification of all four known physics interactions may come true.

The current goal of a Grand Unified Theory, or GUT, is the unification of the electro-weak and strong interactions within one grand unified group[†] G. This group G must include the subgroups of all three interactions.

$$G \supset SU(3)_C \otimes SU(2)_L \otimes U(1)_Y, \tag{1.2}$$

where $SU(3)_C$ is the group describing the strong interaction, and $SU(2)_L$ and $U(1)_Y$ are the groups of the unified electro-weak theory.

Above some mass scale, M_{GUT}, there is only one gauge interaction described by group G, and, hence, only one gauge coupling α_G. Below M_{GUT}, the gauge symmetry could be dynamical breaking into different subgroup symmetries at different energy scales, where the *effective* coupling constant for each interaction will be different. Figure 1.1 shows how the coupling constants change with Q, the mass scale.

Many GUT's with different symmetry groups have been attempted; none of them, however, is completely successful. As particular, the most simplest unifying gauge group $SU(5)$ predicts proton decay at a rate that has been excluded experimentally.

1.2.2 GUT Monopoles

In 1974, 't Hooft [5] and Polyakov [6] independently discovered that magnetic monopoles exist as solutions of gauge symmetry breaking in many nonabelian gauge

---

[†] It is difficult to create a unified theory which includes the gravitational force because it is by far the weakest and has no measurable quantum effect to guide us to a quantum theory.

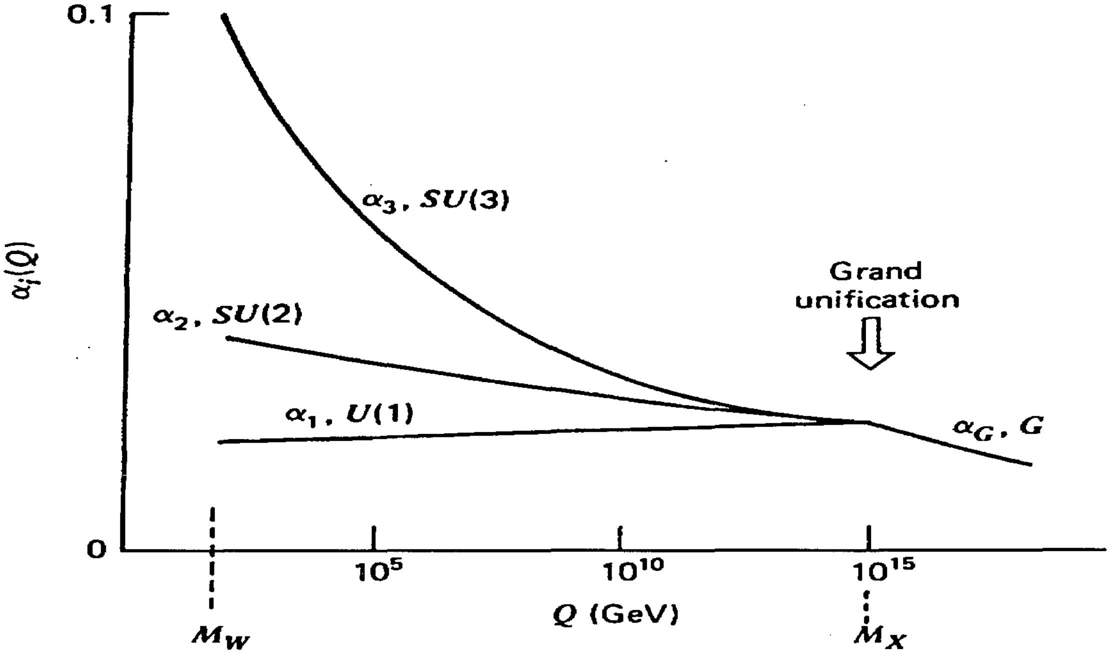

Figure 1.1: The variation of the coupling constants with the characteristic momentum Q, showing the speculative grand unification of the strong [SU(3)] and the electro-weak [$SU(2)\otimes U(1)$] interactions, where the M_w is the mass of charged bosons which mediate the weak interaction, M_x is the grand unification mass, and α_1, α_2, α_3 are the coupling constants of electromagnetic, weak, and strong interactions. α_G is the coupling constant at the unification energy. This picture is reprinted from reference [8].

theories (including GUT's). All grand unified theories possess a large group of exact gauge symmetries that mix the strong and electro-weak interactions, but these symmetries become spontaneously broken at an exceedingly short distance scale M_x^{-1} (or, equivalently, an exceedingly large mass M_x). They demonstrated that as a simple nonabelian group is broken to give $U(1)$ at low energy, the field equations yield a solution for magnetic monopoles. The properties of the magnetic monopole are determined by the distance scale of the spontaneously symmetry breaking.

In contrast to the fact that the monopole mass must be regarded as an arbitrary free parameter in Dirac's theory, the GUT monopole mass is calculable in a given unified model. Different GUT's will give slightly different values of M_x. From the electromagnetic coupling constant $\alpha_{em} \approx 1/137$ which is related to α_x according to the symmetry breaking theorem and the "desert hypothesis," [‡] the GUT energy scale M_x is estimated to be about 10^{14} GeV, for which the mass of GUT magnetic monopoles is $\sim 10^{16}$ GeV.

$$\text{Charge}: \quad g = g_D, \tag{1.3}$$

$$\text{Mass}: \quad M_g \approx \frac{M_x}{\alpha_x} \approx 10^{16}\ \text{GeV}, \tag{1.4}$$

$$\text{Core size}: \quad R \approx {M_x}^{-1} \approx 10^{-28}\ \text{cm}, \tag{1.5}$$

where M_x = grand unification energy scale, and

α_x = coupling constant at grand unification scale.

Most of the monopole mass is concentrated in its tiny core of radius M_x^{-1}, but it has interesting structure on many different size scales. At distances less than $\sim 10^{-16}$ cm from the center of the monopole, virtual W and Z bosons have important effects on its interactions with other particles. As we mentioned early, the color magnetic field will be screened by nonperturbative strong interaction effects beyond the distances of 10^{-13} cm from the center. And, because of its large magnetic charge, the monopole is strongly coupled to a surrounding cloud of virtual electron-positron pairs, which extends out to distances of about 10^{-11} cm from the center [4, 9].

It is believed that magnetic monopoles may carry electric charge in addition to their magnetic charge, simply because monopoles have a large electromagnetic interaction with electrical charged particles. These monopoles with electric charges are called *dyons*. It is not obvious whether magnetic monopoles in nature should be dyons or not; if monopoles did carry electric charge, however, it would slightly affect some

---

[‡] The "Desert hypothesis" assumes that no unexpected new interactions or particles appear between present-day energies (of order 100 GeV) and the unification scale M_x.

experimental searches, such as the mica searches, which we will discuss later.

The core of the GUT magnetic monopole contains grand unified gauge and Higgs fields, where most grand unified theories predict that the baryon number is not conserved [10, 11]. Several authors have argued, moreover, that interactions between fermions and GUT monopoles are independent of the unification scale, M_x, and in fact independent of the typical strong interaction strength [11, 12]. For example, a proton in the vicinity of a GUT monopole could decay; this process is called monopole-catalyzed proton decay. A typical monopole-catalyzed proton decay reaction is:

$$g_m + p \rightarrow g_m + e^+ + \pi^0. \tag{1.6}$$

The monopole-catalyzed decay could be used as a signature for the detection of GUT monopoles in some searches although this is a controversial subject because the expected behavior is strongly model dependent.

1.3 Monopoles and Astrophysics

Because the GUT monopole mass is so large, it is impossible to artificially produce one via current experimental methods. In fact, the only possibility of producing GUT monopoles is during the very early ($t \sim 10^{-34}$ s) epoch of the big bang.[§] The big bang theory holds that the universe was once extremely hot and small, so hot that processes occurred that were sufficiently energetic to produce monopoles. This connection relates GUT monopoles to cosmology and astrophysics. Figure 1.2 shows the history of the universe according the big bang theory, with the very hot epoch of the universe at the beginning.

[§] The Big Bang Model is also called the standard model of cosmology.

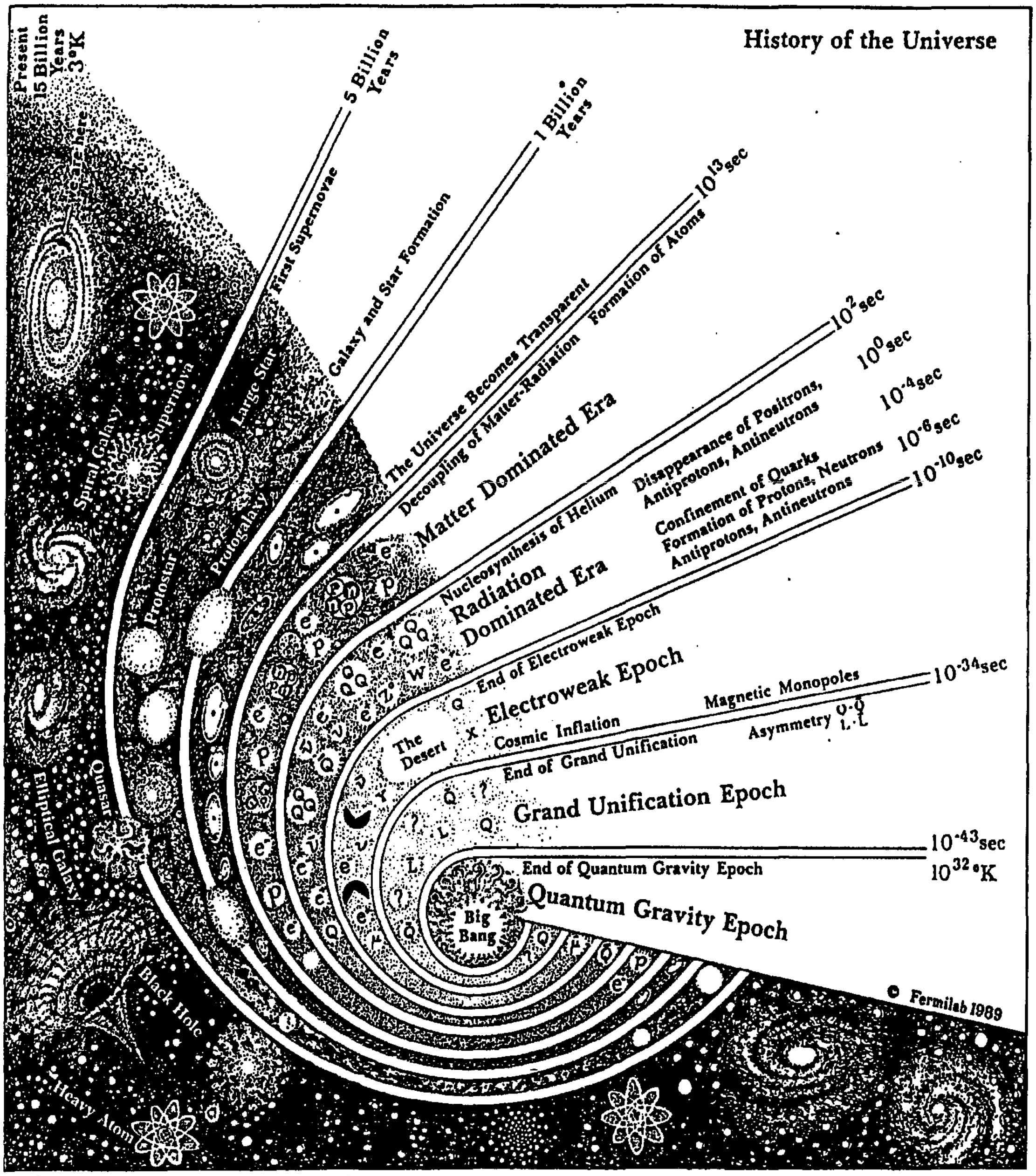

Figure 1.2: The history of the universe according the big bang theory. GUT monopoles can only be created at 10^{-34} s during the early epoch of the big bang universe. This picture is reprinted from the Fermilab poster.

1.3.1 The Density of GUT Monopoles

To estimate the density and flux of magnetic monopoles, we must understand their production, acceleration mechanism, gravitational dynamics, magnetic field, *etc.* These questions have no definite answers; we can still, however, work out some constraints on the flux from our present knowledge of cosmology and astrophysics.

Cosmology

In big bang cosmology, GUT monopoles are produced at the phase transition [13] where the unifying gauge symmetry breaks down to $SU(3) \otimes [SU(2) \otimes U(1)]$, which takes place at the critical temperature $T_c \sim M_x/\alpha$ ($\sim 10^{16}$ GeV). Monopole production was roughly one within each event horizon,¶ which produces too many monopoles to be consistent with the mass of the universe. The only way of decreasing the number of monopoles is via annihilation of monopole anti-monopole, but this rate is very small [15, 14]. Various attempts have been made to resolve this conflict. Among them, the inflationary universe scenario [16, 17] is the most appealing resolution. If there is a period in the early universe during which the universe expands exponentially as a function of time, then the GUT monopole density is diluted by a tremendous factor, which is, unfortunately, impossible to be predicted accurately.

The Mass of Universe

The most straightforward astrophysical limit on the magnetic monopole density comes from the assumption that GUT magnetic monopoles account for most of the mass of the universe [18]. With the mass density in galaxies estimated to be about $0.02\rho_c$, where ρ_c is the critical density to close the universe, the monopole density

---

¶The event horizon is at the distance a light pulse could have traveled since the initial singularity of the big bang.

is then:

$$n_m \sim 4 \times 10^{-20}\mathrm{cm}^{-3}, \quad \text{or} \tag{1.7}$$

$$\frac{n_m}{n_N} \leq 10^{-14} \tag{1.8}$$

where n_m and n_N are the density of monopoles and nucleons, respectively. If GUT magnetic monopoles account for the total dark mass of the universe (about $0.98\rho_c$), the monopole density is then about two orders of magnitude larger than the above result.

1.3.2 The Flux of GUT Monopoles

Because GUT monopoles are produced in the very beginning of the big bang universe, they must interact with other particles during the formation of the galaxy and other objects. Although cosmology and astrophysics do not offer definite answers, general arguments are still used to place severe limits on the velocity and the flux of monopoles in the cosmic rays.

Monopole Velocity

As a relic gas of the big bang, GUT monopoles should have cooled down to 10^{-8} K which implies a velocity of less than $10^{-21}c$. However, the existing magnetic fields and gravitational forces of the earth, solar system, and galaxy can accelerate monopoles to their escape velocities [20], which are listed in Table 1.2.

The escape velocities for Dirac monopoles are the same as those for GUT monopoles or any other object. These velocities indicate that monopoles in the cosmic radiation arrive with very low speed ($v < 10^{-2}c$); there exist, however, very strong magnetic fields surrounding objects [21] as neutron stars, pulsars, and black holes, where

Astronomical Object	Escape velocity
Earth-type planets	$v < 4 \times 10^{-5}c$
The sun and similar stellar systems	$v \approx 10^{-4}c$
The Galaxy or local supercluster	$v \approx 10^{-3}c$
Velocity expected for extragalatic sources	$v > 10^{-3}c$

Table 1.2: List of possible GUT monopole velocities in universe.

GUT magnetic monopoles could be accelerated to relativistic velocities ($v \sim c$) [22]. Since the population of these objects is small, the GUT monopole flux from them is expected to be much less than the Parker bound, which will be explained shortly.

Unlike GUT monopoles which are expected to be supermassive, light Dirac magnetic monopoles could be accelerated by the galactic magnetic field to escape velocity in a much shorter period. Obviously, Dirac monopoles can be accelerated up to near the speed of light by neutron stars, pulsars, white dwarfs, *etc.*

Parker Bound

A simple estimation of the flux of GUT monopoles is to account the monopole for the mass of galaxy and with galactic escape velocity ($10^{-3}c$). With the density discussed in Equation 1.8, we obtain a flux limit:

$$F_g \leq 5.4 \times 10^{-16}\mathrm{cm}^{-2}\mathrm{sr}^{-1}\mathrm{s}^{-1}\mathrm{m}_{17}{}^{-1}[\frac{v}{10^{-3}c}], \qquad (1.9)$$

where $m_{17} = m/(10^{17}\ \mathrm{GeV})$, and

$v =$ velocity of GUT monopoles.

A more interesting result has been obtained by the consideration of the survival of the galactic magnetic field by E. N. Parker *et al.* [19]. The idea is the following: monopoles moving through a magnetic field cause dissipation of the field energy at a rate equal to $\vec{j_m} \bullet \vec{B}$. If we assume that the galactic field can be regenerated by the motions of the interstellar gas, we can obtain a flux limit using the current known galactic field ($\sim 3 \times 10^{-6}$ gauss):

$$F_g < 10^{-15}\mathrm{cm}^{-2}\ \mathrm{sr}^{-1}\ \mathrm{s}^{-1}. \tag{1.10}$$

However, taking into account that monopoles are isotropically distributed, Parker *et al.* reexamined the energy dissipation due to each monopole using the monopole mass and velocity distributions. They obtained a flux limit of:

$$F_g \leq \begin{cases} m_{17} v_3 10^{-15}\mathrm{cm}^{-2}\mathrm{sr}^{-1}\mathrm{s}^{-1}, & \text{if } \ v \geq v_{mag}, \\ 10^{-15}\mathrm{cm}^{-2}\mathrm{sr}^{-1}\mathrm{s}^{-1}, & \text{if } \ v \leq v_{mag}, \end{cases} \tag{1.11}$$

where $m_{17} = m_g/10^{17}$ GeV, and where m_g is the mass of a monopole,
$v_3 = v/(10^{-3}\ c)$ where v is the monopole velocity, and
v_{mag} = the velocity a magnetic monopole which is initially at rest would acquire by magnetic acceleration through a coherent region (of order 10^{21} cm) of the magnetic field.

1.4 Previous Monopole Experiments

The induction technique, which detects the current induced by magnetic monopoles in a conducting ring, is an attractive method for monopole detection. It is a pure magnetic monopole effect [23]; thus, it is sensitive to both Dirac and GUT magnetic monopoles of any velocity. However, it is almost impossible to build a large area detector with this technology at reasonable cost. On the other hand, because the energy loss for fast moving monopoles ($v > 10^{-2}c$) is so large, ($dE/dX >$ 1 GeV/(g/cm^2)), they can be detected by scintillators and gaseous detectors such as streamer tubes and multiwire proportional chambers. Some new materials such as CR-39 and Lexan have been adopted for the detection of monopoles, and are believed to be sensitive to fast moving magnetic monopoles of either GUT or Dirac types.

Some other experimental methods differ for GUT and Dirac monopoles because of the large mass of GUT monopoles. For example, many experiments based on accelerators are irrelevant to GUT monopoles. Searches for magnetic monopoles in bulk materials, especially in ferromagnetic and lunar [24] materials have also been performed, but such searches are hardly relevant to GUT monopoles because GUT monopoles are unlikely to be trapped by the earth or the moon. Ancient micas are used for GUT monopoles searches because mica is believed to be sensitive to GUT monopoles with slow velocities, but, consequently, they are irrelevant to Dirac monopoles.

1.4.1 Accelerator Experiments

Accelerator searches [25, 26, 27] for Dirac monopoles are based on the following interactions:

$$p + \bar{p} \rightarrow g_m + \bar{g}_m, \tag{1.12}$$

$$p + \bar{p} \rightarrow g_m + \bar{g}_m + X, \tag{1.13}$$

$$e^- + e^+ \rightarrow g_m + \bar{g}_m, \quad \text{and} \tag{1.14}$$

$$e^- + e^+ \rightarrow g_m + \bar{g}_m + X, \tag{1.15}$$

where g_m and $\bar{g}_m$ represent monopoles and anti-monopoles, and X represents other charged particles with a total of zero charge. These searches have been performed in both e^+e^- colliders and $p\bar{p}$ colliders. The usual spectrometers based on ionization or excitation due to electrically charged particles are used for magnetic monopole detection in these experiments, and some also use track-etch detectors at the center of the apparatus such as MODEL [27] at LEP.

Searches with accelerators are only valid for a monopole mass less than the half of center of mass energy of the collider. For instance, the mass limit for monopole searches at the LEP e^+e^- storage ring is less than 44.9 GeV as the total center of mass energy is 91 GeV. No magnetic monopoles have been found in any of these experiments. Clearly, these searches are only meaningful for Dirac monopoles because their mass could be light.

1.4.2 Induction Experiments

As mentioned above, the induction technique is sensitive to monopoles at any velocity with any mass as long as the monopole still carries a magnetic charge of at least $g_D = e/2\alpha$. A monopole will induce a predictable current, an eddy current, when it passes through a conducting loop.

Several experiments [28, 29, 30] with superconducting rings have been developed to search for monopoles. There are two advantages to this low temperature superconducting technology. One is that the induced current can last much longer, and hence it can be measured more easily. The other is that the signal-to-noise ratio can be higher at lower temperature. A very sensitive device, called a SQUID (superconducting quantum interference device), is used to help to demonstrate that the induced current is quantized and agrees with the expected value for magnetic monopoles.

Because of the low temperatures required by superconducting rings, however, it is hard to make a large area detector based on this technique, and this limits their ability to set low flux limits. The present global-combined upper limit from induction experiments is 2.2×10^{-13} cm^{-2}sr^{-1}s^{-1} [32], which is well above the Parker bound.

1.4.3 Ionization Experiments

Magnetically charged particles, like electrically charged particles, will lose energy when traversing material. For fast moving monopoles, this energy loss is largely due to their magnetic charge. Energy loss via ionization can be detected with conventional detectors such as scintillator and gaseous detectors, which are important after the theoretical verification [33, 34] that they could be sensitive to low velocity monopoles. A great advantage of these techniques, compared with the superconducting induction detectors, is that a large area detector can be built with much less cost. For GUT monopoles in the cosmic radiation, a large area detector is important because the astrophysical flux limit of GUT monopoles is expected to be very small.

Scintillator Detector

As we will discuss in Chapter 4, the energy loss of magnetic monopoles in scintillator is very large for fast moving ($v > 10^{-2}c$) monopoles while it is very small for slow moving ($v < 10^{-3}c$) monopoles. Thus, it is easier to detect fast moving monopoles, but it is also possible to detect slow monopoles with specially designed trigger systems.

Many scintillator detectors [35, 36, 38, 37, 39, 40] have been developed to search for magnetic monopoles. Among them, the Baksan experiment has operated for more than ten years. This detector is located 850 m w. e. d. (water equivalent depth) underground in the Baksan mountains. The detector is 16 m$\times$16 m$\times$11 m, with four layers of liquid scintillator. Each layer consist of a 20$\times$20 array of scintillator counters with dimensions 70 cm$\times$70 cm$\times$30 cm. At the end of 1993, the Baksan experiment had set an upper limit of 4×10^{-16} cm^{-2}sr^{-1}s^{-1} [41] at 90% c.l. for monopoles velocities between $10^{-3}c$ and $10^{-1}c$.

Gaseous Detector

Measuring the ionization loss of magnetic monopoles is also practical for many gaseous detectors such as streamer tubes and multiwire proportional chambers. Since the ionization energy loss of magnetic monopoles has been theoretically much better modeled in the last ten years, it is now believed possible for proportional chambers to measure directly the energy loss for monopoles at velocities larger than $10^{-2}c$. Drell *et al.* [33] have additionally presented the calculation of magnetic monopole energy loss in atomic hydrogen and helium for velocities less than $10^{-3}c$.

Several groups [42, 43, 44] use gaseous detectors for monopole searches. Among them, the Soudan 2 detector, which is an underground (2,100 m w. e. d.) tracking calorimeter using Ar$-$CO$_2$ gas, was originally built to detect nucleon decays, but can also observe traversing magnetic monopoles. The upper limit from the Soudan 2 experiment [42] is 8.7×10^{-15} cm^{-2}sr^{-1}s^{-1} for $\beta > 2 \times 10^{-3}$.

1.4.4 Track-etch Experiments

Some materials, especially transparent solid materials, record the passage of charged particles by means of the formation of submicroscopic damage trails tens of angstroms in diameter. Such damage trails can be amplified by chemical etching [45] and seen under a microscope. The size of the trail depends upon the nuclear and electric stopping power of the traversing particles. Three materials are commonly used for monopole detection: mica, CR-39, and Lexan. For the expected monopole energy deposition, mica is believed to be sensitive only to monopoles that have captured nuclei, Lexan is believed to be sensitive to monopoles with velocities greater than $\sim 0.3c$, and CR-39 is believed to be sensitive to monopoles with velocities greater than $10^{-4}c$.

CR-39

CR-39 is a plastic material widely used for optical lenses such as eye glasses. It is sensitive to monopoles in a wide velocity region. The majority of CR-39 calibrations performed with heavy ions show that it should be sensitive to fast moving monopoles at $\beta > 10^{-4}$, although the measurements for low β response of CR-39 from Snowden-Ifft and Price [46] show that there is some insensitivity at β around 10^{-3}. Members of the MACRO collaboration at Bologna University in Italy, on the other hand, have also performed a CR-39 calibration with low β ions. Their results show that CR-39 is sensitive to all β down to 10^{-4} which is inconsistent with Price's results [45].

Several groups use CR-39 for fast moving monopole searches [47, 48, 49]. The best flux limit so far achieved is by Orito *et al.* [49], who used a 2,000 m^2 array of CR-39 track-etch detectors underground at a depth of 100 m w. e. d. In 2.1 years of operation, they found no monopole event, for a flux limit of $3.2 \times 10^{-16}\ \mathrm{cm}^{-2}\mathrm{sr}^{-1}\mathrm{s}^{-1}$ for monopole velocities greater than $4 \times 10^{-2}c$.

MICA

Unlike CR-39 and other organic polymers, damage to the structure of mica is caused by a particle's nuclear stopping power. This fact makes mica much less sensitive to fast moving particles than CR-39, and the nuclear stopping power of magnetic monopoles would not be strong enough to produce tracks unless the monopoles have captured nuclei.

The fact that mica is only sensitive to monopoles with captured nuclei makes searches based on it less encompassing, although it is still useful for GUT monopoles because they are expected to have the slow velocities and are required to capture nuclei. In addition, micas were formed $10^8 - 10^9$ years ago, and so have extremely long exposure times which allows mica to play an important role [50, 51, 20] in magnetic monopole searches in the low velocity regime. It is almost certain, however, that mica is not sensitive to fast moving magnetic monopoles.

1.4.5 Monopole Captured Proton Decay

Some experiments search for GUT monopole-catalyzed proton decays. These experiments are irrelevant to Dirac monopoles and are sensitive only to slow moving GUT monopoles because of the probability of GUT monopole catalyzed proton decay is proportional to $1/v$. Several groups are using this technique to search for GUT monopoles in detectors such as water Cerenkov detectors. For a review, see reference [20].

1.5 Summary

While Dirac merely demonstrated that the existence of magnetic monopoles could explain electrical charge quantization, modern GUT's actually predict their existence. Both give the same magnetic charge, but GUT's suggest many other features of magnetic monopoles as well. As a very general consequence of the unification of the fundamental interactions, GUT magnetic monopoles tied to many physics topics from particle physics to cosmology and astrophysics. Any evidence for the existence of magnetic monopoles will have a great impact with modern physics. Particularly, the detection of GUT magnetic monopoles with extremely heavy mass (10^{16} GeV) would confirm a fundamental prediction of grand unification as well as provide a solid evidence to support big bang cosmology. The measurement of a flux of magnetic monopoles would also put severe constraints on the cosmological model building and could also solve, or at least partly solve, the dark matter mystery which is one of the most interesting contemporary physics topics.

GUT monopoles with expected superheavy masses (10^{16} GeV) could only be produced in the early epoch of the big bang universe. It is practical to search for GUT monopoles in the cosmic radiation rather than in bulk materials because they are unlikely to be trapped by the earth. Although the cosmic radiation is not very well understood, and neither is the origin of the universe, it is clear that the flux of magnetic monopoles is very small. Therefore, it is necessary to have a large area detector to search for them. The MACRO experiment, designed specially to search for magnetic monopoles, is such a detector.

Chapter 2

The MACRO Experiment

In this chapter, we will describe the apparatus of the MACRO detector, its location, and its components. Since the scintillator system plays the major role in monopole detection, we will describe it in detail: the liquid scintillator, the photomultiplier tubes (PMT's), the PMT gain setting, and the MACRO calibration system. We will briefly discuss the streamer tube system, for which more details can be found in reference [52]. We will also briefly discuss the other physics objectives of the MACRO experiment.

2.1 General Information About the Gran Sasso Laboratory

MACRO (Monopole **A**strophysics and **C**osmic **R**ay **O**bservatory) is located just off a roadway in the Abruzzo province of central Italy, where highway A14 from Rome to the east coast passes beneath the Gran Sasso, the "Great Rock" (Figure 2.1). In the center of this mountain, about 110 kilometers northeast of Rome, three large experimental halls were built. They comprise the Gran Sasso underground laboratory [54]. Figure 2.2 shows the layout, where the MACRO experiment occupies Hall B.

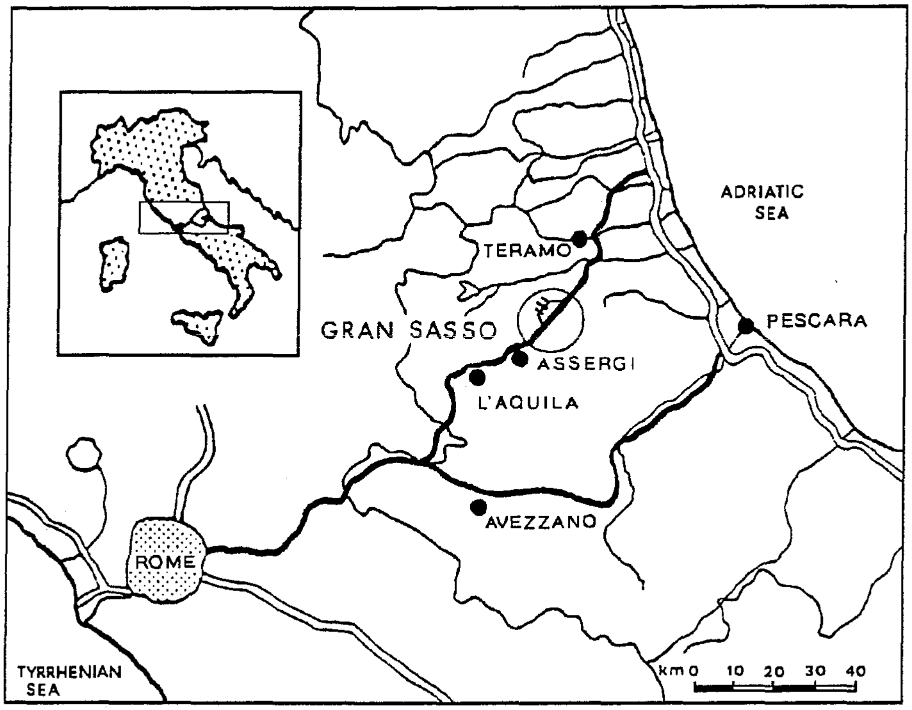

Figure 2.1: Geographical map of central Italy. The circle near the city of Assergi indicates the underground tunnel area. Inside the circle is shown the location of the Gran Sasso underground Laboratory [53].

The geographical coordinates of the Gran Sasso Laboratory are 13°34′28″ E longitude and 42°27′09″ N latitude. The floor of the laboratory is 963 meters above sea level. The mountains provide an excellent shield for the MACRO detector at about 3,200 meters w. e. d. (water equivalent depth), reducing the surface muon flux by a factor of 10^6. The average rock density above the Gran Sasso Laboratory is (2.71 ± 0.04) g/cm^3, consisting of Ca(27%), O(51%), C(12%), Mg(8%), Si(1%), and less than 1% of Al, K, and H. The minimum energy required for a muon to penetrate the rock to the MACRO detector is approximately 1.2 TeV.

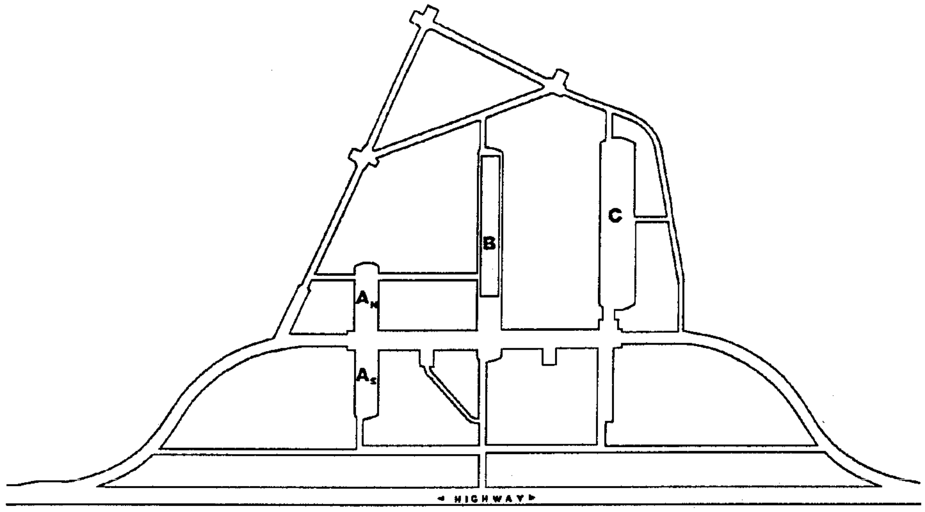

Figure 2.2: The layout of the Gran Sasso underground laboratory. One of the twin roadway tunnels and the three underground Halls (A, B, and C) are shown. MACRO is represented by the rectangle in Hall B [53].

2.2 The MACRO Detector

The MACRO detector is 77 meters long, 12 meters wide and 9 meters high. It consists of six independent "supermodules" placed side by side from the north to the south, shown in Figure 2.3. The six supermodules (SM's) are identical in structure except that SM1 and SM6 have north and south faces, respectively, on their lower parts. The six supermodules are instrumented and operated in three pairs in order to allow for the continuous operation of part of the detector while others may be undergoing calibration.

The upper and lower parts of the detector are constructed differently. The lower part is about five meters high. Figure 2.4 shows a cross-sectional end view of the lower

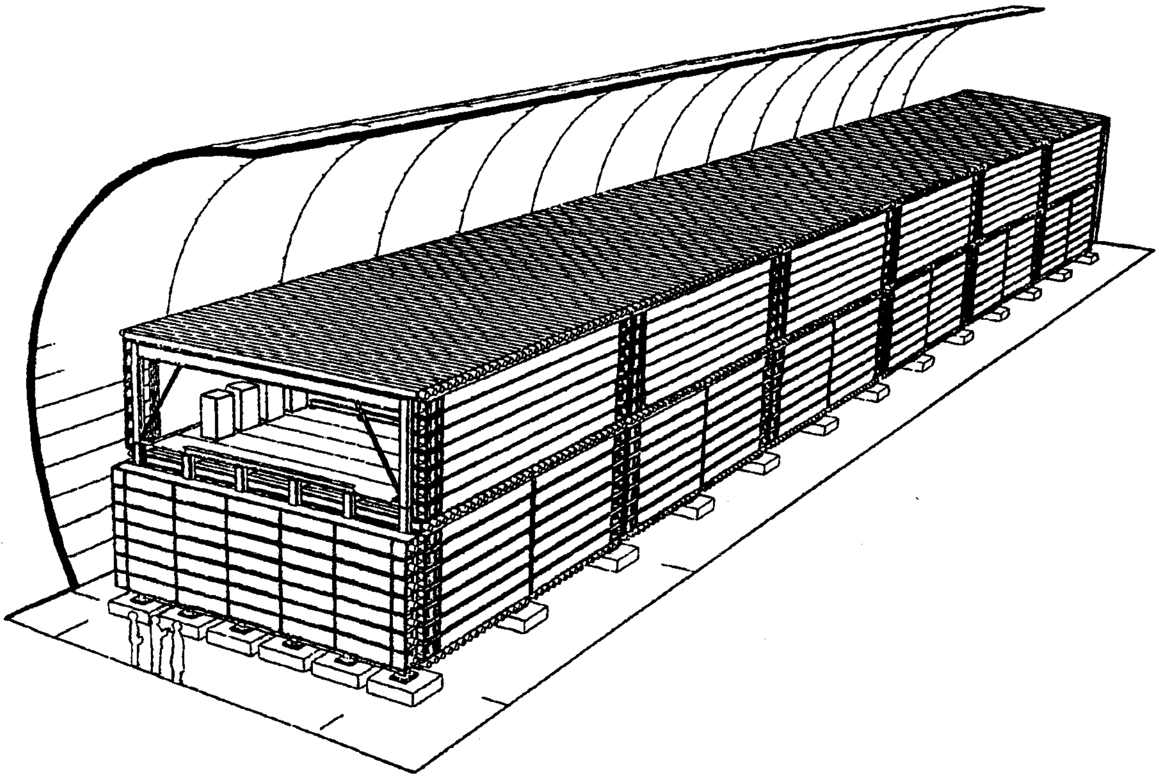

Figure 2.3: The full MACRO detector with six SM's and attico [52].

part of one SM, made up of two modules, each with area of 6 m×12 m×5 m. Between the two modules there is a gap of 30 cm occupied by the supporting structure of the apparatus. The lower part of one SM consists of two horizontal layers (center and bottom) and vertical layers (west, east) of scintillator counters (also called scintillator tanks). The geometry of a horizontal tank is different from that of a vertical one, as will be described later. Each layer of the horizontal tanks is sandwiched between two planes of limited streamer tubes. There are also six more horizontal layers of streamer tubes in between the two scintillator layers, for a total of ten planes. The eight inner planes are separated by seven layers of crushed rock absorbers, each 32 cm thick. The absorbers set the minimum energy threshold at about 1.5 GeV for a vertical muon crossing the detector. The absorbers also help

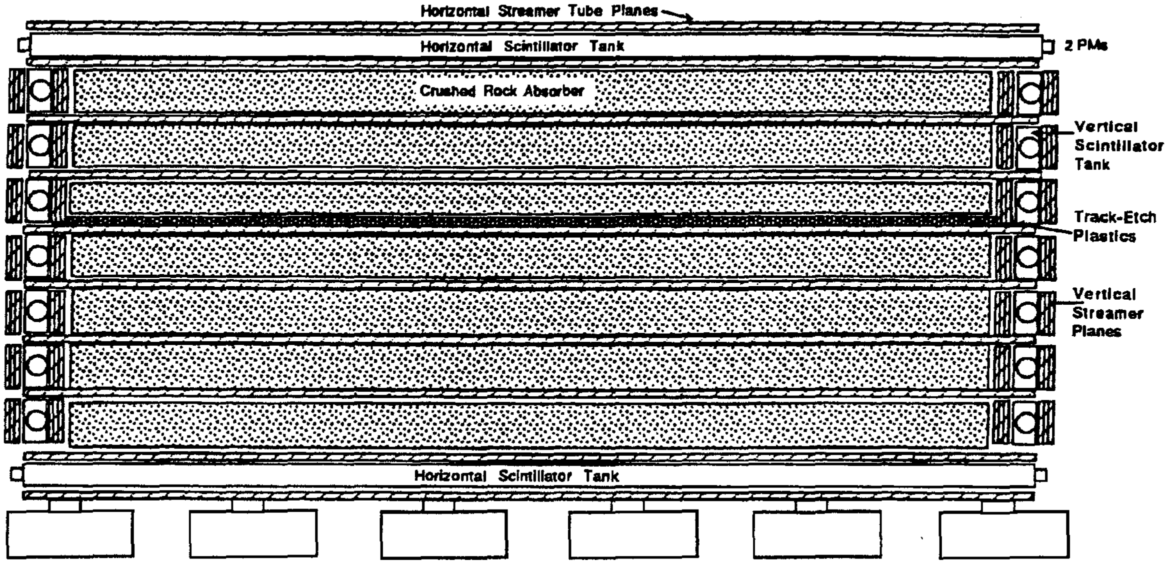

Figure 2.4: A cross section of the lower part of one supermodule [53].

to stop energetic secondary particles produced by particle showers. The horizontal streamer tube planes are instrumented with external pick-up strips, which make an angle of 26.5° with the streamer tube wires. The vertical scintillator tanks are sandwiched between six layers of streamer tube planes, with three planes on each side. No pick-up strips are installed on these vertical streamer tube planes. In the middle of the lower part of the detector, there is one horizontal layer of track-etch modules to provide redundancy for GUT monopole detection. Track-etch modules also exist on the west face and on the north face of the lower part of the detector.

The upper part (called the "attico"), about 4 m, does not contain any concrete absorber, and has fewer streamer tube layers than the lower part. The space below the attico is occupied by electronics and the data acquisition system. The upper part of each SM consists of two vertical and one horizontal (top) faces. The top face has 17 horizontal tanks (as opposed to 16 tanks in the center and bottom); this 17th tank fills the gap between modules. There are also four streamer tube planes at the top of the detector, two above and two below the horizontal scintillator tanks. The vertical faces of the upper part of the detector are similar to those in the lower part.

The east face of the detector is completely covered by a layer of track-etch modules, as well as the north face of the lower part of the detector. Each track-etch module including the layer at the center of the detector consists of two types of plastic with different sensitivities, CR-39 and Lexan, separated by an aluminum sheet. This configuration makes possible a distinction between heavily ionizing nuclear fragments and the expected signature for magnetic monopoles, which will be discussed in Section 2.5.

2.3 The Scintillator System

The MACRO scintillator system consists of the scintillator counters (the tanks), the liquid scintillator in a mineral oil base, the photomultiplier tubes (the PMT's), and the scintillator calibration system. We will discuss each of these in detail.

2.3.1 The Scintillator Tank

There are two types of scintillator tanks, those for the horizontal planes and those for the vertical planes. All are constructed from 0.63 cm thick PVC, and both types are of uniform rectangular cross section and consist of three chambers separated by transparent PVC windows. The large chamber in the middle of the tank is filled with liquid scintillator while two small chambers on either end are filled with pure mineral oil and house the PMT's. The inner walls of the scintillator tanks are lined with a white vinyl-FEP material to achieve better light reflection. The critical angle for total internal reflection from this wall is about 25.6°.

The two types of scintillator tank have different geometries. The horizontal tanks are 12 meters long, 75 cm wide, and 25 cm high, with scintillator chamber 1120 cm long and 73.2 cm wide. The typical depth of the scintillator oil is about 19 cm. The vertical tanks are also 12 meters long, but only 25 cm wide, and 50 cm high. The length of the active scintillator volume in the vertical tanks is 1107 cm, its width is 21.7 cm, and the oil depth is about 46.2 cm. There are variations in oil depth of several millimeters from tank to tank mainly because it was difficult to perfectly control the scintillator filling operation.

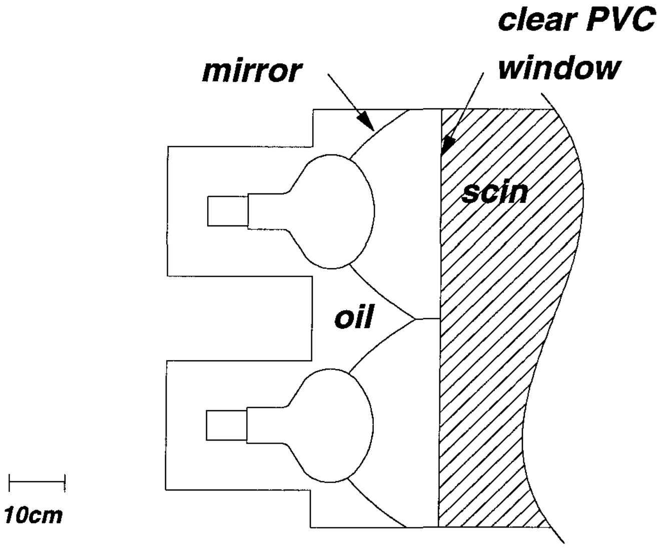

Figure 2.5: Configuration of a horizontal tank end chamber [52].

The different tank geometries result in different end chamber PMT configurations. In particular, horizontal tanks contain two PMT's while vertical end chambers have only one. Figures 2.5 and 2.6 show the details.

The mineral oil in the end chamber not only helps to achieve better light transmission between the scintillator chamber and the photocathode, but also helps to suppress electric sparks. This suppression works very well for the vertical tanks, where the mirrors are just a simply shaped core made of highly reflective aluminum, but not

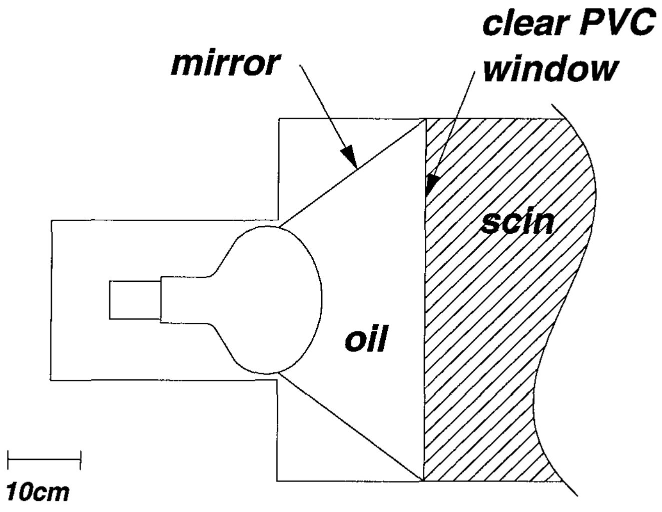

Figure 2.6: Configuration of a vertical tank end chamber [52].

as well for the horizontal tanks, where the mirrors are made of plastic coated with highly reflective aluminum. The shape of the mirrors is that of a revolved planar curve, which has been calculated [58] to guarantee that any light rays from a distant source which are coplanar with the mirror axis will reach the photocathode. The electric sparks in the horizontal end chambers are discussed below. Real data show that the vertical tanks have reasonably good light collection although it is not as impressive as in the horizontal tanks.

As is well known, PMT's are very sensitive to magnetic fields. The metal supporting frame in the detector (near horizontal scintillator tanks) concentrates the earth's magnetic field near the PMT's and thus reduces their efficiency. To solve this problem, a metal shield has been installed around the mirror and dynode chain of each horizontal PMT. This solution, however, can lead to serious sparking around the PMT's. To completely eliminate electric sparks, wires were installed to connect every conductor in the tank end together, to keep potential the same everywhere. For the end chambers in the vertical tanks, there is no need to install such "spark suppression kits" because there are no metal shields in the vertical end chambers, and the mineral oil helps to eliminate the sparks produced by the PVC and the mirror as mentioned earlier.

2.3.2 The Liquid Scintillator

It was a challenge to find the ideal scintillator for MACRO because the tanks are very long and must transmit light over a distance much greater than the attenuation length of usual scintillator materials. Fortunately, MACRO was able to obtain a very high purity mineral oil in North America, the attenuation length of which is more than 20 meters. By carefully selecting the scintillator added to this oil, we have developed a very good liquid scintillator mixture with an attenuation length of more than 12 meters.

The scintillator is a mixture of pseudocumene (1,2,4-trimethylbenzene), PPO (2,5-diphenyl-oxazole), and bis-MSB (p-bis[o-methylstyryl] benzene). The pseudocumene is the primary scintillator and the PPO and bis-MSB are light waveshifters which shift the scintillator light to the most sensitive region of the PMT around 350 nm. The peak absorption wavelengths for pseudocumene, PPO, and bis-MSB are 268 nm, 304 nm, and 345 nm respectively, and their absorption and fluorescence spectra are given in reference [55].

MACRO collaborators tested different scintillator concentrations, ranging down from the purest concentration of 40 g PPO and 40 mg bis-MSB per liter of pseudocumene (876 g). Figure 2.7 shows the results, which indicate that the number of photoelectrons produced increases as a function of scintillator concentration for small concentrations. The number of photoelectrons, however, starts to decrease when the concentration is greater than 4%, caused by absorption of light by the scintillator. A conservative pseudocumene concentration of 3.6% was selected. The final mix is:

- 96.4% mineral oil,
- 3.6% pseudocumene,
- 1.44 g/l of PPO, and
- 1.44 mg/l of bis-MSB.

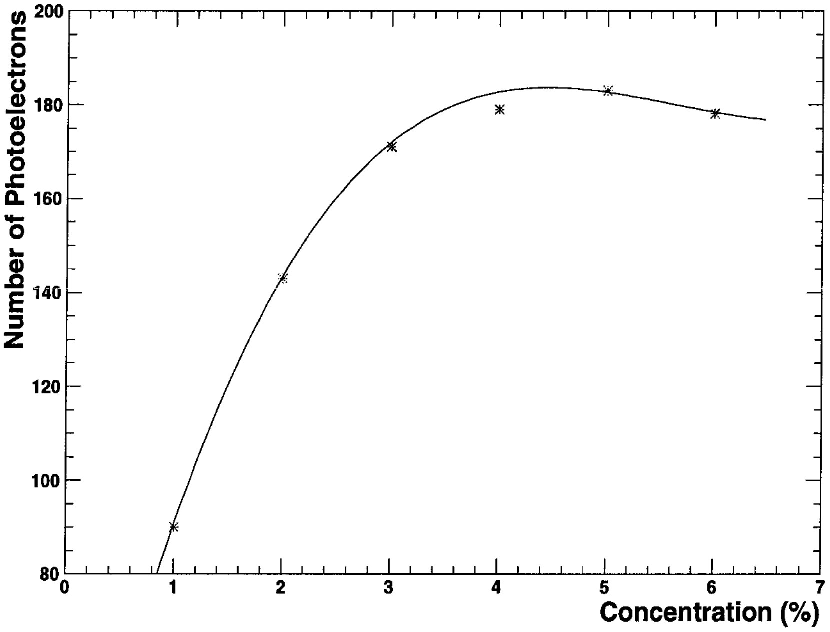

Figure 2.7: Light yield vs pseudocumene concentration for a muon passing through the far end of a MACRO test counter. This plot is from reference [58].

The mineral oil supplied by the manufacturer also contains 40 mg/l of an antioxidant. To monitor the quality of the liquid scintillator mixture, a special spectrophotometric apparatus was set up, checking the attenuation length for each batch of the mixed scintillator before putting it into the scintillator tanks.

2.3.3 Photomultiplier Tubes

The photomultiplier tubes used in the lower part of MACRO are EMI-642's, which have 20 cm diameter hemispherical photocathodes. This tube was chosen because its clear single photoelectron peak (Figure 2.8) is important for the detection of slow moving magnetic monopoles which are expected to produce light at the single photoelectron level. The PMT risetime is about 15 ns for a typical muon pulse, with a height of about 1.5 V. The jitter on this risetime is less than 1 ns.

These PMT's have 13 CeS dynodes in a fast venetian blind structure. The base of the PMT has been designed to give negative signals with typical power supply voltages of about −1600 V. The PMT's used in the attico vertical tanks are Hamamatsu tubes which are similar with EMI but no clear single photoelectron peak.

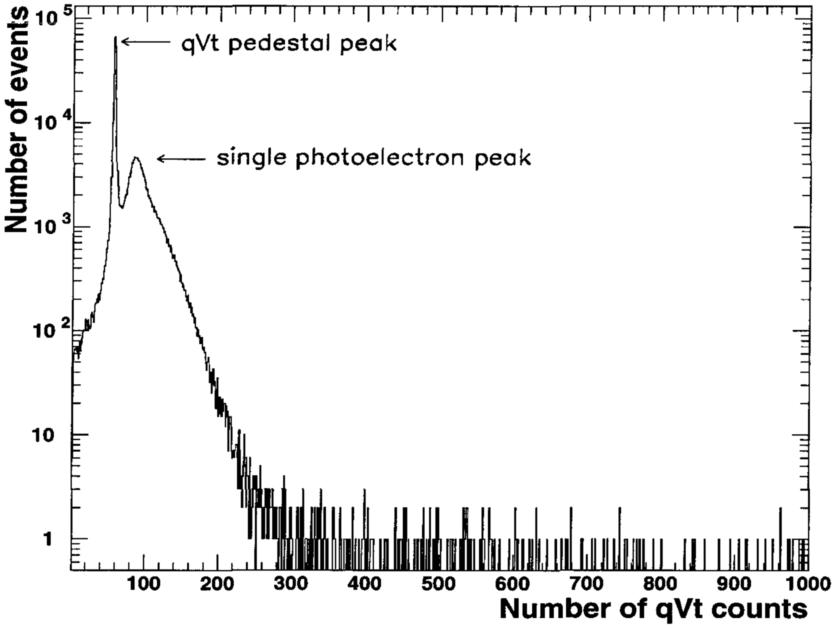

Figure 2.8: Pulse spectra from the qVt showing the single photoelectron peak.

Setting the PMT gains is an important issue because achieving uniform gains across the whole detector is critical for slow monopole search sensitivity. We use a LeCroy qVt module 3001 setup to integrate the PMT pulse charge, and adjust the high voltage supplied to each tube in order that the integrated charge of the single photoelectron peak is the same for all tubes. The pulses are obtained by firing an LED to produce a very weak light signal at the far end of the tank. Figure 2.8 shows a qVt spectrum taken from these signals.

The qVt method not only provides a way of precisely setting PMT gains but more importantly helps to achieve uniformity of the gain setting across the detector. The gains have been set at 4 mV for the single photoelectron peak. We use pulse height rather than integrated charges as a standard because the slow monopole trigger system is sensitive to the height rather than the charge of the pulse. The actual charge gain of the PMT's is about 5×10^6.

2.3.4 The Laser and LED Calibration System

The scintillator has both a LASER and an LED calibration system, both computer controlled. Basically, the lasers help to calibrate the energy, PMT response, and ADC response of the electronics while the LED's help to calibrate timing, waveform, small PMT pulse, and TDC response. A simple layout of the calibration system is shown in Figure 2.9.

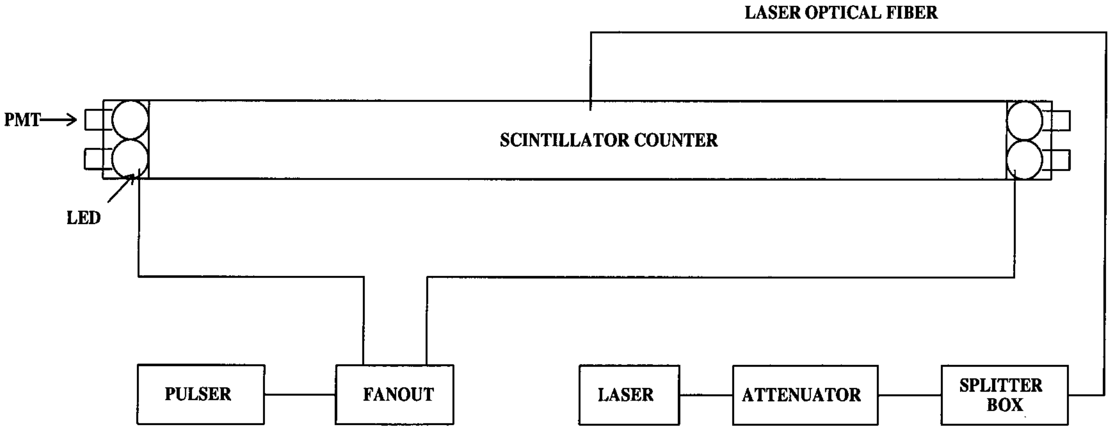

Figure 2.9: Layout of the LASER and LED calibration system.

MACRO uses a VSL337 nitrogen laser, which produces UV light at a wavelength of 337.1 nm. The laser fires very quickly within about 1 ns of the trigger, and is always fired at maximum output. An attenuator is used to control the total amount of light in each scintillator tank, so that the scintillator system is calibrated at different light levels. The laser light is transmitted to each scintillator tank via quartz optical fibers, which go to the center of each tank. Each SM in the lower part of MACRO has one laser, while two SM's of the attico share one laser.

HLMP-3001 red LED's manufactured by Hewlett-Packard reside on the mirrors beside the PMT's in each end chamber. They have a rated "speed of response" of 10 ns, with risetime for long pulses of about 60 ns. The LED's are driven by two central Hewlett-Packard 8115A programmable pulse generators, which are controlled by the data acquisition system so that two pulses with selected pulse height and relative time delay can be produced. CAMAC controlled fanout boxes are used in order to select tanks in any combination for slow monopole simulation or waveform digitizer calibration. More details about the LED calibration system can be found in reference [56].

The calibration is performed for each μVAX (two SM's) separately while the rest of MACRO is still in operation for monitoring gravitational collapse candidates. During calibrations, the laser is triggered at 2.0 Hz and the LED is triggered at 4.0 Hz. Both calibration systems work well; however, the laser sometimes triggers spontaneously during normal data-taking runs. The details are discussed in Chapter 5.

2.3.5 Scintillator Electronics

The scintillator system has three types of triggers—fast particle triggers, the slow monopole trigger, and two gravitational collapse (GC) triggers. The three fast triggers are:

- ERP (Energy Reconstruction Processor) for muon and FMT events,

- CSPAM (Chuck (Lane), S. P. Ahlen Muon trigger), and
- FMT (Fast Monopole Trigger).

The two GC triggers are the ERP GC and the PHRASE (Pulse Height Recorder And Synchronous Encoder). Table 2.1 lists all scintillator system triggers and their classification.

Trigger	Class	Time Window
ERP	fast	6.5 μs
ERP GC	GC	<15 min
CSPAM	fast	1 μs
FMT	fast	10 μs
Caltech Monopole	slow	500 μs
PHRASE	GC	—

Table 2.1: MACRO scintillator triggers.

Besides these trigger systems, MACRO also has a waveform digitizer (WFD) to record PMT signal waveforms. The ERP, the FMT, and the CSPAM trigger systems, along with the WFD, are all used for the fast moving monopole search and will be discussed in Chapter 4. The Caltech slow monopole trigger and the gravitational collapse trigger systems are not related to the topic of this thesis. Details can be found in reference [57] and reference [58, page 31–34].

2.4 The Streamer Tube System

Tracking in MACRO is performed by streamer tubes and pick-up strips, which are briefly discussed here. A thorough treatment can be found in reference [52].

2.4.1 Streamer Tube and Strip Structure

Each streamer tube module consists of eight-chamber cells of size 3.2 cm×25 cm×12 m. The chamber is made of PVC and is glued and heat sealed. Three sides of the cell are coated with a low-resistivity graphite ($\leq 1k\Omega$/square), and act as the cathode. A metal silvered Be-Cu wire resides in the center of each cell to act as the anode, and is supported by plastic at one meter intervals. Figure 2.10 shows the streamer tubes and strips.

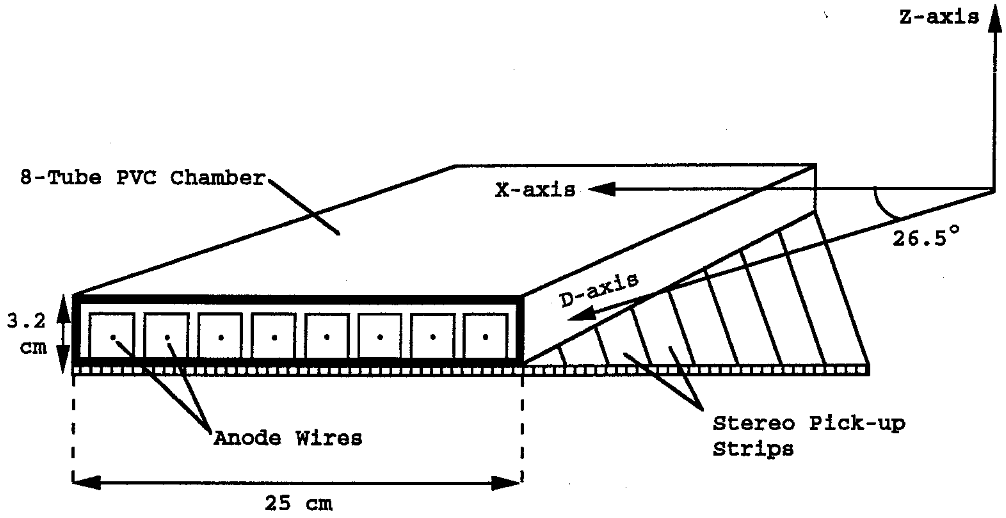

Figure 2.10: Streamer tube and pick-up strip configuration [52].

The gas used in the streamer tubes is a mixture of He (73%) and n-pentane (27%). Helium is chosen with slow monopole detection in mind (in view of the Drell-Penning effect [33]). The gas passes through all streamer chambers in parallel under the control of a central gas system at the rate of one complete volume change every five days.

The typical MACRO streamer tube high voltage is +4250 V, at which the gas works in the plateau region, a fully efficient noiseless operation region more than 700 V

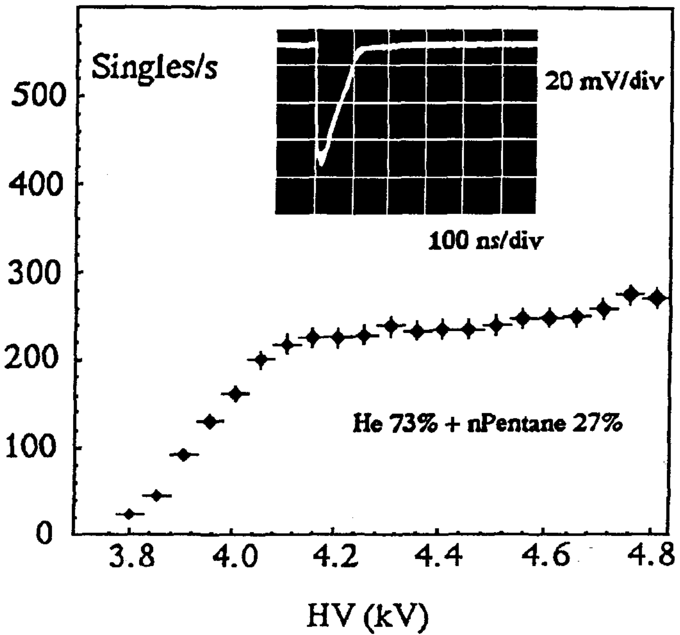

Figure 2.11: Singles rate as a function of high voltage. The inset shows a wire pulse for a test streamer tube [52].

wide. Figure 2.11 shows the streamer tube signal as a function of high voltage. The maximum drift time in a tube is about 600 ns; the dead region along the wire induced by the streamer discharge is a few mm wide, and the dead time is about 300 μs.

The pick-up strips are made of 40 μm thick aluminum, each 3 cm wide. As shown in Figure 2.10, the strips are placed at an angle of 26.5° to the streamer tubes, and face the uncoated side of the streamer tube cells. The charge induced by the streamer tube is picked up by the strips and transmitted to the ends where readout occurs.

The streamer tube is a low noise device, and its signal rate is dominated by ionizing particles from radioactive decay. In MACRO, this rate is quite low at 40 Hz/m^2. In Chapter 5, we will discuss event reconstruction using the streamer tubes and strips.

2.4.2 Streamer Tube Electronics

The streamer tube readout electronics cards are located at the end of each chamber. They are digital devices, each of which processes signals for the eight cells in each streamer tube module. The cards produce two digital pulses, one fast and one slow, for each signal over a 40 mV threshold; the fast pulse is 10 μs wide while the slow pulse is 500 μs wide. These digital pulses may be latched if a trigger occurs with the appropriate time window. The two possible triggers are referred to as "fast chain" and "slow chain," respectively. The data then can be read out by the acquisition system, which puts all the cards in series to create one long shift register: each shift command causes the readout of one bit while at the same time each card outputs one bit to the next card and accepts one bit from the previous card.

Strip readout is similar to streamer tube readout; the digital pulses, however, are stretched to 14 μs for the fast chain and to 580 μs for the slow chain, and, for the fast chain only, four strips are fanned into one bit.

In addition to the digital hit readout, there is also an analog streamer tube readout system, the Charge and Time Processor (QTP), which records the time and charge of every streamer tube hit. The information it provides is coarser than the digital information, however, because 32 wires are fanned into one channel. Details of the QTP system can be found in reference [52].

There are two triggers based on the streamer tube system, the Bari trigger (which is a muon trigger), and the streamer tube monopole trigger. The monopole trigger has a coincident time window of 480 μs, while for the Bari trigger it is 1 μs. Obviously, the Bari trigger is related to the fast chain and the streamer tube monopole trigger is related to the slow chain.

A Bari trigger is produced if one of the following combinations of hits is satisfied:

- Six out of ten horizontal planes,
- Five out of eight contiguous horizontal planes,
- Five out of six vertical planes on the same side,
- Three out of six vertical East planes and three out of six vertical West planes, or
- Three out of ten horizontal planes and three out of six vertical planes on the same side.

The exact streamer tube monopole trigger conditions are more complicated. Simply speaking, the monopole trigger requires seven or more planes to be hit with relative timing consistent with the passage of a slow particle. Two main devices have been developed to recognize this condition. First, each plane has a serial-in parallel-out shift register, with a total memory of 480 bits, each bit representing 1 μs. Second, a circuit which looks for 160 different majority coincidence patterns is used in order to check each "β slice." The streamer tube monopole trigger has significant geometrical acceptance for the detection of monopoles faster than about $\beta = 10^{-4}$. Details are given in reference [59].

2.5 The Track-etch Detector

As mentioned earlier, one horizontal layer and the entire east face of the MACRO detector are covered by track-etch modules, as well as the north face of the lower part of the detector. Each module has dimensions 25 cm×25 cm and consists of three layers of CR-39, three layers of Lexan, and an aluminum absorber which can absorb low energy ions produced coherently or by spallation. All are inserted on rails to allow for convenient removal.

In current theories of monopole energy deposition, the CR-39 threshold velocity for a bare monopole is about $10^{-4}c$. The threshold for Lexan is $\sim 0.3c$; hence, it is sensitive only to events with unusually large signals observed in the electronics detectors.

The track-etch will be mainly used for confirmation of a monopole candidate, if an appropriate signal in the scintillator counters and/or the limited streamer tubes is found. For these candidate events, certain modules will be selected around the expected position according to the streamer tube and scintillator counter information. A special chemical etching process will then be performed, allowing the material damaged by magnetic monopoles or heavily ionizing nuclear fragments to be removed. A scan for holes will be performed with low magnification optical methods to examine the candidate events. The track-etch detector is not used in this analysis, however; details can be found in reference [52].

2.6 The Data Acquisition System

The MACRO online data acquisition system uses two central VAX 4000 computers along with three μVAXes connected via Ethernet. Each μVAX controls two SM's and can be operated independently. Data are collected through a CAMAC interface on the Q-bus of each μVAX. The central VAX 4000's handle the data stream and write it to the hard disks; they run VAX/VMS while the three μVAXes run VAX-ELN. Figure 2.12 shows the general configuration of the data acquisition system, which is connected to the external laboratory via optical fibers and from there is connected to the rest of the world via INTERNET and DECNET.

It bears mentioning that the PHRASE system uses a completely separate acquisition system, which during the "six-month-run" employed two μVAXes, each of which handled three SM's. This separated system allows PHRASE to take data

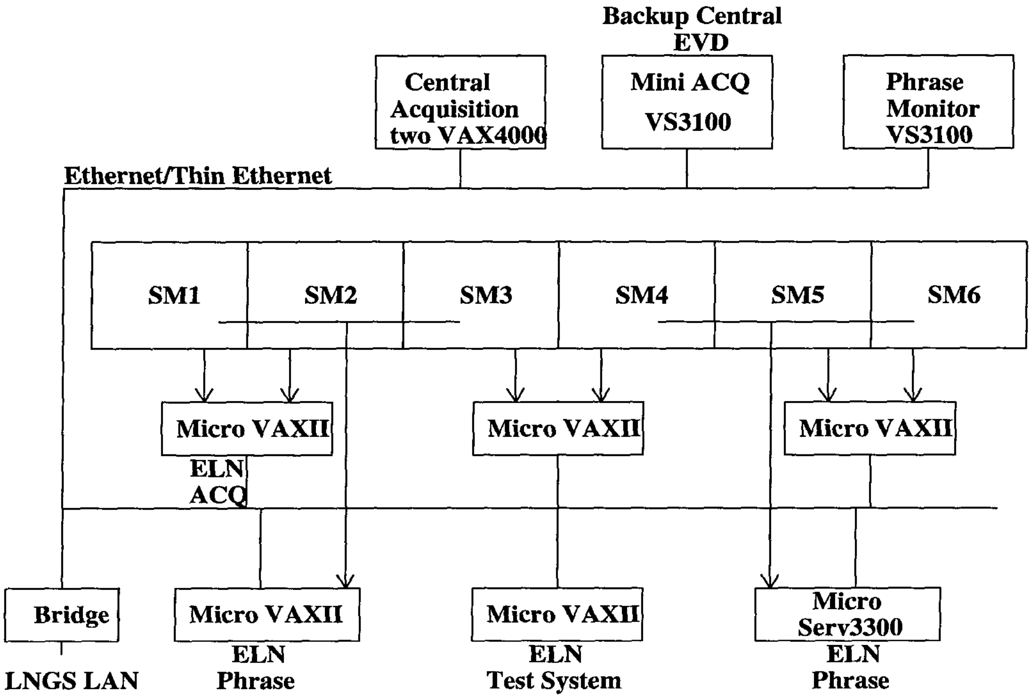

Figure 2.12: General layout of the MACRO global data acquisition system.

continuously for the gravitational collapse trigger even if the main data acquisition is shut down. It currently uses three μVAXes, and each of which handles two SM's including the attico.

2.7 Other Physics Capabilities

Although searching for magnetic monopoles is the main goal of the MACRO experiment, it can also achieve many other physics objectives. MACRO's geometrical acceptance is larger than that of any other underground experiment in the world, making it useful for general cosmic ray physics experiments such as the measurement of the spectrum, composition [60] [62], and decoherence function [61] of the ultra-high energy cosmic rays, *etc.* With the ability to record more than 5 million muon events annually, MACRO is also able to search for muon sources [63], and has performed a muon all-sky survey [63]. Using upward going muon events, MACRO performs WIMP searches [64] and neutrino oscillation [65] measurements, and with a total of 610 tons of liquid scintillator, MACRO is well able to monitor gravitational collapse. (In fact, there are two separate systems for this purpose, ERP and PHRASE, as mentioned earlier.) Nuclearite [66] and heavily ionizing particle searches can also be made in MACRO, and, lastly, a fractionally charged particle trigger system is now under construction.

Chapter 3

Monopole Ionization and Scintillator Light Yield

To know what the signals of fast monopoles look like is one of the most important issues for their detection. This search mainly depends upon the liquid scintillator system; therefore, the light yield of monopoles in liquid scintillators is our concern.

Energy losses of magnetic monopoles are very much dependent on their velocity, and there are several scenarios regarding monopoles in different velocity regions. In general, energy losses are extremely large for fast moving monopoles (with velocities greater than $0.1c$) while they are small for slow moving monopoles (with velocities less than $3 \times 10^{-3}c$), and the energy loss of monopoles with velocities between $10^{-2}c$ and $1.0c$ is much larger than muon minimum ionization energy. This can be seen in Figure 3.1 in the following section.

Energy losses are understood for the response of the scintillation light yield. In general, the light yield is proportional to the energy deposition at low energy loss rate; for particles with extremely high ionization energy losses such as fast monopoles, however, the light yield is not proportional to the energy because of the scintillation saturation. The light yield of magnetic monopoles has been calculated for MACRO liquid scintillator, and for fast monopoles is about two orders of magnitude larger than that produced by muon.

In this chapter, we will discuss magnetic monopole energy losses in various media and their light yield in MACRO scintillator.

3.1 Monopole Energy Loss

The energy loss mechanisms for fast moving monopoles are quite different from those of slow moving monopoles. Generally, for monopole velocities greater than αc, where α is the fine structure constant, a formula similar to Bethe-Bloch [72] is used; for monopole velocities between αc and $10^{-3}c$, a formula derived by Ahlen and Kinoshita using the Fermi gas model is used; and for monopole velocities less than $10^{-3}c$, a method suggested by Drell *et al.* is used. There has been no direct confirmation of these formulae from experiments; however, based on knowledge of the electromagnetic interaction, they are widely accepted. We will briefly discuss each of them below.

3.1.1 Relativistic Monopole Energy Loss

Several authors have discussed the energy loss of fast moving magnetic monopoles [67, 68, 69, 70, 71]. These discussions are based on the symmetry of the electromagnetic interaction. As is well known, the energy loss of electrically charged particles at relativistic speeds can be described successfully with the Bethe-Bloch formula:

$$\frac{dE}{dX}|_e = \frac{4\pi N Z^2 z^2 e^4}{mc^2\beta^2}[\ln\frac{2mc^2\beta^2\gamma^2}{I_e} - \beta^2 - \frac{\delta_e}{2}], \tag{3.1}$$

where N = Avogadro's number,
ze = electric charge of the incident particle,
Z = atomic number of the material,
m = electron mass,
βc = velocity of incident particle,
$\gamma = 1/\sqrt{1-\beta^2}$,
I_e = mean ionization constant of the material, and
δ_e = density effect [73] correction.

This formula is derived by considering collisions between an incident particle and the electrons around the atoms of the medium. (The energy transfer due to the interaction of the incident particle with the nuclei of the media is very small compared with that due to the interaction of the incident particle with electrons.) The collisions are divided into two classes: close collisions and distant collisions. Two assumptions are used in this formula:

- For close collisions, two-body kinematics and the Columb scattering cross section are used, and the electrons in the material are considered to be free;
- For distant collisions, the impact parameter is large enough to consider each electron and the rest of the atom as a dipole.

This formula is appropriate for particles with velocity greater than αc, or roughly the electron orbital velocity. It should remain valid for magnetic monopoles, with the effective charge of the monopole depending upon its velocity ($g\beta$). A formula similar to Bethe-Block for relativistic magnetic monopoles is given by S. Ahlen [71].

$$\frac{dE}{dX}|_m = \frac{4\pi N Z^2 g^2 e^2}{mc^2}[\ln\frac{2mc^2\beta^2\gamma^2}{I_m} - \frac{1}{2} + \frac{K(|g|)}{2} - \frac{\delta_m}{2}], \tag{3.2}$$

where $|g|$ = magnetic monopole charge,
I_m = mean effective ionization constant of the material for monopoles,
δ_m = density effect [73] for monopoles, and
$K(|g|) = 0.406$ for a monopole with $ge = \frac{1}{2}$.

Reference [71] has also shown that the differences between I_e and I_m and between δ_e and δ_m are of the order of 1% or less and can be ignored, although the definitions of I_e and δ_e remain fundamentally different from those of I_m and δ_m.

Like the Bethe-Bloch formula, Equation 3.2 is only strictly valid for $\beta >> \alpha c$. For velocities less than this, the formula breaks down because the two assumptions are no longer valid. In close collisions, for instance, the orbital velocity of the electron is comparable to or even greater than the velocity of the incident particle; hence, we cannot treat the electrons as being free. To get a valid energy loss formula in the low velocity limit, we must use a different approach.

3.1.2 Slow Moving Monopole Energy Loss

The energy loss of slow electrically charged particles has been calculated by several authors. They apply the Fermi gas model, which has been used especially successfully [75, 76] for conductors, semi-conductors, and heavy atoms ($Z > 10$) because the electrons in the conductor, the electrons in the conduction band of a semiconductor, and the outermost electrons in heavy atoms are not strongly confined by the nuclei, and thus can be treated as a Fermi gas of free electrons. Lindhard [76] has derived such a formula:

$$\frac{dE}{dX}|_e = \frac{4}{3\pi}\frac{m^2 Z^2 e^4 v}{\hbar^3}[\ln \pi(\frac{v_F}{\alpha c})^{1/2} + \frac{\alpha c}{\pi v_F} + (\ln \pi - 1)/2], \tag{3.3}$$

where $v =$ incident velocity,

$v_F = \hbar(3\pi^2 N)^{1/3}$ the Fermi velocity (N is the conducting electron density),

$\alpha =$ fine structure constant, and

$Z =$ atomic number of the material.

The characteristic velocity of Fermi gas electrons is v_F, which is roughly equal to αc. The Fermi gas approximation is valid for an incident particle with velocity much less than v_F so that the implicit perturbation assumption used in the calculation is correct. The kinematic limit to energy transfer (for $v_F << c$) is $2mv(v + v_F)$. This energy must be greater than the minimum energy gap (E_g) required to ionize an electron, which is typically a few eV. Setting $E_g = 2$ eV, we find that the incident particle velocity must be greater than about $3 \times 10^{-4}c$.

Using this method, Ahlen and Kinoshita [74] obtained the following formula for magnetic monopole energy losses:

$$\frac{dE}{dX}|_m = \frac{2\pi N g^2 e^2 v}{mc^2 v_F}[\ln\frac{1}{Z_{min}} - \frac{1}{2}], \tag{3.4}$$

where $|g| =$ the magnetic monopole charge,

$Z_{min} = \hbar/(2mv_F\Lambda)$ is determined by eddy current losses, where for conductors Λ is the mean free path $\approx 50aT_m/T$, and

$a, T_m, T =$ the lattice constant, the melting temperature, and the temperature of the material.

In the use of the above formula for non-conducting media such as scintillators, we can set N equal to the total valence electron density and set Λ equal to the atomic radius. A calculation of the energy loss for magnetic monopoles in silicon, made by Ahlen, is shown in Figure 3.1 together with the calculation for slow protons by others. The plot shows that the Fermi gas model is in good agreement with experimental data for protons.

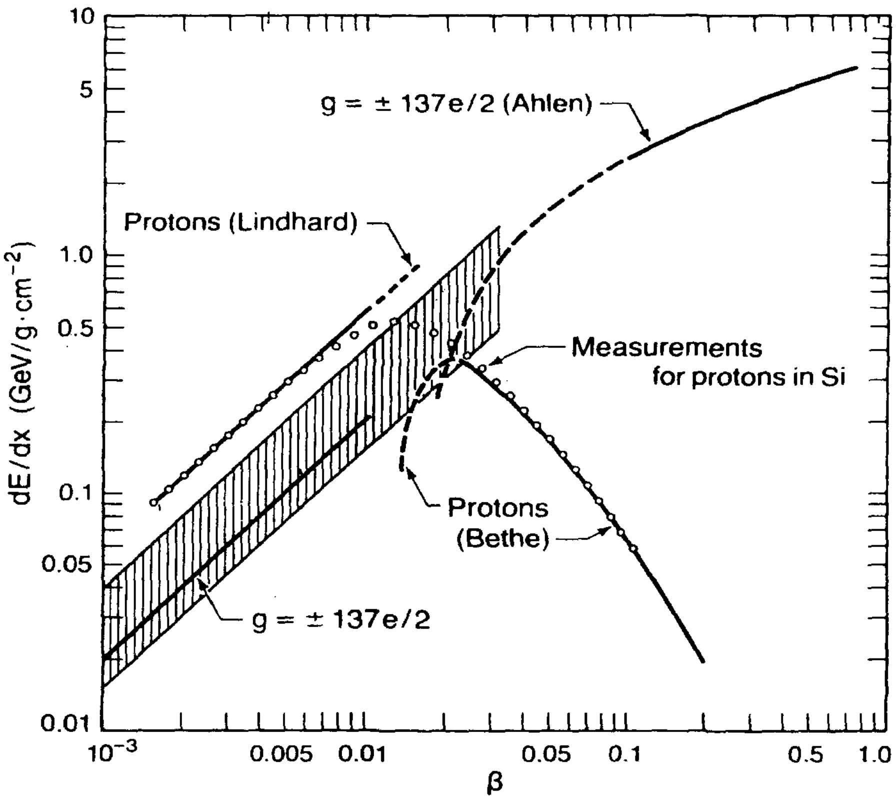

Figure 3.1: Energy losses in silicon for protons and for magnetic monopoles with $g = \pm 137e/2$. Experimental data (open circles) showing measurements of energy losses for protons with both high and low velocities are included. The calculated energy losses for monopoles using different methods discussed in the text are shown. The hatched region indicates the uncertainties in the calculation. This figure is reprinted from reference [74].

For monopoles with velocities less than 10^{-3}c, the above formula is invalid. If we try to extrapolate the formula to this very low velocity region, we get very small energy losses; S. Drell *et al.* [33], however, used a very different method to calculate the energy loss of monopoles with velocities less than $10^{-3}c$ in matter which provides a different answer.

The idea for Drell's calculation is the following: when a magnetic monopole passes through matter, the magnetic field is very large near its path because the monopole charge is large. This strong magnetic field will cause the energy levels of the atom's electrons to split (Zeeman spin splitting). For instance, the energy shift of an electron at a distance r from the monopole is $eg/2mr^2 \sim 7$ eV. If the splitting is large enough, energy level crossing will occur and two different levels will be mixed, and electrons might freely switch into other levels. As a result, an atom could be excited after the monopole has passed. The energy loss calculated using this method is much higher than the extrapolation of Ahlen and Kinoshita's formula. Besides this greater energy loss, Drell's mechanics also implies that scintillation light could be produced by very slow moving monopoles even though the maximum kinematic energy transfer through collisions is less than the energy gap between the ground state and an excited state of an atom. This important phenomenon could allow the detection of very slow moving magnetic monopoles in ionization dependent experiments.

From the above discussion we understand that the energy losses of magnetic monopoles are strongly dependent upon their velocity. For fast moving monopoles, the energy loss is enormous, roughly a factor of $(137/2)^2 \sim 5,000$ times the minimum ionization energy loss. For very slow moving monopoles, the energy losses are smaller and much less than the minimum ionization energy loss, but still detectable. In MACRO, because we use liquid scintillator to detect the light produced by monopoles, we will carefully discuss the light yield of monopoles in scintillator materials in the following section.

3.2 Monopole Light Yield

The energy losses in scintillator and the scintillator light yield are quite different issues, but they are strongly related. Only part of the energy loss is converted to excitation or ionization of the scintillator molecules to produce scintillation light, while most is converted into heat. As is well known, the scintillation response is linear in energy loss for low loss rate dE/dX. Fast muons, with minimum ionization energy rates of about 2 MeV/g cm^2, fall within this linear regime. When the energy loss rate is high, on the other hand, the total amount of light is not linear in energy loss, this nonlinearity being due to the scintillation saturation.

A widely used semi-empirical formula describing the light yield as a function of energy loss was first proposed by J. B. Birks [78]:

$$\frac{dL}{dX} = \frac{S(dE/dX)}{1 + B(dE/dX)}, \tag{3.5}$$

where dL/dX = the light yield rate,
dE/dX = the energy loss rate,
S = the scintillation efficiency, and
B = the scintillator saturation constant, typically about 10^{-3} gcm^{-2}/MeV in commonly used scintillators.

This formula describes the scintillation behavior quite well. When the energy loss rate is small, the term BdE/dX can be ignored in the denominator and the light yield rate is a linear function of the energy loss rate. However, for very high rates of energy loss such as for fast moving monopoles, the light yield will completely saturate and be proportional only to the pathlength of the incident particles in the scintillator.

3.2.1 The Scintillator Saturation Constant

The saturation constant of MACRO scintillator has been measured [79] by comparing the light yields of electrons and low energy α particles. The electrons were produced by recoil γ rays from Co^{60} and Cs^{137}, yielding 1.17 MeV and 1.33 MeV γ's, while the α particles result from the Radon (Rn^{220}) decay chains, which yield α particles of 8.785 and 6.06 MeV. The electrons have a small energy loss rate, so that light yield is just proportional to their energy loss; the energy loss rates of the low energy α particles, however, are about 1.1 GeV/g cm^{-2}, which is quite high. By comparing light yields from the α particles and electrons, we obtain the saturation constant. In addition to measuring the MACRO standard scintillator (at a 3.6% scintillator concentration in the mineral oil), we have also measured the saturation constants for concentrations from 1% to 10% at 1% intervals. Figure 3.2 shows the results. The saturation constant for the MACRO standard scintillator was determined to be (11.6 ± 0.6) mg cm^{-2}/MeV.

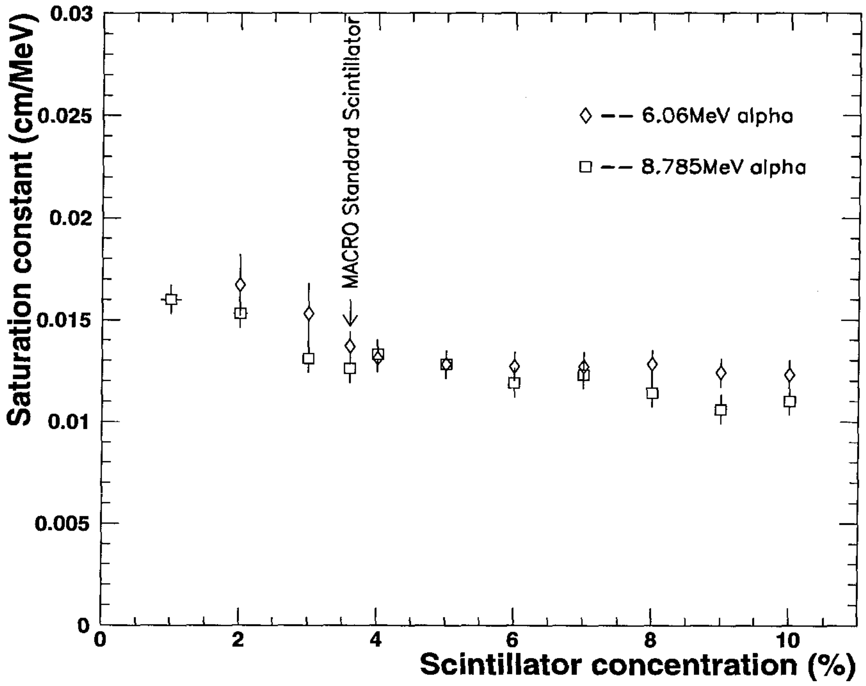

Figure 3.2: Measurements of the saturation constants for scintillators at different concentration levels. There are only two points for each sample, one obtained from the 8.785 MeV α's, and the other from the 6.06 MeV α's.

The scintillation efficiency of the MACRO scintillator is about 40%* relative to anthracene, which requires 68 eV of energy loss per scintillation photon emitted. Therefore, the absolute scintillation efficiency of the MACRO scintillator is about

---

*From Dr. S. Ahlen, a MACRO collaborators at Boston University, who measured the scintillation efficiency for the MACRO scintillator.

170 eV of energy loss per photon. In the following discussions, however, we will use the light yield relative to that produced by muons at the minimum ionization energy loss rate.

3.2.2 Fast Moving Monopole Light Yield

Looking at the energy loss rate for fast monopoles, we find that according to Birks' formula the scintillator will function completely in the saturation region where the light yield is proportional only to the pathlength of the monopole. This light yield level is about 135 times that produced by muons at the minimum ionization energy loss rate.

Simply speaking, the complete saturation region is the column along the incident monopole path within which all the scintillator molecules are excited or ionized. The radius of this column is called the impact parameter, and is about $\sim 76\beta\gamma a_0$ where a_0 is the Bohr radius. For monopoles with velocities greater than $0.1c$, there are also some energetic electrons, δ rays, which have enough energy to escape from the saturation column, after which they can produce additional scintillation light not included in Birks' formula. At extremely high speed, this additional light yield becomes dominant, and for this range the total scintillation light yield is roughly proportional to the total δ ray energy. However, we also must take into account the fact that some very high energy δ rays will escape from the scintillator volume and thus part of their energy will not be recorded. Figure 3.3 shows the light yield in scintillator due to these additional δ rays consideration. In Appedix A, we discuss more detail on the δ rays contribution to the scintillation light.

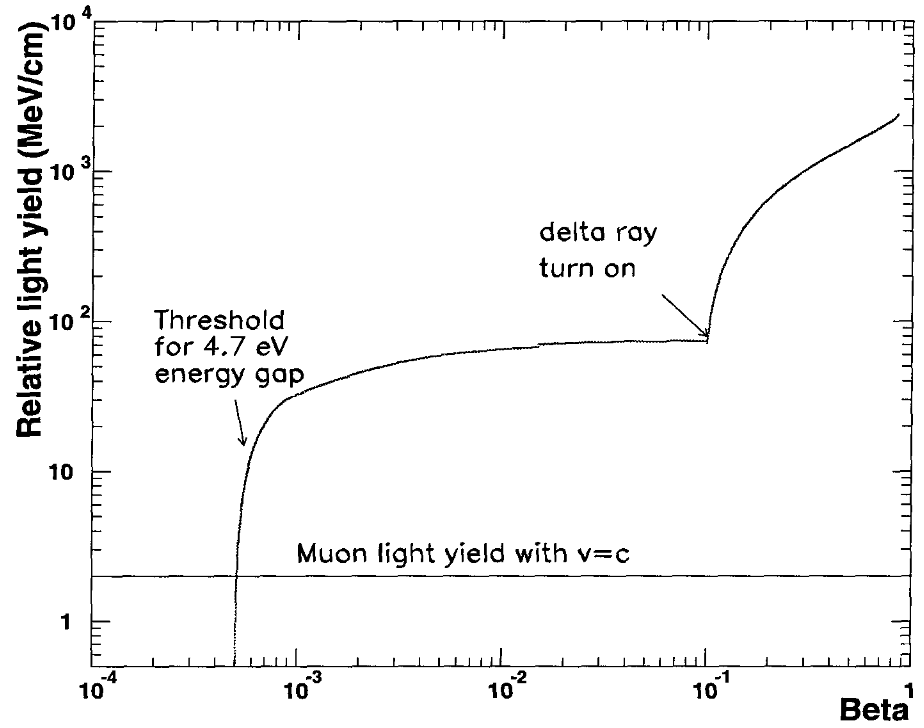

Figure 3.3: Estimate of the light yield for monopoles in MACRO scintillator. The Drell's energy loss calculation for very slow monopoles has not been included because no calculation has been done.

3.2.3 Slow Monopole Light Yield

For slow moving monopoles, we again can use Birks' formula to calculate the scintillation light yield, with the energy loss rate from Ahlen and Kinoshita's formula. For scintillator materials, however, Ahlen and Tarlé [77] have pointed out that there will be a cut-off energy in the light yield due to the energy gap of the scintillator molecules. As mentioned above, if the maximum energy transfer from the two-body collision is less than the energy gap, the electron can not be excited to higher energy states. Hence, there will be no scintillation light even though the incident particle still loses thermal energy. For MACRO scintillator, this energy gap is about 4.7 eV, and using two-body kinematics, we calculate that the scintillation light yield has a cut-off at velocities less than about $\sim 6 \times 10^{-4}$c.

Figure 3.3 shows the light yield in MACRO scintillator for monopole velocities from $10^{-4}c$ to $1.0c$. Generally, the scintillation light yield is much higher than the maximum light from Birks' formula when the δ rays turn on. For slow velocities, the light yield drops significantly near the threshold of the scintillator energy gap and completely cuts off below this point. However, at the velocities lower than $10^{-3}c$, the light yield from Drell's calculation becomes important. There is no precise calculation using Drell's mechanics for the exact light yield for the MACRO scintillator in this velocity range, but nevertheless the light yield of very slow monopoles in helium has been calculated and is proportional to the velocity. Most importantly, it does not have the exponential cutoff as in Tarlé and Ahlen's calculation. Interested readers can find details in reference [58].

Chapter 4

The Fast Moving Monopole Trigger System

The fast moving monopole trigger is sensitive to monopoles with velocities greater than $10^{-2}c$. (The slow monopole trigger is sensitive to monopoles with velocities less than $10^{-2}c$.) Two systems have been designed for the fast monopole detection: the ERP and the CSPAM/FMT. Because of the large expected signals, both have nominal trigger efficiencies near 100%; due to cable connection problems, however, the effective efficiency of the CSPAM/FMT is lower by several percent.

The ERP system, which was originally designed for muon and gravitational collapse detection, has been modified to trigger on fast monopole candidates. This ERP trigger is based on single scintillator counters. Generally, if signals from both ends of a scintillator tank pass threshold within 270 ns of one another, a trigger will be generated, and ADC and TDC information from the signals will be recorded.

The FMT is also a scintillator based trigger dedicated to fast moving particles. It is a double-face trigger, requiring signals from two different faces within 10 μs of one another. A single-face signal is produced when the PMT signals from both ends of a scintillator tank pass the threshold (about −120 mV) within a 100 ns coincident window. The CSPAM is configured similarly to the FMT trigger but has a shorter coincidence window (1 μs), and the FMT is vetoed by the CSPAM to eliminate muon events. Both the CSPAM and the FMT triggers force readout of the waveform digitizer.

In the following sections, we will discuss in detail the ERP and FMT/CSPAM triggers, as well as the configuration of the waveform digitizer.

4.1 The ERP Trigger

The ERP (Energy Reconstruction Processor) is an integrated ADC/TDC readout system for the MACRO scintillator counters. It provides both the fast particle and the gravitational collapse triggers. It is composed of three separate electronics modules: sample-and-hold (S/H) cards, trigger processors, and the readout supervisor. In each SM, the S/H modules occupy one VME crate and the trigger modules and the supervisor occupy one CAMAC crate.

The S/H module is the front end of the ERP system. PMT signals from the fanout enter the S/H module via 50 Ω coaxial ribbon cables. (The fanout module linearly copies PMT signals for each different system.) The S/H module is packaged as a 9U VME module and contains the circuits for four scintillator tanks with two channels per tank. Figure 4.1 shows the general layout.

The primary function of the S/H is to hold the PMT signal amplitude and timing information for both readout and trigger processing purposes. Signals from each end of the scintillator tank are split into four identical copies, two of which are used to provide TDC information and two of which provide the ADC inputs. The TDC signals are discriminated at two different thresholds, starting a constant current

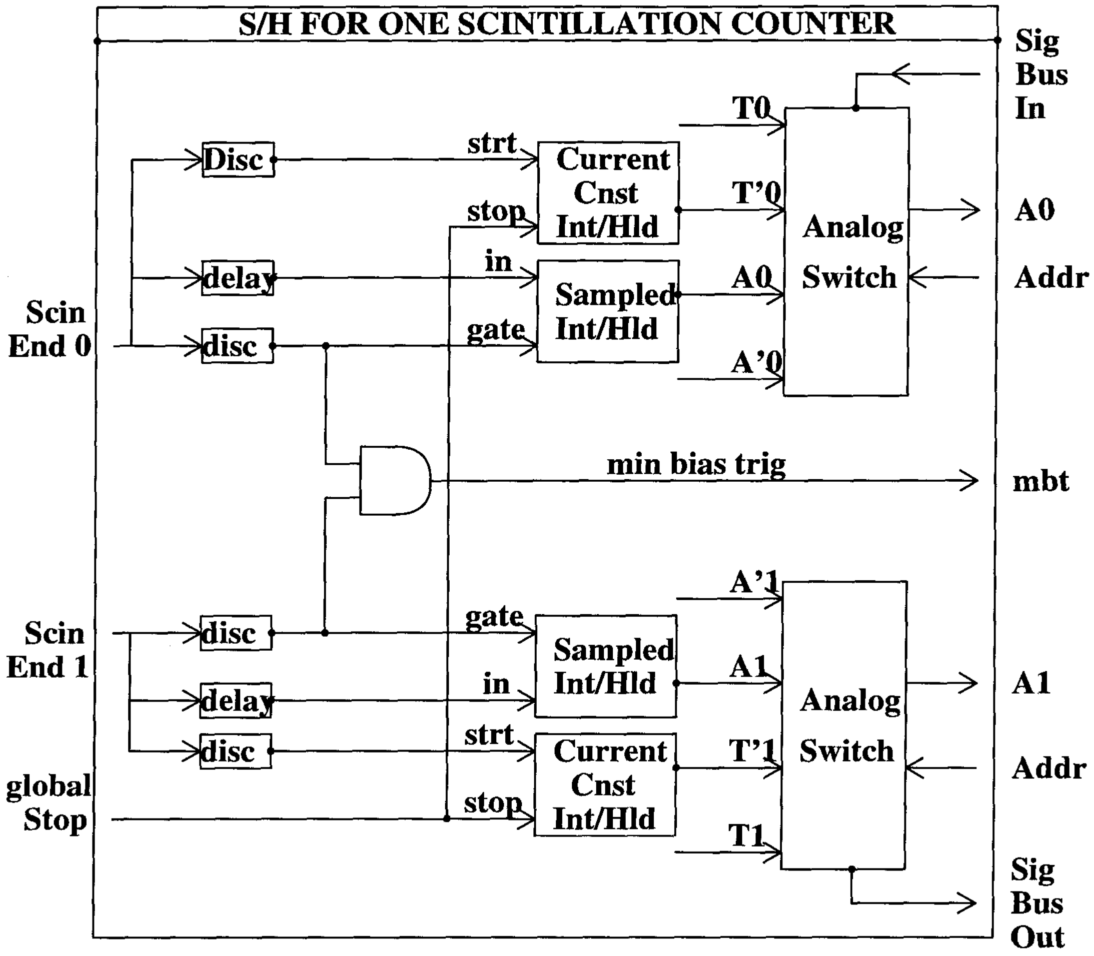

Figure 4.1: General layout of the ERP sample-and-hold (S/H) module.

source which charges a capacitor until stopped by the first minimum bias trigger signal (explained shortly) after a delay of 400 ns. The charge in the capacitor is digitized to produce the TDC value if a trigger occurs. The signal from the higher threshold discriminator produces a "TDC high" value while the other produces a "TDC low" value (T0/T1 and T'0/T'1, respectively, in Figure 4.1). The use of two TDC measurements with independent timing thresholds not only provides redundancy but also helps to eliminate the effects of PMT pre-pulsing, which will be discussed in Chapter 5. One of the remaining two signal copies used for the ERP ADC information is discriminated. If over threshold, a one-shot generates a gate for the integration of the signal and also for the minimum bias trigger as well. The last signal copy is sent through an analog delay line, then split into one direct output and one output attenuated by a factor of ten (A0/A1 and A'0/A'1 in Figure 4.1). Both the direct and attenuated outputs are integrated (using separate integrators) with the aforementioned integration gate. The delay time used for ADC integration is 140 ns to guarantee that the signals completely fall within the integration gate.

The integration gate is 270 ns, which is somewhat short for the 180 ns width of the PMT pulse which would be produced by a magnetic monopole with velocity at $10^{-2}c$ because the signal gets delayed by 140 ns, but the waveform digitizer can be used for very wide pulses to compensate for the short ERP ADC integration gate. This gate is also used to produce a minimum bias trigger if there is a coincidence within the gate from the other end of the same tank.

Discriminator thresholds are set via CAMAC bus, and ADC thresholds are generally about -120 mV (a typical muon pulse is about -1.5 V). The S/H module holds all the integrated TDC and ADC information while awaiting for a decision from the trigger processor. In the absence of a minimum bias trigger within the 270 ns coincident gate time, the S/H module will clear itself immediately without the participation of the trigger and the readout modules.

Figure 4.2 shows the trigger processor and readout supervisor layouts. The trigger processor module is a CAMAC module connected to the S/H module through a 30-conductor ribbon cable. When a minimum bias trigger occurs, the module begins processing the integrated PMT pulses stored in the S/H modules, performing rapid 6-bit digitizations. The digitized values are used as addresses for an 8K×8K RAM look-up table (LUT), which is preloaded with the information required to make both muon and GC trigger decisions. The LUT is produced from both muon events and laser calibration data to set a muon trigger threshold of about 7 MeV. If the LUT indicates that the event does not qualify, a clear signal will be issued to clear the S/H module; if it does qualify, the readout supervisor module is notified and inhibit signals are issued to all the S/H modules. The trigger processor requires about 6.2 μs to produce a trigger, long enough for a particle as slow as $10^{-2}c$ to cross one SM from corner to corner diagonally.

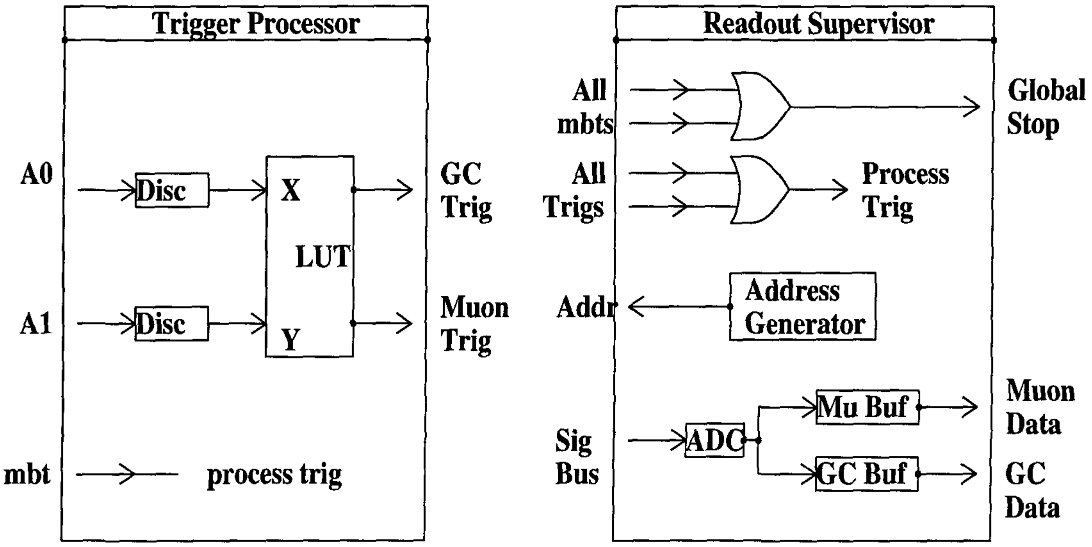

Figure 4.2: General layout of the ERP trigger processor (left) and the ERP readout supervisor (right).

The readout supervisor module is also a CAMAC module, which begins operation when a trigger is received from any trigger processor. The readout module notes which trigger processors have triggered and begins digitization of these channels' signals with a 12-bit 1 MHz ADC via a single daisy-chained RG-172 cable. There are two buffers in the readout module, the muon and the GC buffers, which are read out separately according to which type of trigger was generated.

The ERP is a single box trigger, and each SM is independent from the others, so inter-supermodule events trigger each SM separately. For these events, an inter-ERP timing device is used to record the relative timing among the different SM's. The ERP has a high trigger efficiency for muon and highly ionizing particles, and for fast moving magnetic monopole, the efficiency should be close to 100%.

4.2 The FMT/CSPAM Trigger

The FMT (Fast Monopole Trigger) is dedicated to the detection of fast magnetic monopoles. It is a two-face trigger and combines adjacent SM's in order to achieve a large acceptance for monopoles, whose flux is expected to be isotropic.

Signals from the PMT fan-out module are connected to the FMT/CSPAM fan-in module through 93 Ω coaxial ribbon cables with an 8:1 fan-in ratio. The FMT/CSPAM generates three identical analog outputs which are used to produce the triggers and for the waveform digitizer. They are transmitted to a discrimination/latch module through 50 Ω coaxial cables which are quite long because they must transfer signals to adjacent SM's. If a signal is greater than the discrimination threshold, a 100 ns wide NIM logic pulse is generated using Philips CAMAC 7601 modules and output to a coincidence module. The threshold is set via the CAMAC bus at about −200 mV for horizontal scintillator tanks and about −100 mV for vertical tanks, which is sufficiently high to eliminate background signals from radioactivity and low enough to have good trigger efficiency for muon pulses.

The coincidence module generates an output if the signals from both ends of a tank coincide within 100 ns, which is sufficient for a light pulse to travel the length of the tank (56 ns). Each coincidence module has inputs for two SM's, and two faces on the same side of adjacent SM's are combined together into one output. Hence, there are a total of four outputs for the lower part of the detector, corresponding to the center, bottom, west and east faces. The output from each face starts two gate generators which produce 1 μs wide and 10 μs wide logic pulses for trigger decisions.

The four 1 μs gates are sent to a coincidence module for the CSPAM muon trigger.

The four 10 μs gates are sent to another coincidence module for the FMT. The trigger condition is the same: the coincidence of any two out of four faces. The FMT, however, is vetoed by the CSPAM in order to remove muon events.

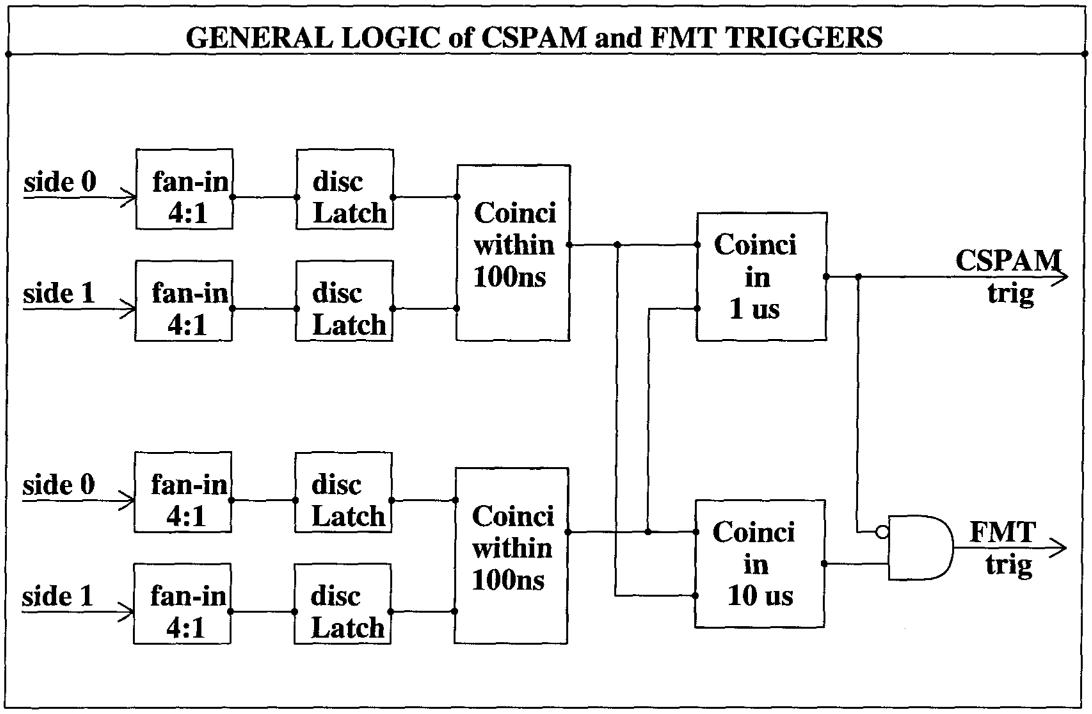

Figure 4.3: General layout of the FMT and the CSPAM trigger systems.

If a trigger occurs, it notifies the discriminator/latch modules to hold all information for readout and latches information about which group of tanks fired. Figure 4.3 shows the layout of the FMT and CSPAM triggers.

Because the FMT/CSPAM trigger requires a two-face coincidence and has a higher threshold than the ERP system, its trigger efficiency is lower; for two-face muon events, however, the CSPAM trigger efficiency should be close to that of the ERP. Neither the FMT nor the CSPAM trigger has any standalone readout. Both use the waveform digitizer to record events.

4.3 The Waveform Digitizer

Two LeCroy 2261 CAMAC waveform digitizer modules were used by each SM, giving two channels per face. Each module had four inputs, each of which had a buffer containing 320 words with a dynamic range of about 2 V. Signals from a single central 80 MHz TTL clock were distributed to every WFD module to obtain a uniform sampling rate. The WFD could be operated in either uni-phase or bi-phase mode. In bi-phase mode, two channels are combined into one, the sampling speed is truly 80 MHz, and the total data buffer is 640 instead of 320 words. In MACRO, however, the WFD modules were operated in uni-phase mode, under which the real sampling clock of each channel of the WFD has only half the rate of the input sampling clock, a 40 MHz real sampling speed, producing an 8 μs long WFD buffer for PMT signals.

WFD input comes from the CSPAM/FMT fan-in module (8:1) through an RG-172 50 Ω coaxial cable. Since each horizontal face has 16 scintillator tanks, a lemo T-connector combines two 8:1 inputs together into one WFD channel, which causes the signals from the horizontal faces input to the WFD to be attenuated by a factor of 3/2. For the vertical faces, there are only seven tanks in the lower part of the detector, so no attenuation is necessary.

Several different triggers prompt WFD encoding, but trigger processing times are different for each. For example, the CSPAM trigger processing time is less than a hundred ns for muons, but for the ERP it is about 6.2 μs. To properly stop the WFD without losing information, the Caltech slow monopole latch module is used. It stops each face separately, while other triggers stop each face simultaneously, but the Caltech slow monopole trigger has priority, meaning that the other triggers will be prohibited from stopping the WFD when a slow monopole trigger occurs.

A new WFD system has been designed and will soon be installed in the MACRO detector. This new system has 200 MHz sampling speed; combines only four PMT signals per WFD channel; operates with zero suppression, suppressing pulse information at -2 mV or above; and has a very long memory buffer which holds up to 32 ms. With this long memory, any PMT signal tail such as reflections from the other end of the scintillator tank, PMT after-pulses, and other late pulses such as hydrogen and helium after pulses will be recorded. The new WFD amplifier has three different slopes which give it a dynamic range of up to -10 V, with one count per mV in the range from zero to -100 mV.

4.4 Summary

As discussed above, the ERP could trigger on magnetic monopoles with velocities as low as $10^{-2}c$, but its TDC cannot cover the whole range expected for these fast monopole candidates. The FMT/CSPAM trigger system can provide additional timing for these events using the WFD. The WFD has a time buffer up to 8 μs and runs in common stop mode with 25 ns resolution, adequate for candidates with times of flight in the few μs region. However, the WFD dynamic range of only 2.0 V is too small to provide all the desired information about the monopole candidate pulse heights, but the combination of the ERP energy measurement, the FMT/CSPAM trigger system, and the WFD provides complete energy and time measurements for fast magnetic monopoles candidates in MACRO.

Chapter 5

Event Reconstruction

MACRO event reconstruction includes the energy deposition in the scintillator from the ERP ADC, the time of flight from both the ERP TDC and the WFD, and event tracks from streamer tube and strip information. We will discuss each in detail.

5.1 Overview of Event Reconstruction

MACRO performs regular weekly ERP calibrations. Both laser and LED systems are used to determine ERP ADC and TDC response in terms of phototube pulse charge and timing.

Fast monopoles' theorized large energy deposition makes the hardware trigger relatively easy, but, because the phototube gain has been set high to obtain clear single photoelectron pulses for slow moving monopoles, the PMT's respond nonlinearly to scintillation light at incident particle energy losses greater than about 120 MeV per counter. (This energy is approximately three and a half times muon minimum ionization energy with a full vertical pathlength (19 cm) in a horizontal counter.)

Accurate energy measurements, then, are a challenge for fast monopole analysis with deposited energies greater than 1 GeV. From the laser calibration, however, the ERP attenuated ADC's can be calibrated up to 8 GeV.

The theoretical scintillation light yield of fast moving monopoles depends strongly upon velocity. Good timing resolution, therefore, will help to identify candidates. The ERP TDC has 0.5 ns resolution for muons, but only a 400 ns range (as mentioned in the last chapter), which is not long enough for all FMT candidates. The WFD system, however, can provide timing information for times of flight as long as 8 μs. Its fixed 25 ns resolution translates to better than 2.5% for times of flight longer than 1 μs.

Particle tracks are reconstructed using the streamer tubes and associated pickup strips. The tracking packages are very efficient for single or multiple muon events, but less so for electronic showers. For most muon and multiple muon events, they determine the total pathlength as well as the pathlength in each scintillator tank for single muons.

5.2 Energy Reconstruction

Energy reconstruction at muon energy levels has been well described in reference [64] using the ERP unattenuated ADC, but this approach is only completely valid for energies less than four times muon minimum ionization. When the energy deposited in the scintillator is greater, the PMT's respond nonlinearly, and the ERP unattenuated ADC's are saturated; consequently, the ERP attenuated ADC must be used to obtain the correct energy. Laser calibration data are used to correct for the PMT nonlinearity. Event energies (after the primary event selection) used in this thesis, then, are reconstructed from the ERP attenuated ADC's. The energy reconstruction requires:

1. A fit of the ERP attenuated ADC to correct for PMT nonlinearity,
2. The tank response function to correct for the scintillator attenuation (position) factor, and
3. A comparison of the corrected attenuated ADC value with the mean attenuated ADC value for muons.

The reconstructed energy is defined to be the square root of the product of the two energies observed at each end (the geometric mean).

5.2.1 The PMT Nonlinearity Correction

In Appendix B, we discuss in detail the MACRO laser attenuator and the ERP responses for both unattenuated and attenuated ADC's. The ERP unattenuated ADC's respond linearly to low level scintillation light before saturating at 4095 counts, the maximum of the 12-bit ADC. The ERP attenuated ADC's, however, as the data in Figure 5.1 show, do not saturate; instead, they show a nonlinear response to high level laser light. This nonlinear response is due to the PMT's (the attenuated ADC itself is linear with the input signal). The PMT nonlinear response can be corrected for using the attenuated ADC laser calibration data.

One example of the PMT linear and nonlinear responses is shown in Figure 5.1. For each tank end, we first fit the linear and the nonlinear terms with the following functions:

$$A_a = gL + P_{ed}, \tag{5.1}$$

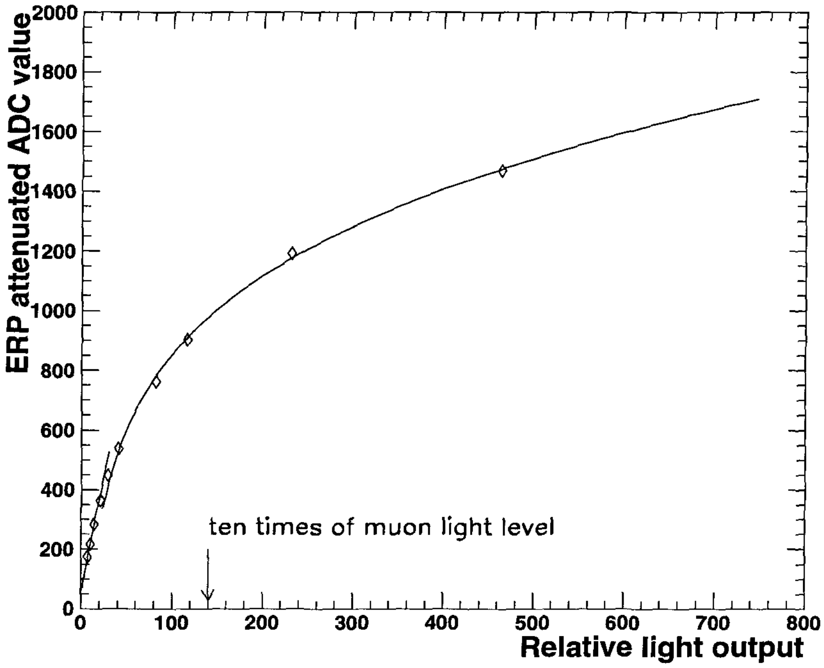

Figure 5.1: The ERP attenuated ADC value as a function of relative laser light output, with both the linear and quadratic fits.

where A_a = the ERP attenuated ADC value,
L = the relative laser light, and
g, P_{ed} = fitting slope and ADC pedestal; and

$$L = b_0 + b_1(A_a - P_{ed}) + b_2(A_a - P_{ed})^2 + b_3(A_a - P_{ed})^3 + b_4(A_a - P_{ed})^4, \qquad (5.2)$$

where b_0, b_1, b_2, b_3, b_4 = fitting constants.

The nonlinear formula is an empirical polynomial, with which we convert the ERP attenuated ADC into a relative light value, so that the linear gain can be used to obtain the corrected attenuated ADC value.

$$\langle ADC \rangle_c = gL, \qquad (5.3)$$

where $\langle ADC \rangle_c$ = the corrected ERP attenuated ADC value.

5.2.2 Event Position

The position within a scintillator tank is determined from the difference between the times that the light signal arrives at each end. The ERP TDC is in common stop mode; that is, each channel starts its own TDC provided the signal is over threshold, and all are stopped by a common signal generated by the channel which triggered first. The position formula is:

$$x_c = \frac{1}{2}(T_0 - T_1)\frac{c}{n_r}, \tag{5.4}$$

where T_0, T_1 = reconstructed times from the 0 and 1 ends,
$c = 29.98$ cm/ns, the speed of light,
n_r = the effective index of refraction of the scintillator, and
x_c = the position relative to the center of the tank.

The index of refraction of the MACRO scintillator is about 1.47, but this is effectively about $n_r = 1.587$ [64] due to reflections from the inner walls of the counter: while the actual distance from one end of a tank to the other is about 11.2 meters, the real mean distance that light travels is longer because some reflects back and forth from the inner walls along the way, making the effective index of refraction larger. Its value is obtained by comparing the position calculated from the TDC's and the position calculated from the streamer tube track, which are fit to get the speed of light in the scintillator, and hence the effective index of refraction.

5.2.3 The Position Response Function

In order to determine the energy of an event, we must know the PMT response as a function of position inside the tank. This response function results from a combination of the MACRO scintillator oil attenuation, reflection efficiency of the mirrors, and PMT acceptance and response. Since the response functions from tank to tank are almost identical [64], we use only two response functions: one for all horizontal tanks and one for all vertical tanks.

The response function is:

$$R(x) = \frac{a_1}{x^2} + a_2 e^{-x/a_3} + a_4 e^{-x/a_5}, \tag{5.5}$$

where $R(x) =$ the response function,

$x =$ distance from the end of the tank, and

$a_1, a_2, a_3, a_4, a_5 =$ fitting constants.

This semi-empirical formula includes the inverse square geometric term $(1/x^2)$ and two exponentials, one of which may be understood as attenuation due to the bulk scintillator and the other as attenuation due to reflections from the tank walls.

We cut the muon events along the scintillator counters into 14 cross-sectional strips and use the most probable value from Landau fit to the ADC values for each strip in the fit to Formula 5.5. Figure 5.2 shows these ADC values as a function of position inside and the fitted curve.

The response function is a simple correction factor and so is dimensionless. It is normalized to unity at the center of the tank. Figure 5.3 shows both the ERP raw attenuated ADC and the corrected attenuated ADC vs position along the tank. The ERP attenuated ADC's are essentially position independent after the correction.

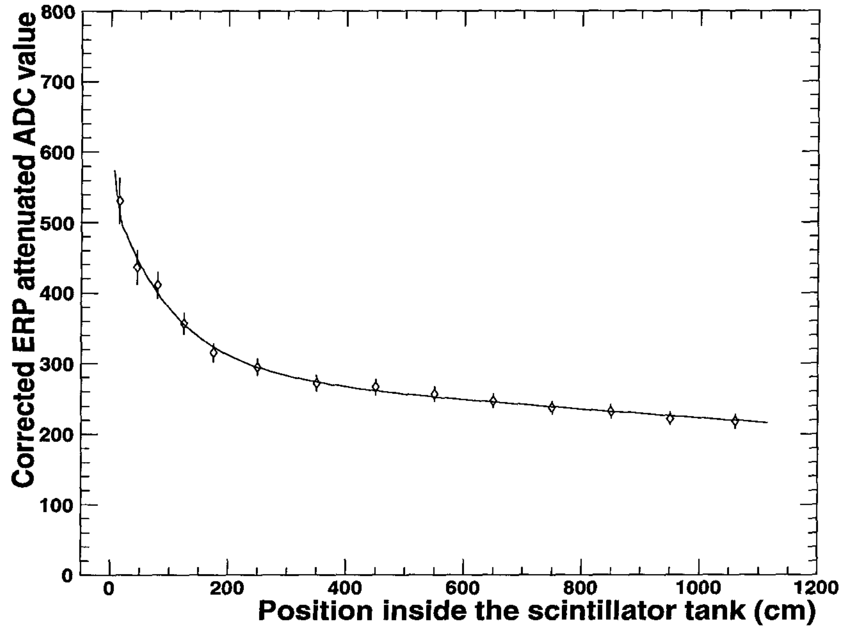

Figure 5.2: The PMT signal response for single muon events at different positions inside the tank.

5.2.4 Absolute Energy Normalization

The laser calibration can only determine relative energy deposition. Absolute energy normalization is obtained from the minimum ionization energy for single muon events. Using a collection of single muons within 100 cm of the center of a tank, we get the distribution of ERP attenuated ADC values for fixed pathlength. The most probable value of the ERP attenuated ADC, obtained from the Landau fit, is considered the attenuated ADC value corresponding to the expected muon energy. Figure 5.4 shows this distribution for tank 4B01.

The energy from each tank end is calculated from the following formula:

$$E_n = \frac{\langle ADC \rangle_c}{R(x)\langle ADC \rangle_m}, \tag{5.6}$$

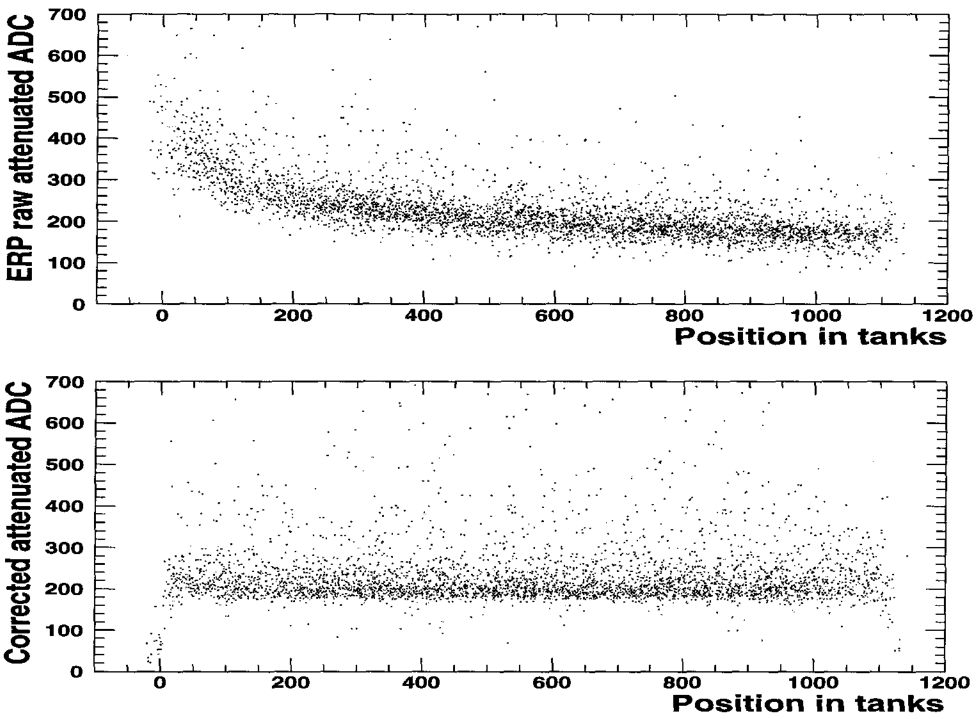

Figure 5.3: The ERP raw attenuated ADC vs position (upper plot), and after correction with the position response function (lower plot). Positions are calculated from streamer tube tracking.

where $\langle ADC \rangle_c$ = the corrected attenuated ADC value,
$\langle ADC \rangle_m$ = the mean ADC value per MeV in the center,
$R(x)$ = the response function, and
E_n = the energy from end n ($n = 0$ or 1).

The energy for the counter is calculated by taking the geometric mean of the values obtained at the two ends:

$$E = \sqrt{E_0 E_1}. \tag{5.7}$$

Ideally, the energies on both ends should be same after all corrections; historically, however, we use the above formula instead of doing a position correction. In case that no position correction is made, the reconstructed energy on each end will be different

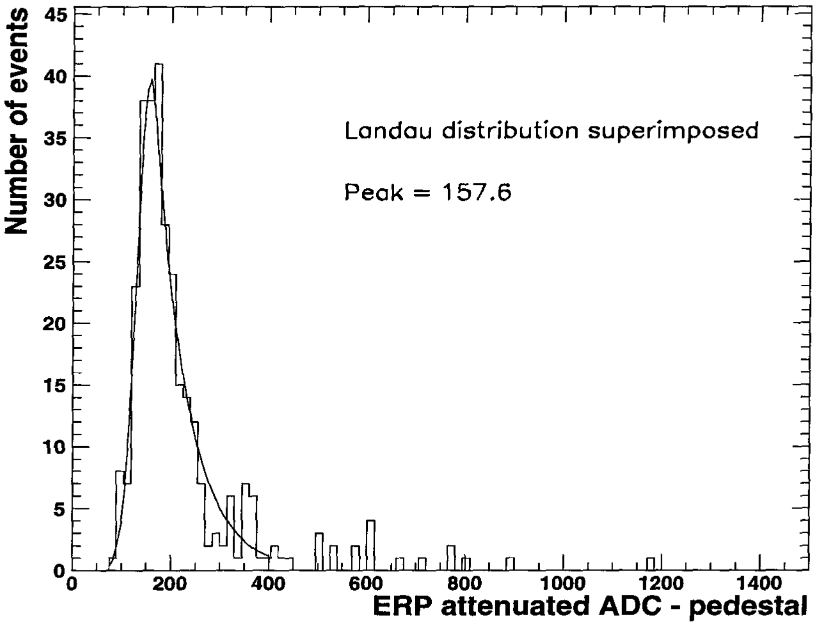

Figure 5.4: Distribution of the ERP attenuated ADC for single muon events near the center of the tank.

because the energy is approximately an exponential function of the position ($E_1 \propto e^{-x/x_0}$), where x is the position in a tank and x_0 is the scintillator attenuation length. In the case of no position correction, we use this square root of the multiplication of two energies instead of the mean value of energies on both ends to eliminate this position factor. We use this formula even though we have corrected for the position factor in this analysis.

5.2.5 Energy Calibration Quality

The quality of the energy calibration depends very much on the stability of the scintillator system as well as the ERP electronics. As shown in Figure 5.1, the PMT saturates at high energy, where a small change in ADC value could produce a large change in the reconstructed energy. Figure 5.5 shows boundaries of the uncertainty in the ERP attenuated ADC correction.

The laser calibrations performed for the data sample used in this thesis ("six-month-run" data) was only up to 2 GeV which is below the ERP attenuated ADC limit. We extrapolate the fit and use these fitting results for larger energy reconstruction in this analysis. In early 1994 after "six-month-run," we took laser calibrations for the ERP system up to its hardware limit. The data showed that the reconstructed energy limit from the ERP attenuated ADC was about 8 GeV in the worst case, and was consistent with the "six-month-run" data.

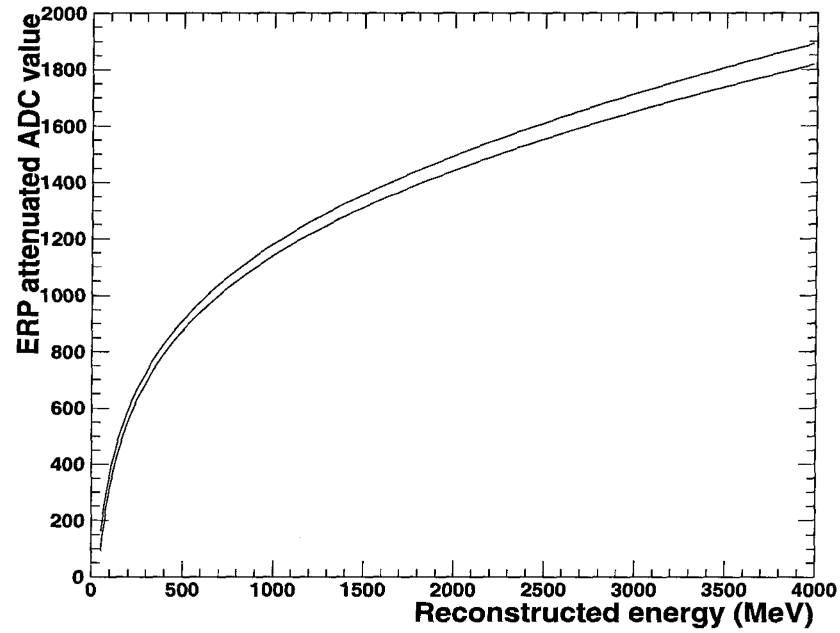

Figure 5.5: The uncertainty of the energy reconstruction (from laser calibrations).

Energy reconstruction errors are mainly due to the saturation correction error (errors from the position correction are negligible). The light level of the calibration data extend to the equivalent of a couple of GeV, for which the corresponding energy error (at 2 GeV) is about 10%, and the fitting results can be extrapolated to several GeV with about 20% error. The upper limit of the energy calibration is approximately 8 GeV in the worst case as mentioned above, limited by the ERP ADC integration gate and the PMT pulse height saturation. (The actual maximum calibration energy varies from tank to tank, and for some can reach 15 GeV. In this analysis, we will assume the worst case value.) The error from the energy normalization, less than 2% from the muon peak fitting, is an additional contribution.

We state that the above reconstructed energy is the energy deposited inside each scintillator tank by an incident particle, but this statement is not precise. The reconstructed energy is actually the equivalent energy for the light produced by the incident particle. From the discussions in Chapter 3, we know that the scintillation light yield is proportional to the energy loss rate at low energy while it is heavily saturated at high levels [78]. In this case, the light yield equivalent energy is not proportional to the energy loss rate of the incident particles; the saturation for fast monopoles, however, has been included in the calculation of the light yield.

5.3 Timing Calibration

Timing calibrations are necessary to determine the time of flight (TOF) of particles crossing the MACRO detector, and thus their velocities. For relativistic particles, the TOF is less than 400 ns, and the ERP TDC is used. For non-relativistic particles, the ERP TDC is saturated, and we rely on the WFD. We will discuss the ERP TDC calibration here, and the longer WFD TOF timing calibration in Section 5.4.

There are three major steps required to calibrate the ERP TDC. First, the TDC slope (counts per nanosecond) is calculated; second, the timing offset of each TDC channel, including cable and electronic delay, is calculated; and third, since fixed threshold discriminators are used, a correction for signal size is made (the "time walk correction"). All three can be obtained from LED calibration data and muon events.

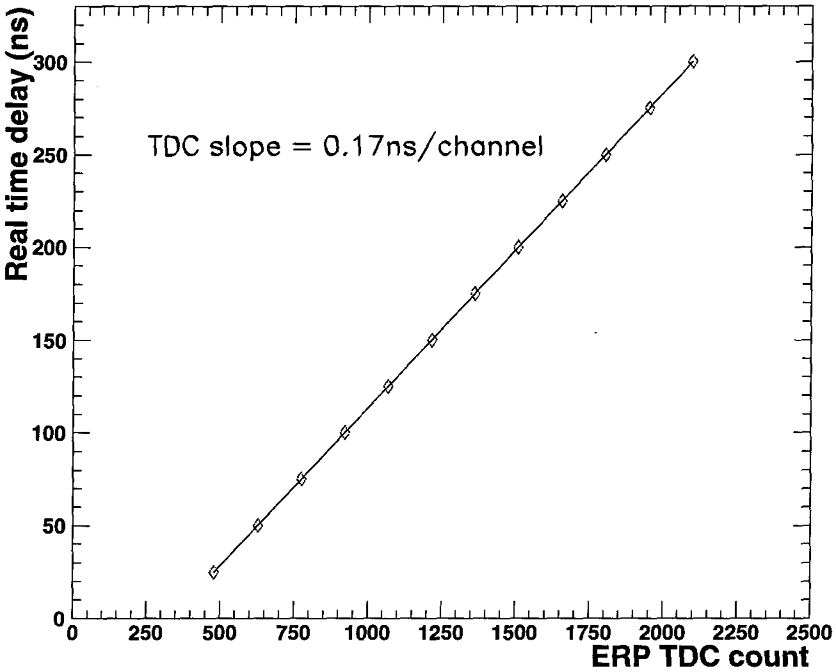

Figure 5.6: An example of TDC slope fitting.

5.3.1 TDC Slope

A CAMAC controlled pulse generator allows triggering of each tank end with different time delays. This yields TDC values as a linear function of delay, the slope of which corresponds to the TDC value per nanosecond, and the intercept of which yields the relative timing offset. Figure 5.6 shows an example. The fitting formula is:

$$\langle TDC \rangle = \langle slope \rangle \times T + P_0, \tag{5.8}$$

where $\langle slope \rangle$ = fitting slope,

T = time in ns controlled by pulse generator, and

P_0 = TDC offset.

Note that the offset determined above is not used in the time of flight calculations because there is some jitter in LED light delivery time from tank to tank. A more accurate determination of the offset is discussed in Section 5.3.3.

5.3.2 Time Walk

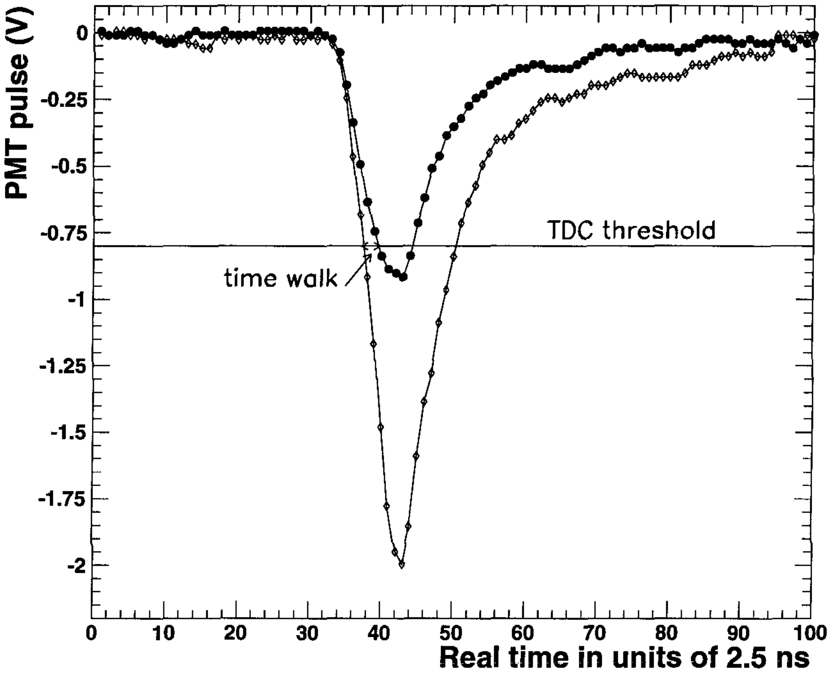

Figure 5.7: Time walk caused by different sized pulses. The two pulses are taken with LeCroy module 3011 digital scope with 400 MHz sampling clock.

Time walk is a systematic shift in the recording time caused by a variation in TDC triggering times at different pulse heights. For a fixed TDC trigger threshold, differently sized pulses pass the threshold at different times even though they begin at the same time. Clearly, it takes longer time for a smaller pulse (*i.e.*, far from the PMT) to cross the TDC threshold, as seen in Figure 5.7.

Time walk is determined by recording a set of pulses of different heights but with the same delay. The TDC time difference (time walk) can be parameterized using the following empirical function:

$$T_{tw} = \frac{d_1}{\sqrt{\langle ADC\rangle - \langle ped\rangle}} + \frac{d_2}{\langle ADC\rangle - \langle ped\rangle}, \tag{5.9}$$

where T_{tw} = the time walk,

$\langle ADC\rangle$ = the ERP unattenuated ADC value,

$\langle ped\rangle$ = the ERP unattenuated ADC pedestal, and

d_1, d_2 = fitting constants.

In reference [64], page 44-47, there is suggested a reason for choosing this formula. It has been shown that the time walk is a power series of $1/\sqrt{V}$, where V is the pulse height. We use the ERP ADC value instead of the pulse height because the pulse height is not directly measured in the ERP. Figure 5.8 shows the time walk fit, which improves resolution by a factor of two to 0.5 ns.

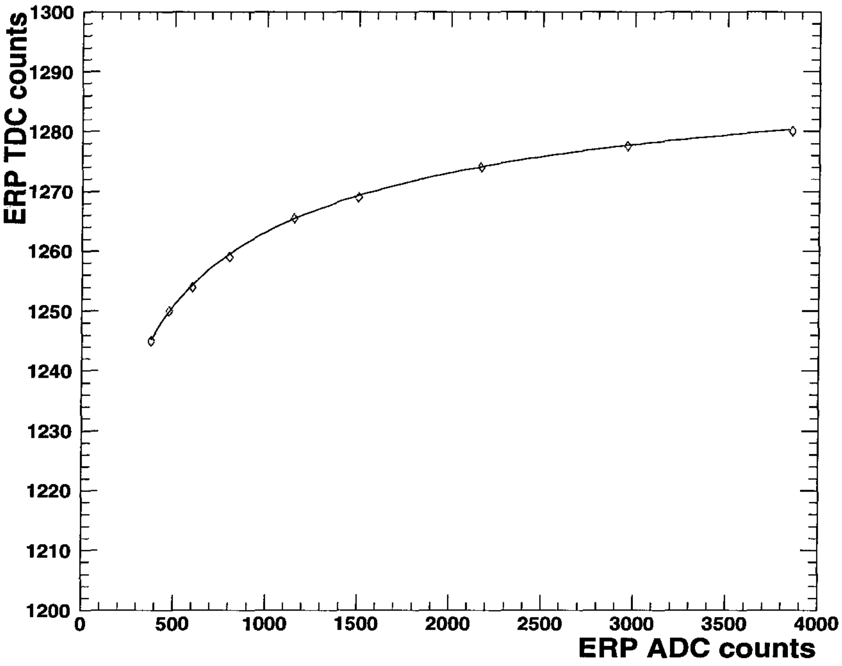

Figure 5.8: An example of the time walk fit.

5.3.3 TDC Offset

The TDC offset is caused by cable delays, PMT response, and electronics delays. It is difficult to know these offsets precisely, so the ERP TDC offset is calibrated from muon events. Single wire and strip tracks are required to eliminate shower and multiple muon events that can confuse the TDC start.

In all applications of the TDC, only the difference between the two ends of a counter or the difference between two counters (TOF) is used. Therefore, only the relative offset is important. Two types of relative offsets are calculated using real muon events: the two-side offset between the two ends of one scintillator counter, and the two-counter offset between two different scintillator counters.

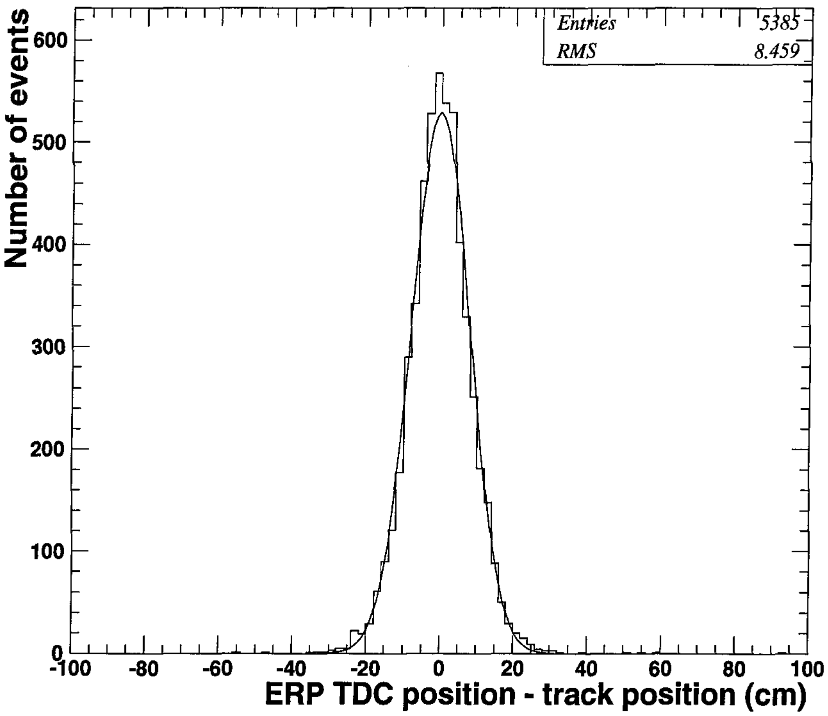

Figure 5.9: The difference between the ERP TDC and the track position.

For the two-side offset, we compare the position determined from the timewalk corrected TDC to the position from the streamer tube track, then adjust the offset so that two positions are consistent. Figure 5.9 shows the distribution of the difference between the offset corrected TDC and track positions. The events are from the horizontal tanks of SM1. The σ is less than 10 cm, which corresponds to less than 0.5 ns.

After calibrating the two-side offsets for each counter, we can calculate the TOF from two different counters for single muons and adjust the offset so that $1/\beta = 1$. We use $1/\beta$ instead of β because $1/\beta$ is proportional to time of light, and for a fixed pathlength in the detector is expected to have a Gaussian distribution. The two-counter offsets are also well calibrated, with errors of not more than 0.5 ns as discussed in the following section.

5.3.4 Time of Flight

The time of an event hitting each tank is determined from the mean time at both ends. Figure 5.10 demonstrates the geometry.

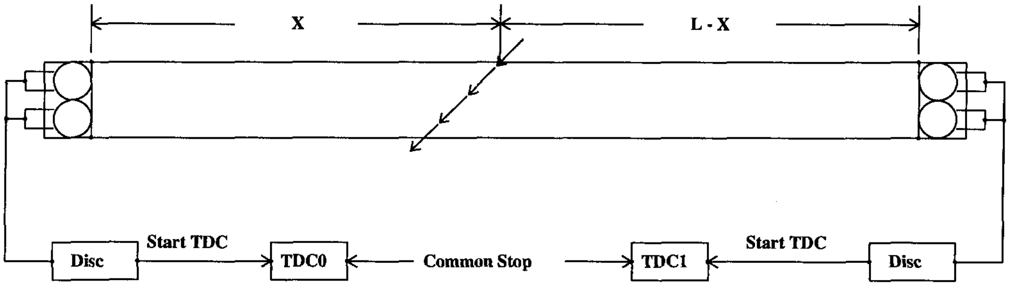

Figure 5.10: The layout of the ERP TDC.

We use the following formulae to calculate the time:

$$T_{top1} = T_{passage} + X/v + T_{delay1}, \quad \text{and} \tag{5.10}$$

$$T_{top2} = T_{passage} + (L - X)/v + T_{delay2}, \tag{5.11}$$

where $T_{passage}$ = the time when an event hits the tank,
X = the event position inside the tank,
v = the speed of light in the scintillator, and
L = the scintillator tank length.

The time of an event hitting the tank is calculated through:

$$T_{passage} = \frac{1}{2}(T_{top1} - T_{delay1} + T_{top2} - T_{delay2} + L/v) \tag{5.12}$$

With the delay corrected TDC, $T_1 = T_{top1} - T_{delay1}$ and $T_2 = T_{top2} - T_{delay2}$, so we have:

$$T_{passage} = \frac{1}{2}(T_1 + T_2 + L/v) \tag{5.13}$$

The difference between the times for two tanks on different faces of the detector gives the time-of-flight (TOF):

$$\langle TOF \rangle = T_{passage1} - T_{passage2}, \quad \text{or} \tag{5.14}$$

$$\langle TOF \rangle = \frac{1}{2}(T_1 + T_2 - T_3 - T_4), \tag{5.15}$$

where T_1, T_2 = the corrected time for both ends of the top tank, and
T_3, T_4 = the corrected time for both ends of the bottom tank.

The MACRO ERP TDC system, after calibration, gives a time resolution of 0.5 ns. This is seen in the distribution of $1/\beta$ for single muon events in Figure 5.11. The σ of the above Gaussian distribution in $1/\beta$ is 0.03, corresponding to the resolution in timing of 0.5 ns.

Although the time resolution of the MACRO scintillator system is quite good

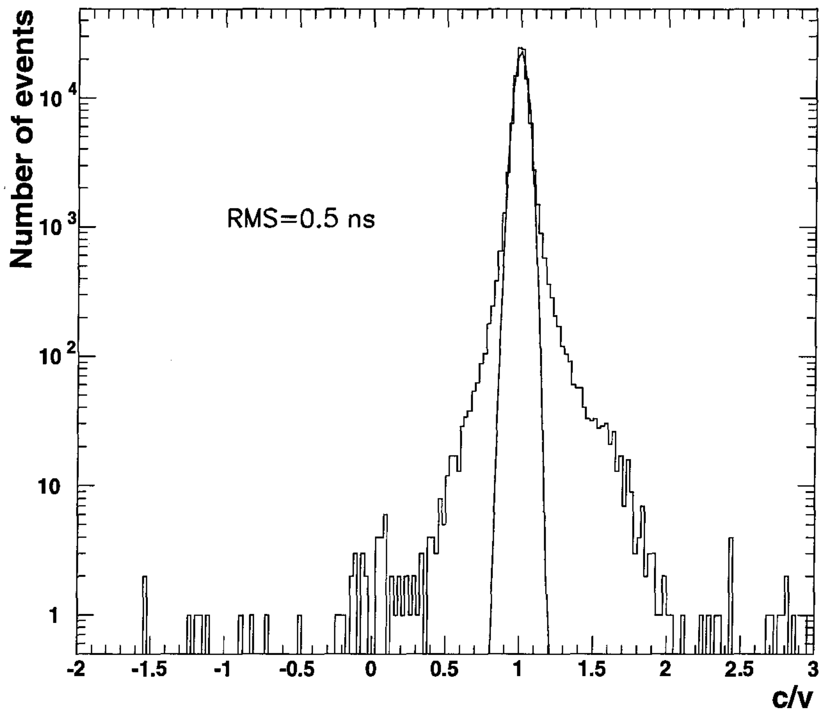

Figure 5.11: The distribution of $1/\beta$ for single muon events.

(0.5 ns), the distribution of $1/\beta$ still has non-gaussian tails on both ends. Some cases which can produce the incorrect timing information which cause these tails are radioactivity decay nearly coincident with the passage of a muon, multiple muons in a single event, and muons accompanied by showers. In fact, applying some stringent cuts on these types of events can eliminate the non-gaussian tails. MACRO has successfully performed these requirements [65] and obtains an upward going muon peak near $1/\beta = -1$. For monopole analysis, we only use absolute timing and the $\beta = |v|/c$.

5.4 WFD Reconstruction

Since it extends beyond the range of the ERP (400 ns), the WFD is used for fast moving monopole trigger timing as well as providing a tool to study the signal waveforms. This is particularly important when we look for rare events with heavy ionization because the WFD provides rejection of multiple muons which could be confusing if only the ADC were recorded. The WFD can also distinguish shower events from a large signal due to a single crossing particle.

Because each channel of the WFD has a buffer of only 8 μs, the MACRO WFD system is stopped in two different modes. The "common stop mode" is used for the muon triggers and the FMT because the TOF of particles from these should be within that time window. A separate stop mode is used for the slow monopole trigger, for which the TOF can be as long as 500 μs. In this mode, each face of the WFD is stopped immediately after the trigger occurs in that face.

Waveform reconstruction involves reading out the waveforms from triggered channels, fitting them, and correcting the baseline. For fast particle triggers, one can also get the TOF by comparing the event times from two different faces.

5.4.1 Waveform Baseline Correction

For some WFD channels the baseline is not stable, as shown in Figure 5.12 which contains the WFD readout from two different channels, one with a stable baseline, the other with baseline drift.* A least-squares-fit program is applied to fit the true baseline, first fitting with all points, then a second time eliminating points which lie three sigma or more away from the first result. Figure 5.13 shows the results of

---

*The WFD module is a charge coupling device (CCD), which has a nonzero baseline. The charge for each sample of the baseline voltage is held by a cell in CCD before it is digitized, giving an unstable baseline when the CCD is leaky.

baseline correction.

The WFD has 1.0 mV/count gain, and a dynamic range of around 2.0 V, which is insufficient to record very large pulses. In fact, the WFD can even be saturated if a muon passes close to a tank end. Although for the subject of this particular thesis a smaller PMT gain would be preferred to minimize this problem, in fact, in MACRO the PMT gain is high to guarantee that for slow monopole detection the single photoelectron pulses will stand significantly above the baseline noise.

5.4.2 WFD Timing

The WFD has a common sampling clock which cycles at 80 MHz. The cable delay is identical for every channel to ensure that measured times are comparable in common stop mode. It can be seen from muon events that these cable delays are consistent because the TOF of a typical muon from the center to the bottom face is only 15 ns, and with the 80 MHz sampling clock, the muon pulses from these two different faces appear in simultaneous or consecutive samples. Figure 5.14 shows the waveform of a typical muon for which the pulse height (this case in a horizontal tank) is about 1.5 V.

For TOF's less than 400 ns, precise timing can be obtained from the ERP TDC. For particles with TOF longer than 400 ns, however, the WFD supplies timing with a 25 ns resolution, an accuracy of better than 6% (better than 2.5% for TOF greater than 1 μs). Obviously, the longer the TOF, the better the relative resolution.

Figure 5.15 shows a muon decay, demonstrating the WFD timing resolution. The timing for this event is about 3.4 μs. The muon hits tank 5C08 in the center face, passes through the detector, then decays just above 5B10. The decay electron ends up in tank 5B10 in bottom face. The energy deposited in tank 5C08 is 30.5 MeV while in tank 5B10 it is 20.5 MeV. There is a clear streamer tube track, and both

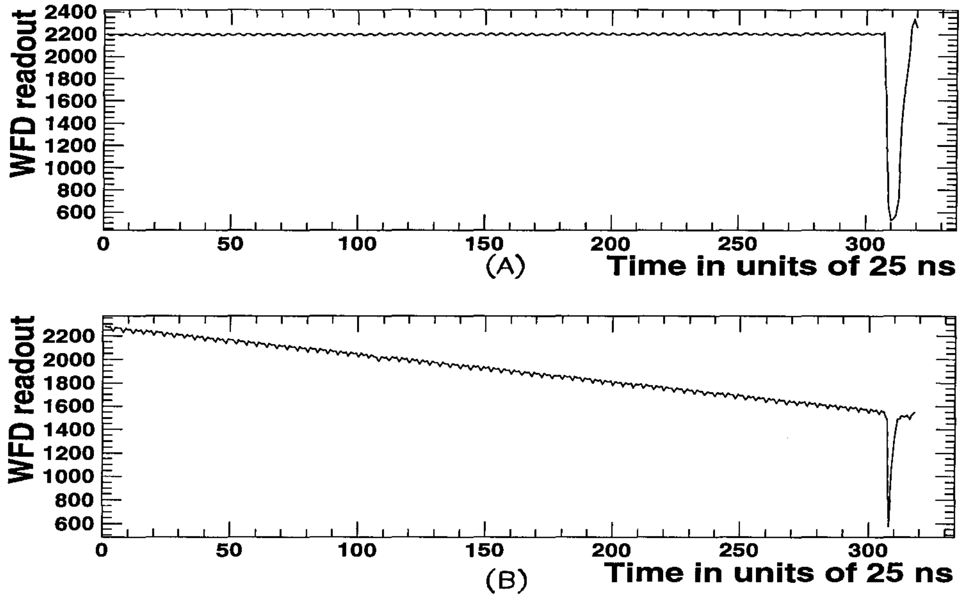

Figure 5.12: (A) is a WFD readout with a stable baseline. (B) is a WFD readout with a drifting baseline. The WFD gain is about 1 count/mV.

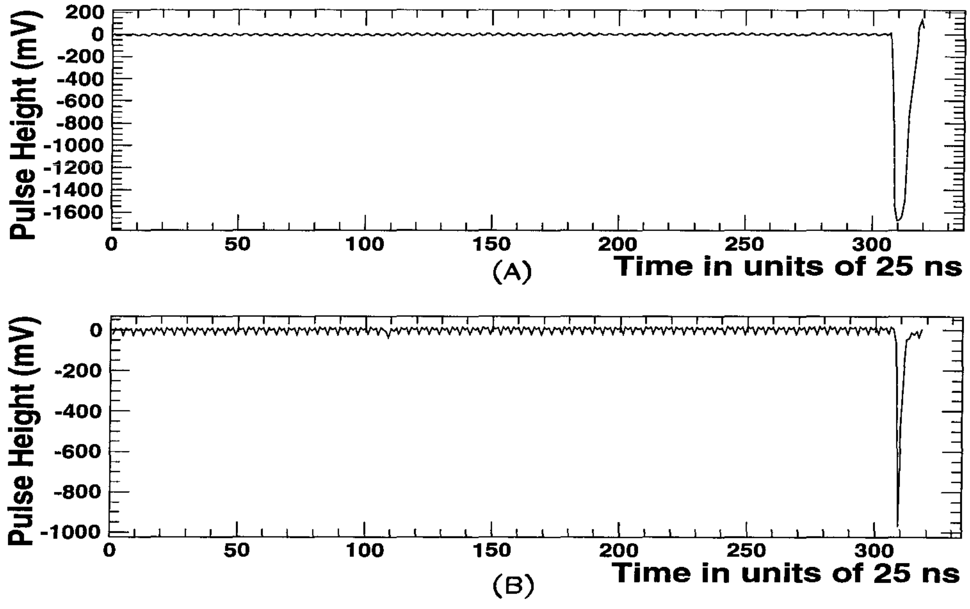

Figure 5.13: (A) and (B) are the baseline corrected WFD plots corresponding to Figure 5.12.

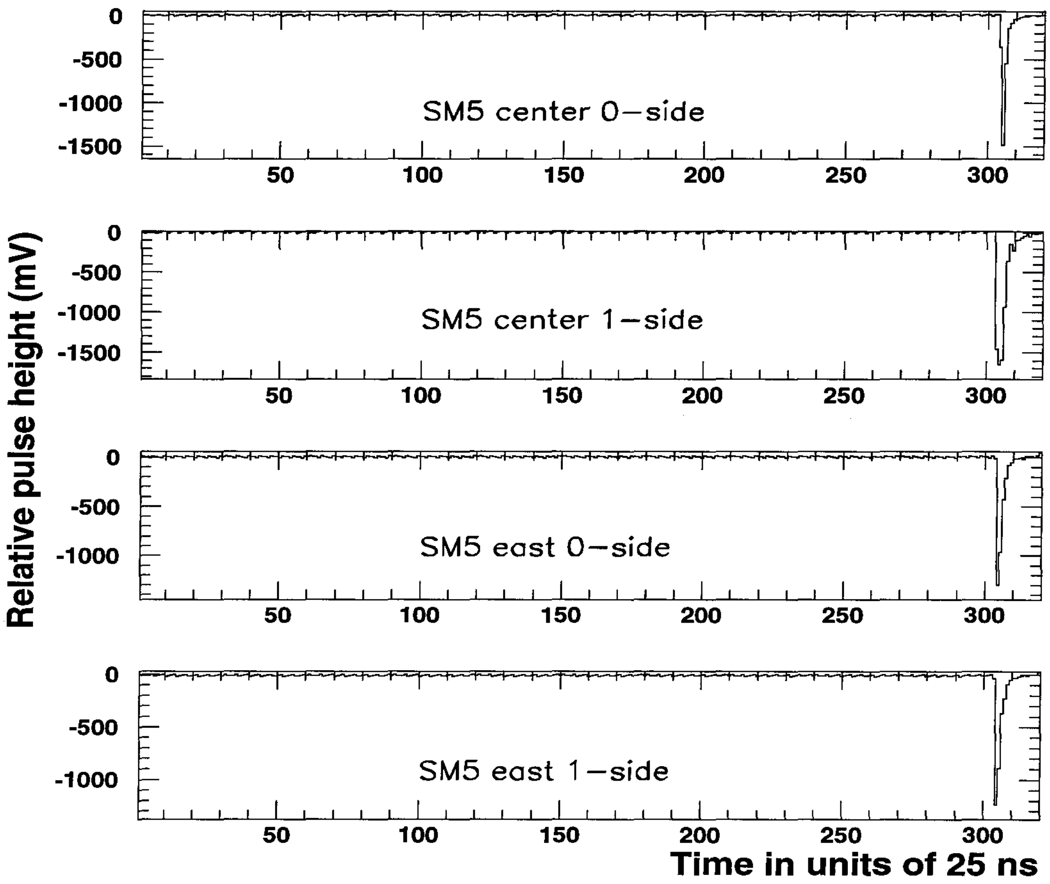

Figure 5.14: A typical muon waveform. The event is run 6011, event 2.

the streamer tubes and strips show that the muon changes direction near the end, indicating that it slows down. The timing accuracy for this event is less than 1%.

5.5 Event Tracking

When there are both streamer tube and strip hits, an event track can be found and fitted to provide accurate position and angle information, which can then be used to determine the pathlength in the scintillator counter and the flight distance across

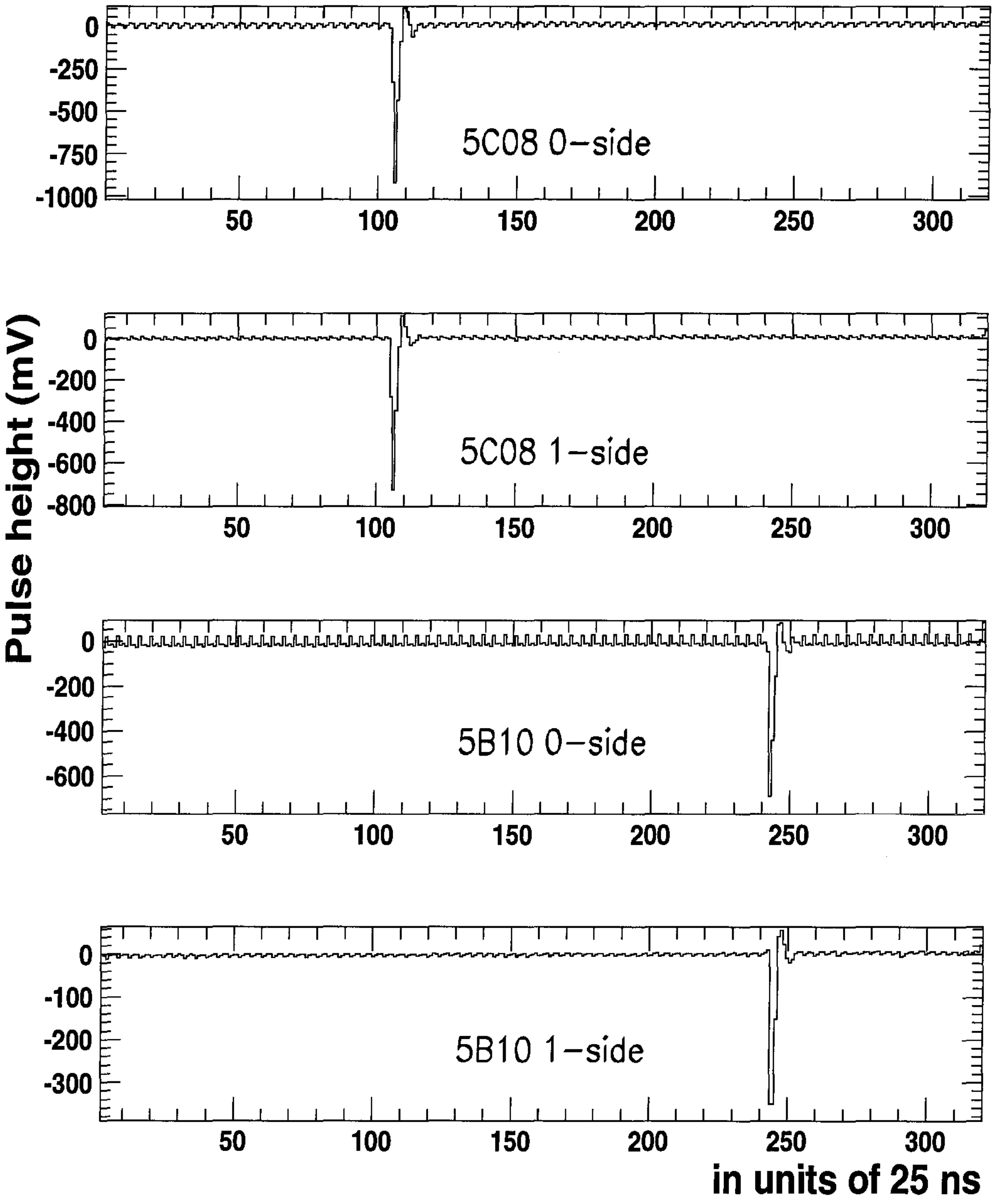

Figure 5.15: The WFD record for a muon decay. The event is run 6013, event 7706. The TOF obtained by comparing signals from the two faces is 3.4 μs.

the detector.

Three different track packages have been developed for MACRO. They are:

CATRAK written by Caterina Bloise [80] which uses only horizontal streamer tube hits to find tracks in both the wire (XZ) and strip (DZ) views,

LATRAK written by Paolo Bernardini, which uses lateral and central streamer tube hits to find tracks in the YZ view, and

SPURIO written by Maurizio Spurio [81], which combines horizontal and lateral streamer tube hits to get tracks in both the wire and the strip views.

The ten layers of streamer tubes that lie along the direction of the horizontal tanks provide the X view; the ten pickup strips are placed at an angle of 26.5° with respect to the wires, and provide the D view; Z is in the vertical direction; and Y lies along the vertical tanks.

For CATRAK, a least-squares-fit is used to pick up hits from each plane as a track in both the wire (XZ) and the strip (DZ) views. Because the strips are at an angle of about $\theta = 26.5°$ with respect to the wires, the YZ view is obtained from Y = D/cosθ - Xcotθ.

Figure 5.16 shows a typical muon track in both the wire and the strip view. The solid scintillator boxes are the ERP hits while the open boxes do not have ERP triggers. The asterisks mark wire or strip hits used to fit the track while the open circle hits are not.

The lateral track from the vertical faces only includes the wire view because there are no strips for the lateral streamer tubes. Hence, lateral tracks alone cannot determine the position and must be associated with a central track or the ERP TDC.

Space resolution is $\sigma(w) = 1.1$ cm for the wires, and $\sigma(s) = 1.6$ cm for the strips, corresponding to an intrinsic angular resolution of 0.2° [52] for muons crossing ten horizontal planes. Due to the multiple Coulomb scattering in the rock overburden, however, the effective overall resolution with respect to the original muon direction is about 1.0° [52].

The track packages work well for single muon events, with more than 95% tracking efficiency, but they do not work as well for showering events because extra hits spread out over the wire and strip planes. These shower events must be treated carefully. In this thesis, we use the track packages for single and multiple muon events when available, but tracks are not required as discussed in the next chapter. For shower events, however, we do not rely on the track, but rather use other methods to identify them such as visually scanning the hits. Our analysis is thus not limited by the tracking efficiency.

5.6 Conclusion

The MACRO event reconstruction packages for both scintillator and streamer tube systems should work well for fast magnetic monopole candidates. The energy reconstruction from the ERP attenuated ADC is up to a minimum of 8 GeV, with errors of less than 12% at less than 2 GeV, and of about 22% at greater than 4 GeV. MACRO also provides accurate timing resolution of 0.5 ns from the ERP TDC for time of flight less than 400 ns. For time of flight from 400 ns to 8 μs, the timing resolution is 25 ns as obtained from the WFD. The streamer tube and strip tracking programs work well for single and multiple muon events, with single muon efficiency greater than 96%, spatial resolution of about 1 cm, and angular resolution of about 0.2°.

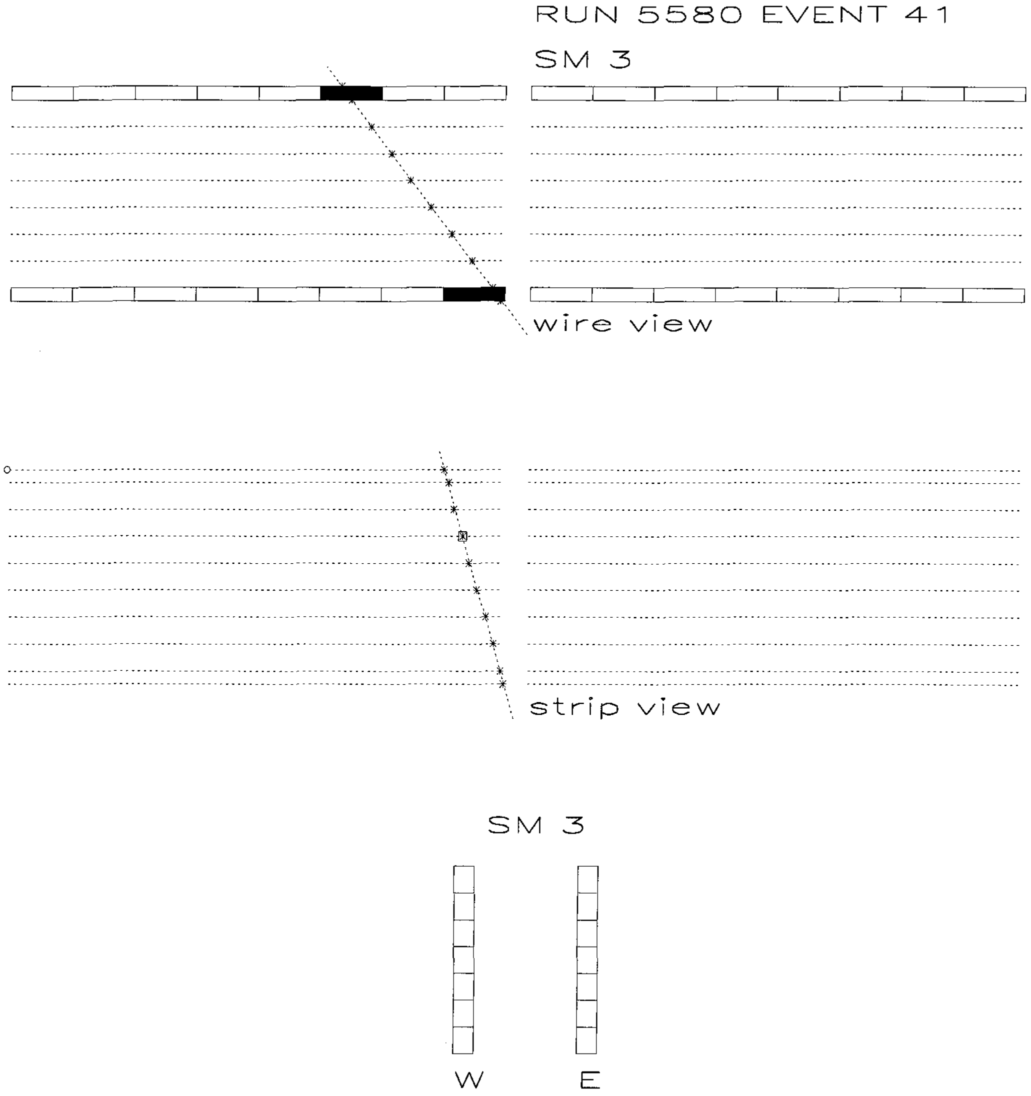

Figure 5.16: A typical muon event has a track from both the wire view and the strip view. The event is located in SM3, passing through tank 3C06 in the center face and 3B08 in the bottom face as indicated with the two solid boxes. All ten layers of streamer tubes are triggered as well as all ten layers of strips. Tracks on both the wire (XZ) view and strip (DZ) view are used to calculate the exact location and the angle.

Chapter 6

Fast Monopole Data Analysis

As discussed Chapter 3, the theoretical scintillation light yield for fast moving magnetic monopoles is quite high compared with that produced by muons. This predicates that searching for events with extremely high energy deposition should be our basic approach in this analysis. Using ERP energy and timing calibrations and the waveform information, we employ several criteria to exclude most events in the high energy background of multiple muons and muon induced showers. The selected data sample, however, still includes many events, especially from the sample of showers. Because the energy deposition from these can be quite large, other information, specifically from the streamer tubes and strips, must be used for background rejection.

The energy limit of the ERP ADC, about 8 GeV as described in the last chapter, is more than 200 times the median energy deposition of muons, but for fast moving monopoles, it would be better if this limit were higher. Because it is lower than that expected for fast monopoles with full vertical pathlength (19 cm or 43 cm, for horizontal and vertical tanks, respectively), it is difficult to select events based on one-face scintillator information. Therefore, two faces are required for every candidate, meaning that every candidate must have consistently high energy in scintillator tanks in two different faces. If any event were to satisfy this requirement, other independent confirmation such as from the track-etch detector could also be required.

In this chapter we discuss each step of the fast moving magnetic monopole data analysis, from primary event selection to the application of all the different physics cuts, which include both WFD and streamer tube information. We will also discuss visual scans of the remaining events and the ultimate exclusion of all. Finally, we calculate the detector acceptance, and since no monopole was found in this data sample, we determine a flux limit for fast moving magnetic monopoles.

6.1 Event Selection

The data sample included in this analysis is from the "six-month-run," which started December 10, 1992, and ended July 1, 1993. During this period, the full MACRO area (but only the lower part) of six supermodules was in operation, excluding the north and south faces.

The data include a total of 673 regular runs, excluding the regular Tuesday calibration runs. The event rate (mostly from cosmic ray muons) is approximately 0.2 Hz with all six SM's running (Figure 6.1 shows the distribution). The size of the largest peak shows that all SM's were in operation for the majority of the runs. There are also two small peaks in the plot, corresponding to two and four SM's operations, when other parts of the detector were undergoing calibration or maintenance.

Primary event selection is based on the ERP trigger only. In order to use the inter-ERP events, which cross two or more SM's, we combine the ERP triggers from all SM's and treat the entire detector with four faces: center, bottom, west, and

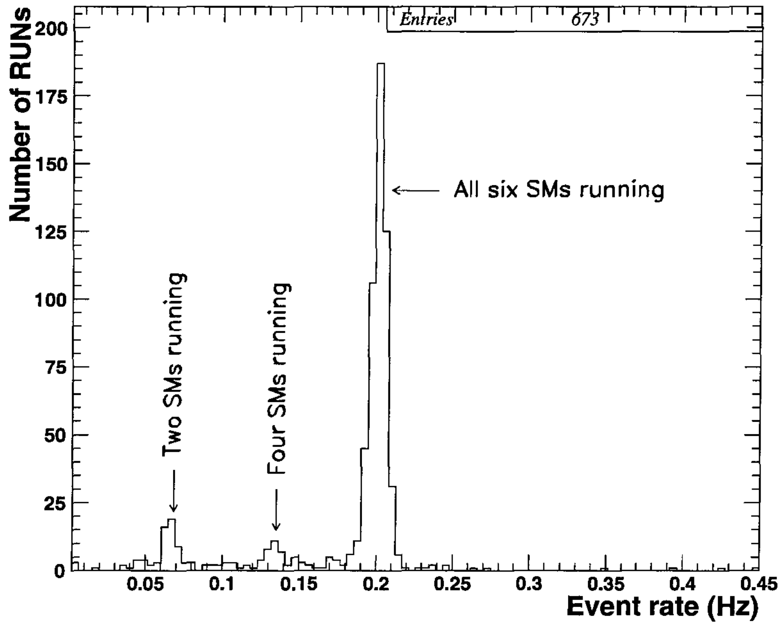

Figure 6.1: The event rate distribution.

east, each face consisting of the six corresponding faces of the six individual SM's. Based on this configuration, we select those events which meet the following two requirements:

1. The event must be a two-face or more ERP event, and
2. The largest energy from a single tank in each face is used, and the event must have at least two faces, for which this largest energy is greater than 120 MeV.

The 120 MeV cut is slightly greater than three times the energy deposited by a typical vertical muon in a horizontal tank (pathlength 19 cm), and it is roughly the PMT linear response limit. It is equivalent to the light generated by a magnetic monopole with a velocity of $10^{-2}c$ (the lower limit for this search) in less than two centimeters in MACRO scintillator. Figure 6.2 shows the energy distribution of single scintillator tank energy deposition for two-face ERP events. The peak value is about 34.5 MeV. The long tail is caused by muon induced showers, multiple muon events, and any possible high ionization particles. Figure 6.2 also shows the 120 MeV

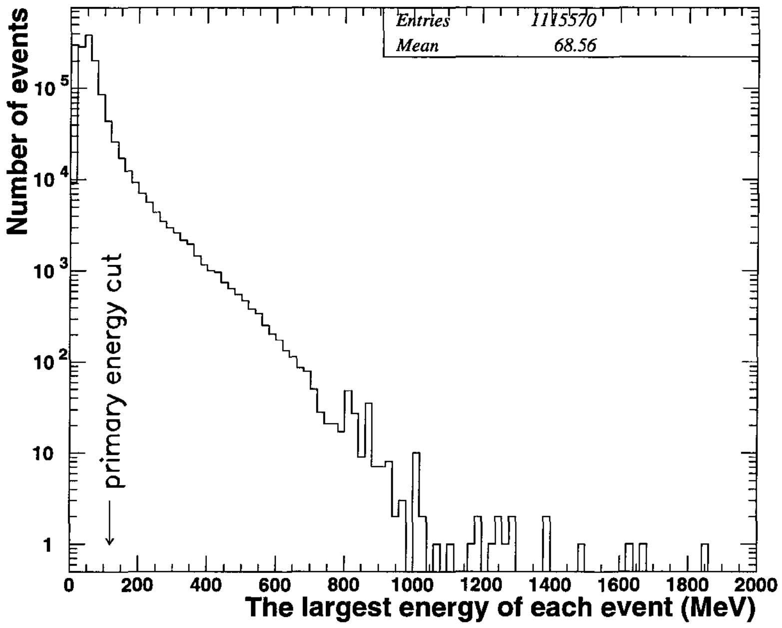

Figure 6.2: The energy distribution of two-face ERP events.

cut, which eliminates most single muon events, but keeps those whose energies lie on the tail. The reconstructed energy used in the primary event selection is calculated using the MACRO standard energy calibration data of the ERP unattenuated ADC [64], for which the error at 120 MeV is about 5%. No tracking information is used, so no pathlength correction is included. For the selected events, the energy will also be reconstructed using the ERP attenuated ADC's as described in the last chapter.

Because no track information is used in the primary event selection, and because the geometries of horizontal and vertical tanks are different, the 120 MeV requirement is more stringent for horizontal tanks than for vertical tanks because the mean pathlength of events in vertical boxes is longer than that in horizontal boxes. As a result, a considerable number of the events selected under this requirement involve vertical faces.

There are a total of 4.7 million single SM ERP triggers. Of these, 2.65 million are two-face ERP events; of those, however, only 14,424 are selected by the primary energy cut (0.5%). Table 6.1 summarizes the effects of the event selection requirements. The remainder of this chapter concerns the detailed analysis of these candidates.

Total runs	673
Total run time	229 days
Total ERP triggers	$4.7\ 10^6$
Total two-face ERP triggers	$2.65\ 10^6$
Total events selected after 120 MeV energy cut	14,424

Table 6.1: Statistics of "six-month-run" data sample.

6.2 Physics Analysis

The primary event selection uses only unattenuated ERP ADC information. For further analysis, however, we use all possible information to identify each event, including ERP attenuated ADC, the WFD, streamer tube, and strip information.

The selected events can be classified in five basic groups:

1. Muon induced showers,
2. Multiple muon events,
3. Spurious laser calibration events,
4. High energy muons, and
5. The remaining fast monopole candidates.

Muon induced shower events are selected because they produce many low energy particles, many of which deposit their energy in the scintillator, so that the integral signal is large. There are also multiple muon events with two or even three tracks passing through the same pair of tanks, for which the deposited energies are again higher than the mean. A small fraction of events are single muon events with unusually high energy deposition due to bremsstrahlung and/or pair production. It is also possible that some muons accidentally coincide with radioactivity in the same tank near the phototube, which can result in large reconstructed energies. Some laser events are also selected because occasionally the laser spontaneously triggers during regular runs. The laser attenuator setting for these events is determined by whatever setting was left from the previous calibration, and if it is low enough, the reconstructed energy can be more than 120 MeV.

Using the ERP TDC, ERP attenuated ADC, WFD, and both streamer tube and strip tracks, we are able to make several additional physics cuts which eliminate more background events from the selected data sample. We will discuss each of these cuts, which are performed in series, in detail.

6.2.1 The Laser Cut

Generally, laser events can be easily identified because the scintillator pattern unit (SPU) records every laser event if it triggers during a regular run, but the SPU sometimes fails to record spontaneously triggering laser events. Such spontaneous triggering occurs in almost all SM's, but is much more frequent in SM1 and in SM5 than in the other four.

We can use the ERP to identify those laser events without an SPU record based on the fact that laser light should appear in every tank simultaneously and the laser fiber in most tanks is located within 50 cm of the center of the tank. Therefore, we use the following to identify a laser event:

1. The total number of ERP box hits is more than ten,
2. There is no track from either the streamer tubes or the strips,
3. The number of random extra streamer tubes hits is less than ten,
4. 90% of the ERP reconstructed positions are within a 100 cm region at the center of the tank, and
5. 95% of the trigger times of the ERP hits are within eight nanoseconds of one another.

The first three requirements ensure that we do not misidentify real events. The σ of the distribution of time differences among ERP TDC's is about 2.5 ns for laser events, so the requirement that 95% of the tanks have TDC differences less than eight nanoseconds corresponds to about three σ in the TDC distribution. The laser cut identifies 1,649 events, leaving 12,775 candidates.

6.2.2 The WFD Saturation Cut

Muon showers or regular muons accidentally coincident with radioactivity have wider pulses than regular muons in the WFD. When a secondary shower hit occurs at a slightly different time from the primary muon pulse, for instance, the peak is not affected, but the pulse is wider than usual. Also, when secondary particles are widely separated from the original muon hit, the pulse again becomes wider, but its height may not change. Obviously, wider pulses will be integrated into larger ADC values, which result in larger reconstructed energies. Such cases cannot be identified from the ERP ADC information alone, but it is possible to discover them with the WFD.

The WFD has a dynamic range of approximately two volts, which is sufficient for normal muon pulses at the center of the horizontal tanks, which typically have heights of about 1.5 V. Because a lemo "T" connector is used to combine two inputs into one WFD channel for the horizontal faces, the signal is attenuated by a factor of 3/2 as discussed in Section 5.4. Hence, the normal muon signal from the center of a tank is near 1.0 V from the WFD.

Normally, an energy deposition of 120 MeV at the center of a tank should correspond roughly to about 5.1 V, or to 3.3 V if it occurs at the far end. Because of the attenuation factor, however, the pulse height corresponding to 120 MeV energy at the far end of a tank is actually about 2.2 V at the WFD. Nevertheless, events with 120 MeV reconstructed energy—more than three times energy deposition of a regular muon—should have a pulse height greater than 2 V no matter where in the tank the muon hit occurs. In other words, pulses at both sides should saturate the WFD dynamic range no matter where the events happens inside a tank, if the energy deposition is indeed 120 MeV or more. However, due to the slow sampling clock (25 ns), the actual WFD pulse height can be lower if the peak falls between samples. In order to guarantee that the pulse heights on both ends of a tank saturate the WFD dynamic range for events close to one end, then the equivalent energy deposition inside a scintillator tank must be more than 180 MeV in the worst case. For vertical tanks, because there is no extra attenuation, the equivalent energy deposition for pulses which saturate the WFD on the both ends is about 150 MeV for events close to one end.

The WFD saturation cut requires that the pulses in both ends of the tanks from both faces must saturate the WFD dynamic range. Only 2,477 events survive.

This cut performs a double check to the large energy deposition, but it actually also raises the energy threshold a bit as explained above, and does reduce the acceptance by only less than 1%. In addition, the efficiency for fast monopole detection is not 100% because of occasional cable disconnection. Comparing penetrating muon events in both the ERP ADC and the WFD record, we obtain a WFD efficiency of

95.2%, which applies to the fast monopoles analysis as well.

6.2.3 The Pathlength Cut

The pathlength is the flight distance of a particle in the detector. There are a number of remaining events with very short pathlengths, which generally hit one corner with one or more tanks in either the center or bottom face and one or more in a vertical face. The vertical separation is often too short to produce a streamer tube trigger, which requires that at least six layers of streamer tubes fire, but some do have streamer tube triggers which do not seem to associate with the scintillator hits.

These events are possibly muon-induced showers, but the lack of streamer tube information makes it hard to see their structure. Another factor which predisposes the selection of these events is that there tends to be at least one vertical box hit, and since particles have longer pathlengths inside the vertical tanks than horizontal tanks, the 120 MeV energy cut is not as stringent for vertical tanks as it is for horizontal tanks.

There is insufficient available information to completely identify such events. The pathlength cut, requiring the vertical separation among the ERP hits to be greater than two meters, rejects them. Choosing the vertical separation instead of pathlength in the detector is because the detector is structured with horizontal layers and the streamer tube requires six layers to have a trigger. A total of 1,065 events survived this cut.

The pathlength cut does not affect either the trigger efficiency or the trigger sensitivity. However, a Monte Carlo simulation shows that it does reduce the total geometric acceptance by 15%, while reducing the remaining data sample by 40%.

6.2.4 The Track Matching Cut

Up to this stage, we have selected events which have the two largest energies from two different faces both greater than 120 MeV.* We now apply the tracking information to identify each possible candidate. If a track or tracks exist, we can determine a pair of scintillator tanks associated with the track. For the track matching cut, we find the pair of scintillator tanks associated with each streamer tube track, and we require that the energies in these two tanks must satisfy our requirement (120 MeV).

Because the tracking program does not work well for the events with showers, we only apply this cut to those events which have either just one track or parallel multiple tracks; for other events we still keep them in the data sample. Most single track and parallel multiple track events still have a few extra tank hits, which we have to consider. If the scintillator tanks which associate with tracks do not survive this cut, we look at the extra hits to determine whether their energies satisfy the energy requirement, which is two largest energies from different faces among these extra hits greater than 120 MeV.

For single track events which have one track from wire view and one from strips, we determine the associated tanks using both track parameters. To avoid mistakes, the two adjacent tanks (one if the tank at the edge of the detector) are also counted, and the largest energy deposited in any of these three tanks is defined to be the energy associated with the track.

For multiple track events, however, it is much more difficult to determine which strip track is associated with which wire track. For multiple track events, therefore, this cut is applied only to the clearly reconstructed parallel multiple track events for which the tracking information is reliable. We apply the following requirements to define clearly reconstructed parallel multiple track events:

---

*The WFD cut increases the minimum energy up to 180 MeV for some events, but in most cases the minimum energy is still 120 MeV.

1. The number of tracks in both the wire view and the strip view must be more than two, and
2. These tracks must be parallel; that is the difference between each track slope and the mean slope must be less than 10%.

The track matching cut requires that the energy deposited at both ends of the track must be greater than 120 MeV. For those events clearly having two or more muons striking the same pair of tanks, we subtract the mean muon energy for each extra track and determine whether the remainder exceeds the 120 MeV energy requirement or not. Those events which have no track information are still kept. A total of 463 events survived this cut.

This cut affects only those events with clear tracking, but these tracks are never required. Consequently, this cut does not affect the acceptance. It is possible for inaccurate tracking to point to the wrong scintillator tanks (if the angle in streamer tube is off by more than 6°), but with the careful track selection procedure which we used, the efficiency for fast monopoles candidates is not changed after this cut.

6.2.5 The Energy Cut

In general, the events which survive the above cuts can be classified into three groups—potential fast monopole events, muon induced shower events, and multiple muon events which include collateral hits (δ rays) so that the track information is not good enough to invoke the track matching cut. There are an additional few events for which our software fails to reconstruct tracks even though the events look like multiple muon events.

There are several events with no streamer tube information, only scintillator information. It is not clear whether these events were the results of the streamer tubes inefficiency. Due to the lack of streamer tube information, we can only use the scintillator hits to identify any possible monopole candidate with these events. In order to be conservative, we require the pathlength in each scintillator tank to be greater than 10 cm, which is equivalent to approximately 600 MeV for a fast moving monopole with a speed of $10^{-2}c$, which is the lowest light yield of equivalent energy to be expected for the fast monopole candidates. Therefore, we apply a higher energy cut.

This energy cut is similar to the primary event selection, but uses the ERP attenuated ADC rather than the ERP unattenuated ADC. We did not make this high energy cut at the primary event selection because the energy reconstruction at that stage was from the standard MACRO software and is only good for the lower energy. The high energy reconstruction is applied only to those events passing all previous cuts. Once again, the largest energy from a single tank in each face is used, and the event must have at least two faces, in each of which the largest energy must be greater than 600 MeV.

A total of 85 events survive this cut. This cut does not change the trigger sensitivity because the energy reconstruction is good at this level, but the 10 cm pathlength requirement reduces the total acceptance by 8%.

6.2.6 Summary of Cuts

We have applied five different physics cuts to the event sample, reducing the total number from 14,424 to 85. Table 6.2 summarizes.

The laser cut eliminates spontaneously triggering laser events from the data sample, and does not affect the trigger efficiency. The WFD saturation cut eliminates those events whose large energy deposition is likely caused by a secondary parti-

CUT	Rejected	Survived	Retained	Acceptance	Efficiency
Primary Selection	—	14,424	100%	100%	100%
Laser	1649	12775	88.5%	100%	100%
WFD	11732	2477	17.2%	99%	95.2%
Pathlength	1412	1065	7.4%	84%	95.2%
Track Matching	602	463	3.2%	84%	95.2%
Energy	378	85	0.6%	76%	95.2%

Table 6.2: Summary of physics cuts.

cle, producing a wide but unsaturated pulse. The WFD cut does raise the energy threshold somewhat. It only marginally reduces the acceptance, but it does affect the efficiency because of WFD cabling problems. The pathlength cut rejects corner clipping events and reduces the acceptance by 15%, generally for near horizontal crossings. The track match cut rejects both single track and multiple muon events for which the two tanks with the largest energy deposition are not associated with the same track. This cut does not affect the acceptance or efficiency because tracks are never required. The 10 cm pathlength in scintillator tank requirement raises the energy threshold to 600 MeV, which is very high for muons and even for some showers. This high energy threshold, however, is fine for fast monopoles and well within the attenuated ADC calibration range. This cut reduces the acceptance by 8%, but does not change the efficiency. The 85 remaining events include multiple muon events, large showers, and possible monopole candidates.

6.3 Visual Scanning

The remaining 85 events were visually scanned. No single track monopole candidate was observed. All remaining candidates have multiple hits in the scintillator tanks, the streamer tubes, and the strips; some have multiple tracks. Monopoles could, however, possibly be found within these events because monopoles with relativistic velocities can induce showers.

Of these 85 events, 65 are identified as potential monopoles accompanied by large showers and the other 20 as potential monopoles within multiple track events. For the 65 events with showers, visual scanning identified 26 of them that had clipped the corner of the detector with vertical pathlengths less than two meters. They survived the pathlength cut, however, because they contain extra hits which confused the pathlength calculation. They were rejected, as were another 12 events in which the two highest energy tanks did not match the shower direction as determined by the streamer tube hits.

Of the 20 with multiple tracks, 13 were rejected because the two largest energy tanks (from two separate faces) did not associate with the same track or because their large energies were due to muons traveling along the tanks. Although the tracking program did not work well for these events, the streamer tube and strip hits were adequate to allow us to identify tracks by eye. One multiple tracks event was rejected because, after the average muon energy (34.5 MeV) corresponding to each visually determined track was subtracted, the remaining maximum energies no longer satisfied the 600 MeV requirement. Table 6.3 shows the summary of visually scanned 85 events.

Corner clipping	Shower events	Multiple muons	Reminder
26	12	14	33

Table 6.3: Summary of the visual scanned 85 events.

The remaining 33 events, the final sample of possible fast monopole candidates, are listed in Table 6.4 with information such as pathlength in the detector and time of flight (TOF). All reconstructed energies are shown with errors, which are less than 7% at 1 GeV or less, and less than 10% at about 2 GeV. Because the ERP energy calibration limit is about 8 GeV in worst case, however, the error on the energy beyond this is unknown. Event 961 of run 6162 is the only one which reaches this calibration limit in one face.

All of these 33 events include large showers and seven are also accompanied by multiple tracks. These showers are so large that every streamer tube within a two meter or larger region around the core was fired, and the TDC's indicate that all their velocities are larger than $0.5c$. As an example, event 15,243 in run 6259 has a width of approximately six meters on the top of the center face around tank 6C04, close to the west side, and a diameter of about three meters on the bottom face near 6B03 (Figure 6.3). In the center region nearly every streamer tube and strip is triggered. Note that the event display represents a group of adjacent hits with one mark, so that in Figure 6.3 the several dots in the center of the shower actually represent many hits; the one dot on the top of the center face between 6C04 and 6C05 actually represents all 200 streamer tube cells in a six meter wide region.

To find fast monopoles within these multiple hit events, we compare the energy deposition with that expected for monopoles (the energy deposition should be at least as large as a lone monopole if there is any monopole within them). We again use the largest reconstructed energy from a single tank in each face, and define the two largest energies from different faces as those which the candidate passes through.

Figure 6.4 shows the distribution of these two maximum energies. It also shows the ERP energy calibration limit boundary, which is 8 GeV in the worst case. The minimum scintillation light yield produced by a magnetic monopole with velocity greater than $0.5c$ is at least 16 GeV. Fast monopole candidates should be at the (8 GeV, 8 GeV) point, or higher for tanks with higher calibration limits. All events in Figure 6.4 are clearly outside the expected monopole region.

RUN	EVT	PATH (cm)	TOF (ns)	β	ENE I (MeV)	ENE II (MeV)	TANK I	TANK II
5574	7815	580	26	0.74	1967 ± 200	1196 ± 59	4B11	4C15
5595	6891	300	10	1.0	872 ± 44	776 ± 39	4B10	4W04
5605	6536	460	13	1.15	1350 ± 65	940 ± 45	3C08	3B08
5630	3703	400	19	0.74	743 ± 37	625 ± 31	4B05	4W06
5656	8104	500	30	0.55	1552 ± 110	1405 ± 100	4C10	4B12
5668	9103	280	8	1.2	1920 ± 380	978 ± 49	4B14	4E05
5818	7792	430	25	0.6	2764 ± 320	1094 ± 75	6C08	6E02
5829	68	490	19	0.85	1681 ± 120	699 ± 35	4C05	4B07
5832	8853	280	12	0.80	1160 ± 55	920 ± 45	2C11	2W02
5897	11953	375	12	1.04	1255 ± 63	1080 ± 54	3C10	3W04
5856	9273	560	28	0.7	2184 ± 200	1056 ± 70	4C05	4B07
5933	13585	970	36	0.9	1253 ± 80	603 ± 30	2C09	2B11
5998	6876	480	20	0.8	806 ± 40	661 ± 33	1C16	2B01
6013	16534	725	18	1.32	1070 ± 54	870 ± 44	3C07	3B06
6014	6999	475	22	0.73	1650 ± 83	1430 ± 70	5B08	5C08
6017	14388	285	16	0.60	2640 ± 290	1810 ± 145	6C14	6E04
6032	7123	420	16	0.9	2741 ± 270	1000 ± 70	4W07	4B10

(Continued)

(Continued)

RUN	EVT	PATH (cm)	TOF (ns)	β	ENE I (MeV)	ENE II (MeV)	TANK I	TANK II
6039	6787	485	25	0.65	2290 ± 250	2110 ± 240	1C04	1B04
6061	10190	550	20	0.92	1183 ± 83	1135 ± 80	4B10	4C13
6084	7994	530	13	1.37	2880 ± 430	1650 ± 130	6C09	6B08
6089	1066	370	11	1.1	3853 ± 550	1370 ± 90	4E05	4B14
6091	1769	420	16	0.88	2537 ± 500	1348 ± 95	2B06	2E06
6116	9928	260	15	0.59	1010 ± 60	810 ± 41	3E04	3C10
6121	12195	570	30	0.65	2548 ± 500	725 ± 35	2C07	2B11
6162	961	280	7	1.11	$8^{+\infty}_{-2.0}$GeV	741 ± 37	3E04	3C12
6202	4101	480	14	1.16	674 ± 34	635 ± 32	5B08	5C10
6203	12870	540	18	1.00	208 ± 102	820 ± 41	6C07	6B03
6209	8832	340	7	1.64	1020 ± 51	610 ± 25	5W04	5C06
6244	14621	515	22	0.78	910 ± 45	720 ± 36	3C11	3B09
6249	14105	780	28	1.00	3170 ± 350	2210 ± 260	1C10	1B02
6255	666	715	24	0.99	3640 ± 540	2130 ± 305	6B16	6C15
6259	15243	480	25	0.64	2730 ± 410	800 ± 40	6C04	6B03
6266	3617	300	15	0.67	1130 ± 60	1090 ± 55	4C11	4E04

Table 6.4: A list of the 33 events remaining after cuts. EVT is the event number, and ENE I and ENE II are the energies corresponding to TANK I and TANK II.

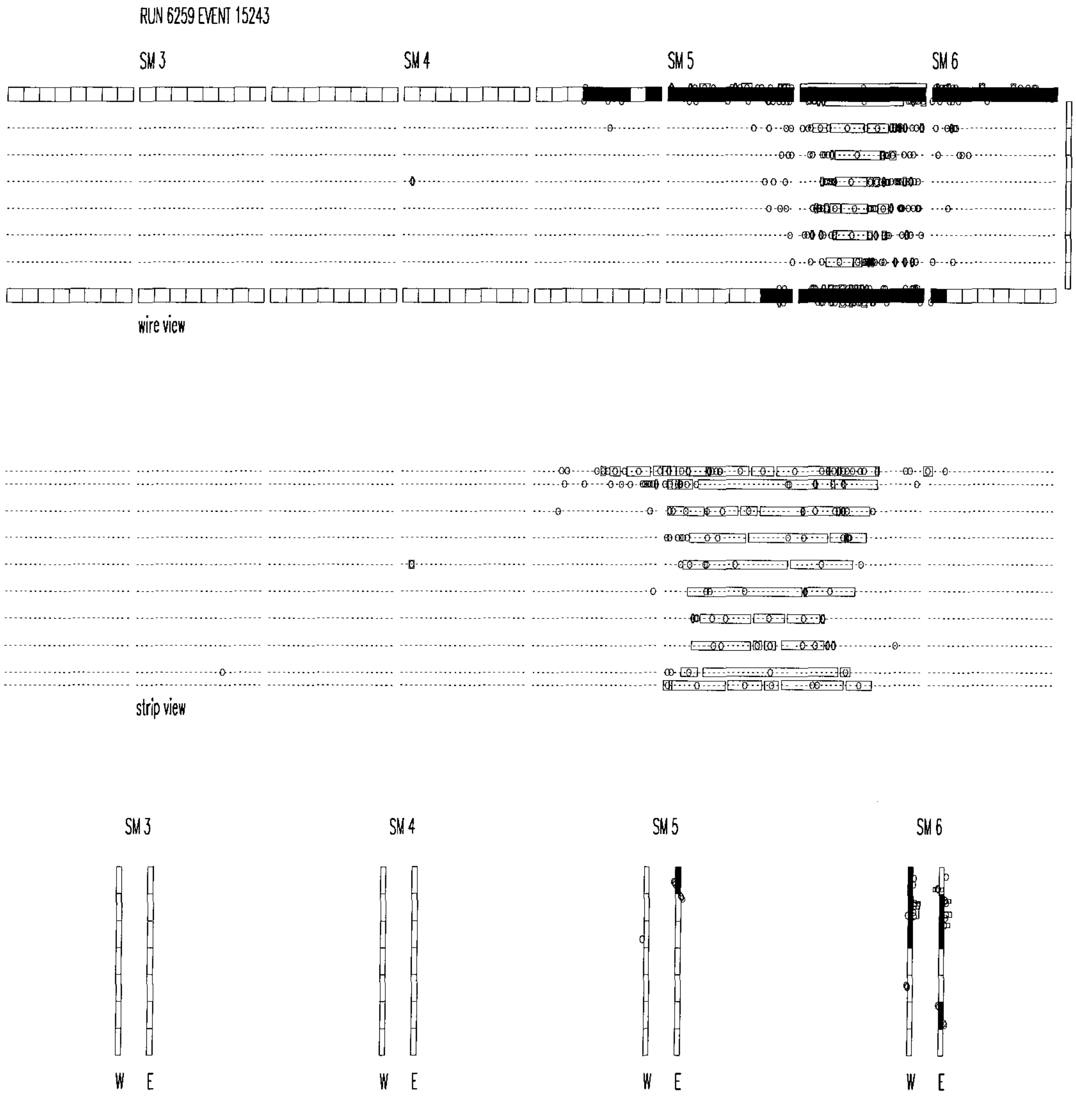

Figure 6.3: An example of a shower event, run 6,259 event 15,243.

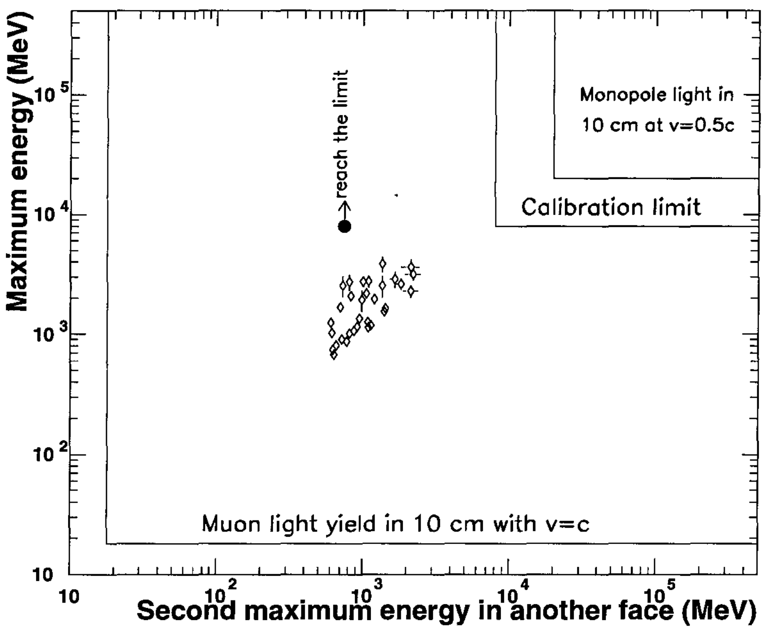

Figure 6.4: Distribution of the two maximum energies from two different faces for the remaining 33 events.

We require that each event must have reconstructed energy in two independent faces at or above the ERP calibration limit, which is less than the expected monopole energy deposition, to qualify as a candidate. This double-face requirement considerably suppresses the background events from muon showers, which can generate a number of energetic secondary electrons and gammas which confuse the event reconstruction. As we mentioned above, one event has an extremely large energy deposited in one tank of the east face while the largest energy deposited in the center face is much less (Figure 6.5). It hits the center face in SM3 around tank 3C11 with a zenith angle of about 10°, and proceeds down to the center of the east face around 3E04. The waveform (the sum of all signals from that side of the entire face) is completely saturated on both sides of the east face (Figure 6.6) for about 170 ns. The waveform of the center face, however, has a small but long tail consistent with the shower hypothesis. The ERP reconstructed energy from 3E04 reaches the laser calibration limit at 8 GeV, but the reconstructed energy is only about 740 MeV in

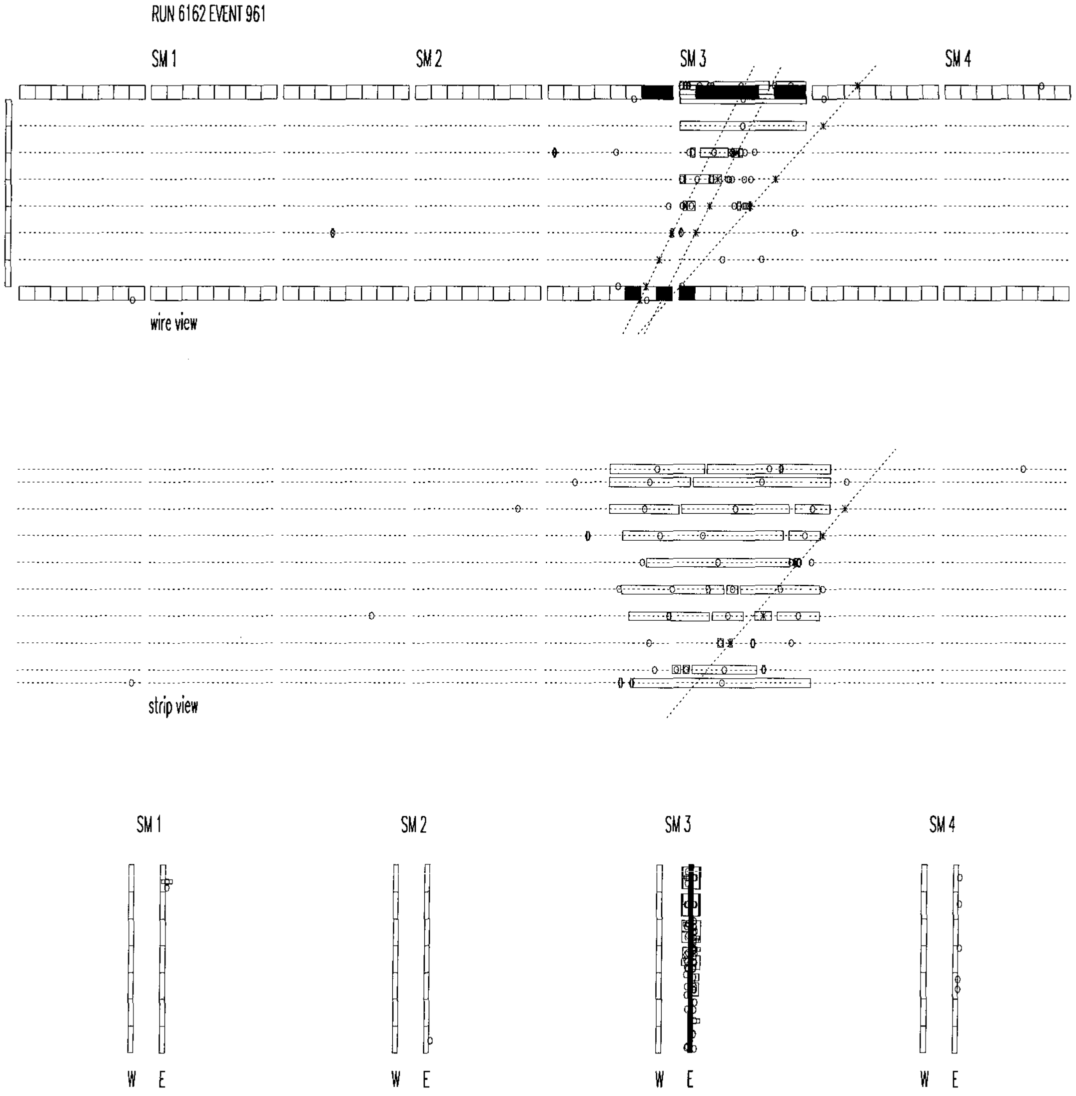

Figure 6.5: The event display for a shower from run 6261. Almost every single streamer tube cell fired in a six meter wide region around tank 3C12. The shower continues to be at least two meters wide all the way down to the east face. On the top two layers, scintillator tanks 3C07 to 3C16 fired. Tanks 3C09, 3C14, and 3B07 were not in operation at the time of this run.

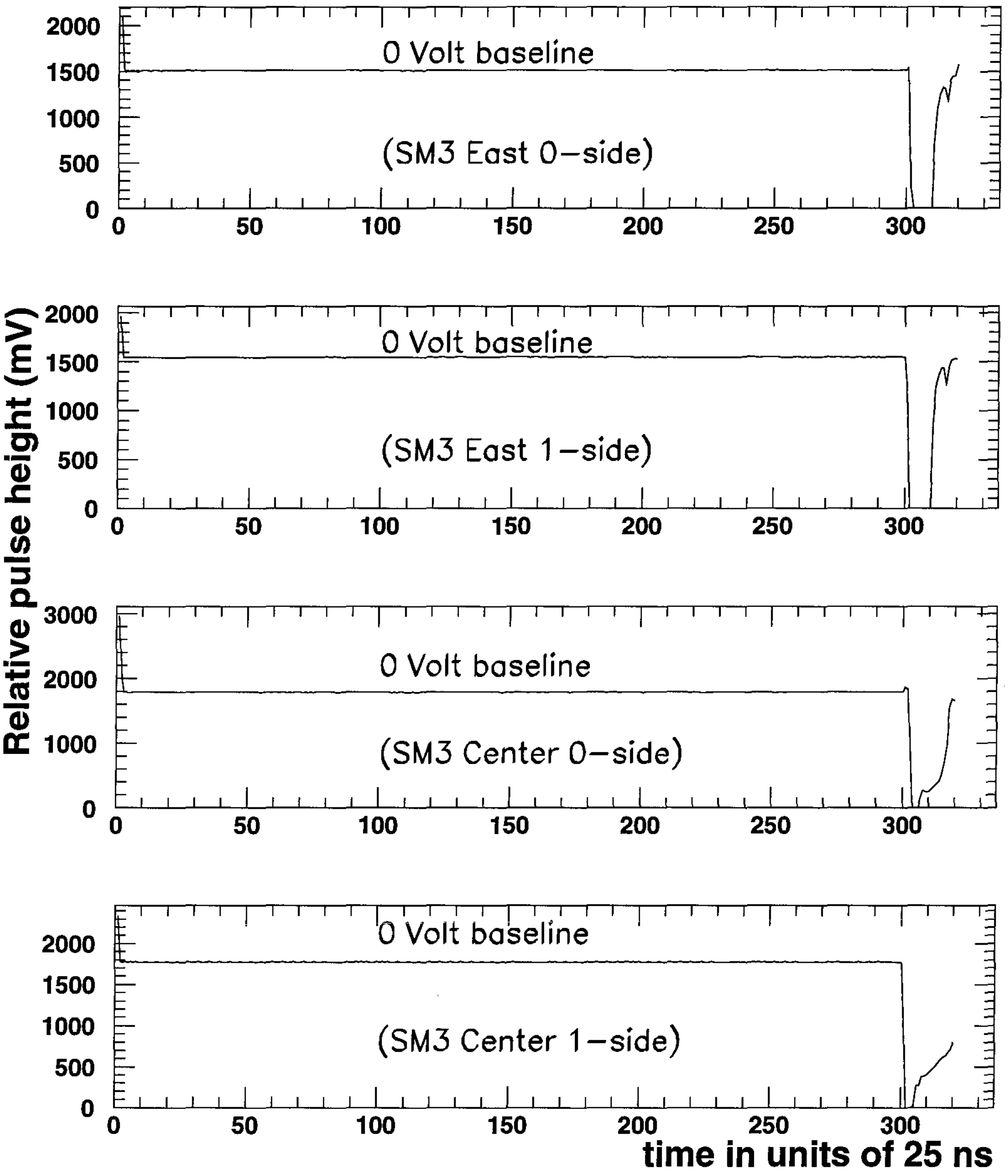

Figure 6.6: The waveforms of event 961 in run 6162. The signals from both sides of the east face are saturated as the upper two waveforms show. The lower two waveforms, from the center face, show a long low tail consistent with a shower spreading over several meters in the center face, with some lower speed particles producing late scintillation light. The waveform tails are cut off in the center face because the WFD is stopped by the CSPAM trigger at about 500 ns after the leading edge of the signal.

tank 3C11. We reject this event because the center face information is inconsistent with the expected light of a relativistic monopole.

In Figure 6.7 and 6.8, we plot the energy vs relative velocity for the 33 events. The relative monopole light yield is calculated for a pathlength of 10 cm in MACRO scintillator. All these events have energies which are one-third or less of the energy calibration limit, and of the expected equivalent monopole minimum light yield, except that one event with energy in one face reaches the energy calibration limit. As mentioned above, to be conservative, we require that an event must have energies on both faces to satisfy the energy requirement to be a monopole candidate. The normal time resolution in this region is 0.5 ns; due to showers, however, the timing from each tank can have an error up by 30 ns which corresponds to the light transfer in six meters which is the shower size in the scintillator.

Figure 6.7 and 6.8 assumes that monopole-induced showers require relativistic velocity. For such a monopole passing through the scintillator, our monopole light yield requirement is correct. If a slow moving monopole could produce such large showers, however, the timing reconstruction would actually be for the showers, which progress at nearly the speed of light, not for the monopole. So if a monopole with velocity of $10^{-2}c$ could induce large showers, we would probably misidentify it.

It can be shown, however, that it is unlikely for a non-relativistic monopole ($10^{-2}c < 0.5c$) to generate large showers in the MACRO detector. Considering monopole interactions in media, we know that there are two ways to produce secondary particles. One is through the classical electromagnetic interaction, and the other (for GUT monopoles) is through monopole catalysis of proton decay. Neither should produce large showers accompanying a monopole with velocity of $10^{-2}c$ because, on one hand, it is impossible for a low speed monopole to generate showers through elastic collision because the secondary particles have maximum energy of $2mc^2\beta^2\gamma^2$, and, on the other hand, the theoretical probability that monopole catalysis of pro-

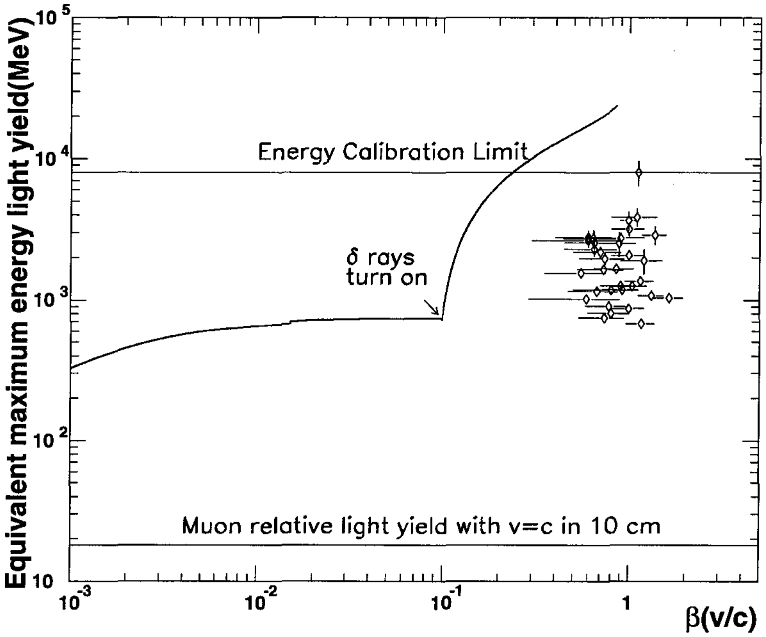

Figure 6.7: The maximum energy equivalent of the relative light yield of the 33 surviving events vs β.

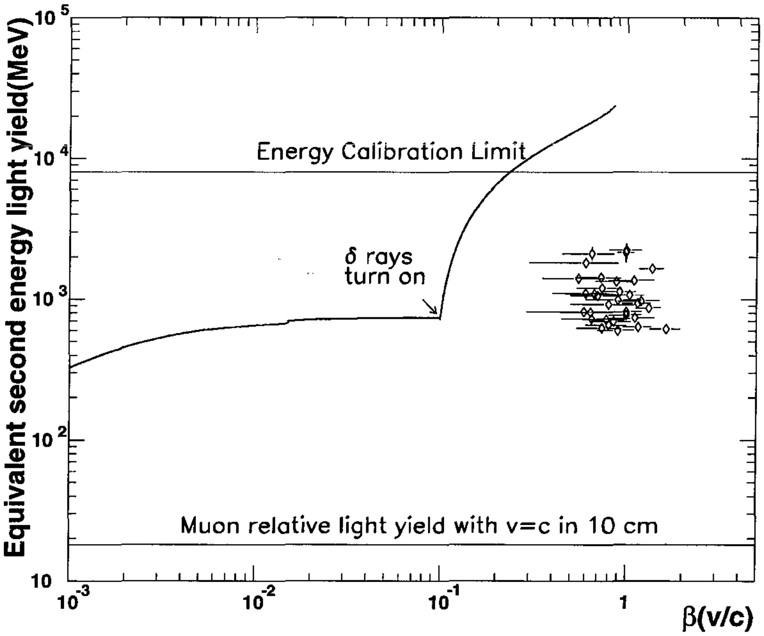

Figure 6.8: The second maximum energy equivalent of the relative light yield of the 33 surviving events vs β.

ton decay [82] produces such large showers in MACRO is less than 10^{-10}. For a monopole with a speed of $0.1c$, the calculated mean free path between two successive monopole-induced proton decays according to current theoretical cross-sections ($\sigma \sim \sigma_{strong} \sim 4 \times 10^{-26}$ cm^2) is about 70 meters in the scintillator oil and about 14 meters in the MACRO absorber. This is longer if the velocity is larger. Therefore, with a pathlength of several meters, as for the surviving 33 events, the large showers are not expected to be generated by any monopole with velocity between $10^{-2}c$ and 0.5c. Figure 6.8 has shown that the equivalent energy light yield of this event is less than the expected light yield for monopoles with velocities greater than $0.5c$.

In conclusion, we find no fast moving magnetic monopole candidate in the velocity range from $10^{-2}c$ to $1.0c$ during the "six-month-run" using the lower part of the MACRO detector. (Because of no monopole candidate, the track-etch has not been used.)

6.4 Acceptance and Flux Limit

To convert our fast moving magnetic monopole search result into a monopole flux limit, we need to calculate the acceptance of the detector. The acceptances for two, four, and all six SM's need to be calculated separately in order to use runs which may have one, two, or three μVAXes in operation. This acceptance is calculated through a Monte Carlo simulation which takes into account the real geometry of the MACRO detector.

The Monte Carlo simulates the trajectory of each event isotropically traversing the MACRO detector because the earth should have no stopping power for these heavy monopoles. It then applies all the requirements used in this analysis.

SM's	1	2	4	6
acceptance (m^2sr)	540	1210	2620	4050

Table 6.5: Detector acceptances

We also eliminate those tanks which were not operational during the "six-month-run" period. We obtain the acceptances in Table 6.5 with 1% error. These are calculated for monopole velocities greater than $10^{-2}c$. In the Monte Carlo simulation, however, we do not take the velocity into account because the acceptance is constant for $v \geq 10^{-2}c$. For monopole candidates with velocities less than $10^{-2}c$, the results are presented elsewhere [58].

Number of runs	Number of SM's	Acceptance (m^2sr)	Total run time (hour)	Total live time (hour)
9	One SM	540	5.94	5.9
61	Two adjacent SM's	1210	313.6	310.4
35	Four adjacent SM's	2620	105.5	104.4
11	Four separate SM's	2560	5.7	5.6
570	All six SM's	4050	5080.6	5029.8

Table 6.6: The list of live times for all 673 runs of the "six-month-run."

The live time of each run is calculated by subtracting the computer busy time from the run duration. For normal runs, the duration is the UTC (Universal Time Clock) time difference between the beginning and the end of the run. For those runs which ended abnormally, the UTC time of the last event is used. The computer busy time is less than 1% when all six SM's are in operation, but to be conservative, we subtract this maximum of 1% from every run duration. Because the acceptance is different for runs with a different number of SM's in operation, we list the live time in Table 6.6 according to geometry for the 673 total runs. The total exposure is the sum of the acceptance and live time products, or 7.6 × 10^{14} cm^{2}sr s.

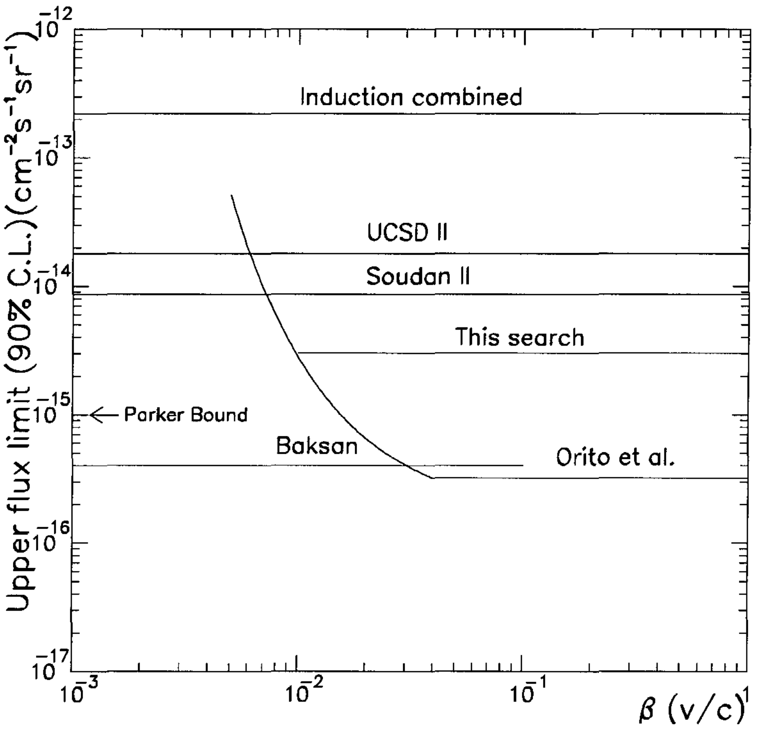

Figure 6.9: Upper flux limits (at 90% confidence levels) for fast moving magnetic monopoles searches from other experiments. Among these results, UCSD II [42] (He—CH_4) and Soudan II [43] (Ar—CO_2) are gaseous type detectors while the Baksan [41] experiment is a scintillator detector. Orito *et al.* [49] obtained their result using a CR-39 track-etch detector, and the induction (combined) result is from reference [32]. The result of this analysis is for the fast monopole with $\beta \geq 10^{-2}c$.

The probability of seeing at least one event is 90%, according to the Poisson statistics, if the expected number of events is 2.3. So, with no candidate, we establish an upper flux limit for the fast moving magnetic monopole at the 90% confidence level by dividing 2.3 by the aforementioned total acceptance live time product. The resultant flux limit is 3.03 × 10^{-15} cm^{-2} sr^{-1} s^{-1} for fast moving monopoles with velocities from $10^{-2}c$ to $1.0c$. Figure 6.9 shows the current flux limits from other experiments.

Chapter 7

Conclusion

"There is little reason to doubt that further surprising discoveries await the dedicated student of the magnetic monopole."

— John Preskill

MACRO is a large underground detector at 3,000 meters water equivalent depth with a nominal acceptance of 10,000 m^2sr, located at the Gran Sasso, in central Italy. Its primary goal is to search for magnetic monopoles at a flux level beyond the Parker bound. It employs liquid scintillator counters, streamer tubes and track-etch detectors which can supply good independent and cross check for fast monopole events. This search is mainly based on the liquid scintillator system with primary event selection and energy reconstruction from the ERP system. The 6.2 μs trigger time is based on the time of flight of a fast moving monopole through one supermodule diagonally with a velocity $\sim 10^{-2}c$. The search uses the "six-month-run" data which were taken from December 10, 1992, to July 1, 1993, with the operation of the lower part of the full detector. With good energy reconstruction ability, we apply a double-face high energy requirement to reject most muon events from the data sample, then apply WFD, streamer tube and strip information to reject non-monopole events.

The live time of this analysis is 5,300 hours, and the acceptance is 4050 m^2sr. With no candidate event found, we establish an upper flux limit for the fast moving magnetic monopole at 90% confidence level of 3.03×10^{-15} $cm^{-2}sr^{-1}s^{-1}$ for velocities from $10^{-2}c$ to $1.0c$.

Appendix A

Scintillation Light From δ Rays

The total scintillation light of high ionization particles is described with the following formula: [78]

$$(\frac{dL}{dX})_t = (\frac{dL}{dX})_p + (\frac{dL}{dX})_\delta, \tag{A.1}$$

where $(\frac{dL}{dX})_t$ = the total scintillation light,
$(\frac{dL}{dX})_p$ = the scintillation light due to the primary particle, and
$(\frac{dL}{dX})_\delta$ = the scintillation light due to δ rays.

This formula counts on the contribution of the δ rays produced by the primary particle. The total light emitted per unit length is considered as the sum of two contributions: one from primary particle; and one from those energetic δ rays which escape the saturation column and produce light with high efficiency. The δ rays produce light with high efficiency and without saturation because their ionization energy loss rate is low. Thus, $(dL/dX)_\delta$ is just proportional to the δ rays energy, and $(dL/dX)_p$ can be calculated from the Birks' formula discussed in Section 3.2.

The radius of the saturation column is proportional to the impact parameter. For a relativistic particle with the velocity greater than the electron orbital speed ($\sim \alpha c$), the adiabatic impact parameter [83] b_0 is

$$b_0 \sim \beta\gamma c\tau, \tag{A.2}$$

where $\beta =$ the relative speed,
$\gamma = 1/\sqrt{1-\beta^2}$, and
$\tau =$ the collision time.

As long as the impact parameter less than b_0 [74], electron can receive energy from projectile. For the impact parameter larger than b_0, electrons will only be perturbed but not excited. For hydrogen, the collision time is approximately $2\pi a_0/(\alpha c)$, where a_0 is the Bohr's radius, and thus, b_0 is about $137\beta\gamma a_0$. For MACRO liquid scintillator, delocalized π electrons are along a benzenoid ring with the circumference of about $10\mathring{A}$, and the b_0 will be four times that of hydrogen. For the velocity less than electron orbital speed, the δ rays are insignificant.

Considering that the saturation column is where all the π electrons are excited or ionized, we know for MACRO scintillator, this maximum number of photons at the saturation region will be about 5×10^5 per cm. The total π electrons inside the adiabatic impact parameter volume for $\beta \sim 0.1$ is, however, several orders of magnitude higher than those being excited or ionized. Hence, the adiabatic impact parameter is bigger than the saturation column radius. Using data from Reference [84], we can calculate the range of 10 KeV electron in MACRO scintillator of about 1.7 μm which is about two orders of magnitude larger than the saturation radius. Hence, δ rays with energies larger than 10 KeV will have no problem to escape the column.

The calculation of the fast monopole light yield has taken care of the δ rays with energies greater than 10 KeV, and these δ rays must have an angle greater than 10° from the direction of the incident monopole trajectory. Clearly, it can escape from the saturation column, and converts almost all the energy into the scintillation light with its nonsaturation efficiency. It is hard to estimate the error of this calculation, but we have employed very conservative requirements in order not to overestimate.

Appendix B

The MACRO Laser Calibration

Each MACRO supermodule has one laser attenuator for the lower part of the detector from which light is conducted though laser fibers to the scintillator counters. The amount of light delivered to the scintillators can be controlled from near zero to tens of times the muon light yield. In this appendix, we will discuss the ERP ADC response to this laser calibration system.

B.1 The Laser Attenuator

To obtain a series of laser light levels, MACRO employs optical attenuators. Each has 4,000 steps, numbered from 0 to 4,000, with the light output doubling every 100 steps. Below 500, the light level is too low to trigger our electronics. Figure B.1 shows the relative light yield as a function of attenuator step, following a very good power law function from attenuation steps 600 through 3,600, over which range the total amount of light changes by about eight orders of magnitude. The amount of light at around step 2,600 is equivalent to the light produced by a typical muon in a horizontal tank (Figure B.1).

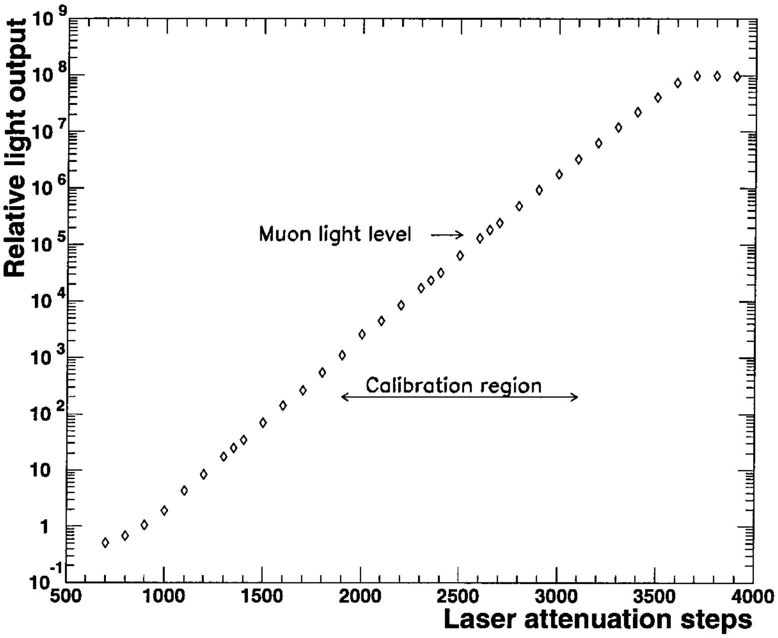

Figure B.1: The relative light as a function of laser attenuator steps.

During weekly calibrations, the laser attenuator setting is varied from about 2,000 to 3,100 in every 50 unit steps. The corresponding light level changes from a quarter to about 60 times the muon light yield in a horizontal tank. The laser is triggered about 150 times at each attenuation setting.

B.2 ERP ADC Response

Since the ERP is triggered by the input signal itself, there is no signal until the light level is high enough to exceed the trigger threshold, and for levels near threshold, the laser does not trigger with 100% efficiency. Figure B.2 shows the number of laser events at different attenuator setting for the first scintillator counter of the bottom face of SM5 (box number 401). At the attenuator step 2,350, the trigger efficiency is only about 40%. Only those settings with greater than 95% trigger efficiency are used for calibrations.

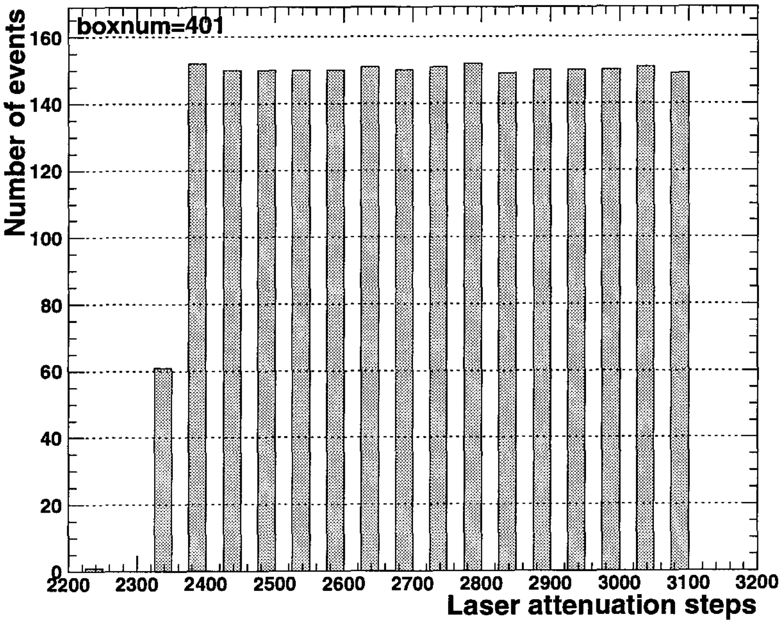

Figure B.2: The number of events for each attenuator setting. The laser has fixed 150 triggers.

Typically, ERP ADC values have a linear response to laser light until the ADC saturates, which occurs before the PMT itself begins to respond nonlinearly. Figure B.3 shows the mean ERP ADC value vs laser attenuation setting. Since the total amount of light varies as a power law of the attenuator setting, we show the ADC value in Figure B.3 on a logarithmic scale.

Figure B.3 shows clearly that the ADC values are linear until saturation at 4,095, the maximum value of the 12-bit ADC. Extrapolating the linear part of the ERP ADC response to zero light input gives the ADC pedestal for each channel.

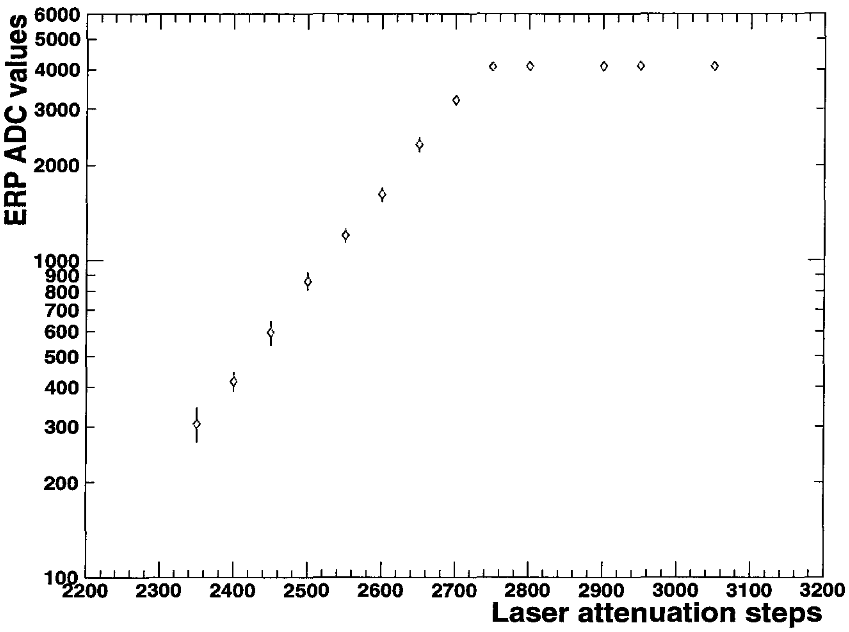

Figure B.3: The ERP ADC value as a function of laser attenuator settings.

B.3 ERP Attenuated ADC Response

As we mentioned in Chapter 4, the ERP provides both unattenuated and attenuated ADC values. The attenuation factor is approximately 10. If we look at the attenuated ADC for the laser light levels shown above (Figure B.3), we see new behavior. At light levels less than three time the level produced by typical muons in horizontal tanks, the ERP attenuated ADC is approximately a linear function of the light level. As the total light increases, however, the attenuated ADC value becomes nonlinear, reflecting the PMT nonlinear response (Figure B.4)

In order to see the nonlinear behavior more clearly, we plot in Figure B.5 the relative light output on a linear scale by converting the laser attenuator steps as follows:

$$\langle Output \rangle = C_0 \; 2^{\langle steps \rangle / 100}, \tag{B.1}$$

where C_0 = an arbitrary scale factor .

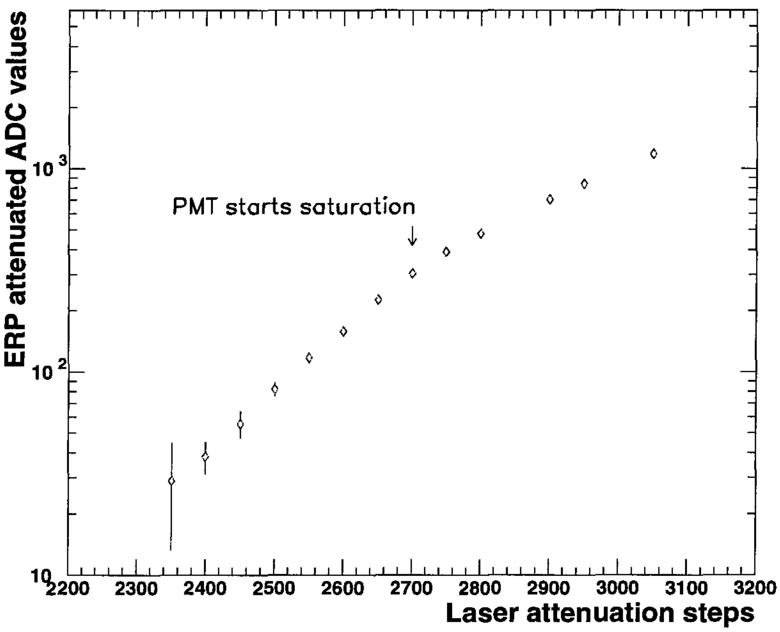

Figure B.4: The ERP attenuated ADC value as a function of laser attenuator settings.

We fit the first five data points with a linear function to obtain the pedestal and gain of the attenuated ADC for each ERP channel. We then fit the rest of the data points with a quadratic function in order to correct for saturation of the PMT's.

The ERP attenuated ADC calibration data used in this thesis do not reach their maximum limit; rather, the calibration has been performed up to the hardware limit, caused by PMT pulse height saturation and the limited width of the ERP ADC integration gate. The PMT pulse height saturates at typically 4.5 V, but the width of the pulse continues to increase with the laser light beyond this point. Obviously, the change in width does not affect the ADC after it exceeds the width of the integration gate. For a typical horizontal tank, the largest possible ERP attenuated ADC value is around 1,800. In the future, the calibration using new waveform digitizer, which has 5 ns sampling resolution and 32 ms memory (using zero suppression), larger energies can be reconstructed possibly up to the theoretical fast monopole energy deposition in MACRO scintillator.

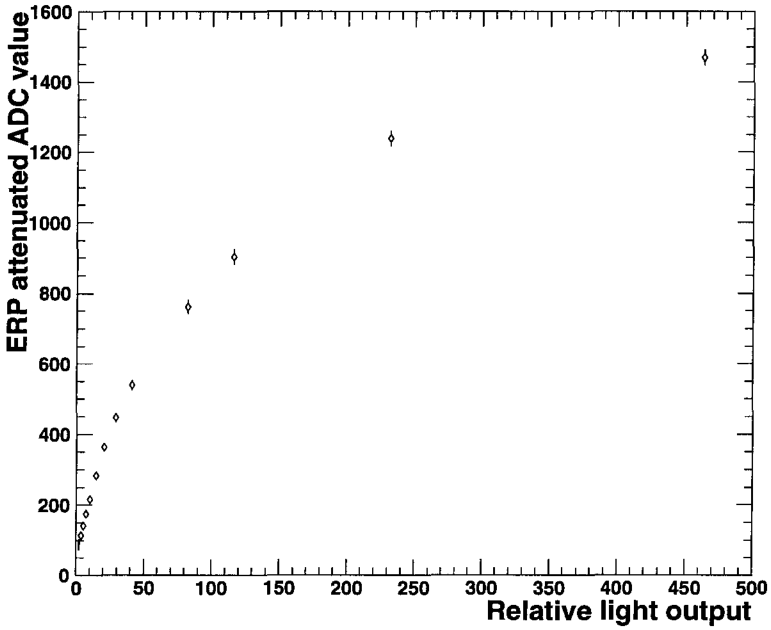

Figure B.5: The ERP attenuated ADC value as a function of laser attenuator settings.

Appendix C

The MACRO Collaboration

S. Ahlen,(3) M. Ambrosio,(12) R. Antolini,(4,7*) G. Auriemma,(14),(a) R. Baker,(11) A. Baldini,(13) B. B. Bam,(2) G. C. Barbarino,(12) B. C. Barish,(4) G. Battistoni,(6),(b) R. Bellotti,(1) C. Bemporad,(13) P. Bernardini,(10) H. Bilokon,(6) V. Bisi,(16) C. Bloise,(6) C. Bower,(8) S. Bussino,(14) F. Cafagna,(1) M. Calicchio,(1) D. Campana,(12) P. Campana,(6) M. Carboni,(6) S. Cecchini,(2),(c) F. Cei,(13) V. Chiarella,(6) R. Cormack,(3) A. Corona,(14) S. Coutu,(4),(11*) G. De Cataldo,(1) H. Dekhissi,(2),(d) C. De Marzo,(1) M. De Vincenzi,(14),(e) A. Di Credico,(9) E. Diehl,(11) O. Erriquez,(1) C. Favuzzi,(1) D. Ficenec,(3),(f) C. Forti,(6) P. Fusco,(1) G. Giacomelli,(2) G. Giannini,(13),(g) N. Giglietto,(1) P. Giubellino,(16) M. Grassi,(13) P. Green,(15,18*) A. Grillo,(6) F. Guarino,(12) P. Guarnaccia,(1) C. Gustavino,(7) A. Habig,(8) R. Heinz,(8) J. T. Hong,(3) E. Iarocci,(6),(h) E. Katsavounidis,(4) E. Kearns,(3) S. Klein,(3),(i) S. Kyriazopoulou,(4) E. Lamanna,(14) C. Lane,(5) C. Lee,(11) D. Levin,(3,11*) P. Lipari,(14) G. Liu,(4) R. Liu,(4) N. Longley,(4) M. J. Longo,(11) Y. Lu,(15) G. Ludlam,(3) G. Mancarella,(10) G. Mandrioli,(2) A. Margiotta-Neri,(2) A. Marin,(3) A. Marini,(6) D. Martello,(10) A. Marzari Chiesa,(16) M. Masera,(16) M. N. Mazziotta,(1) D. G. Michael,(4) S. Mikheyev,(7),(j) L. Miller,(8) M. Mittelbrunn,(5) P. Monacelli,(9) M. Monteno,(16) S. Mufson,(8) J. Musser,(8) D. Nicoló,(13) R. Nolty,(4)

S. Nutter,(8),(11*) C. Okada,(3) G. Osteria,(12) O. Palamara,(10) S. Parlati,(4,7*) V. Patera,(6) L. Patrizii,(2) B. Pavesi,(2) R. Pazzi,(13) C. W. Peck,(4) J. Petrakis,(8,17*) S. Petrera,(10) N. D. Pignatano,(4) P. Pistilli,(10) J. Reynoldson,(7) F. Ronga,(6) G. Sanzani,(2) A. Sanzgiri,(15) C. Satriano,(14),(a) L. Satta,(6),(h) E. Scapparone,(2) K. Scholberg,(4) A. Sciubba,(14),(h) P. Serra Lugaresi,(2) M. Severi,(14) M. Sitta,(16) P. Spinelli,(1) M. Spinetti,(6) M. Spurio,(2) J. Steele,(4),(5*) R. Steinberg,(5) J. L. Stone,(3) L. R. Sulak,(3) A. Surdo,(10) G. Tarlé,(11) V. Valente,(6) C. W. Walter,(4) R. Webb,(15) and W. Worstell.(3)

(1)Dipartimento di Fisica dell'Università di Bari
and Istituto Nazionale di Fisica Nucleare (INFN), Bari, 70126, Italy
(2)Dipartimento di Fisica dell'Università di Bologna and INFN, Bologna, 40126, Italy
(3)Physics Department, Boston University, Boston, Massachusetts 02215
(4)California Institute of Technology, Pasadena, California 91125
(5)Department of Physics, Drexel University, Philadelphia, Pennsylvania 19104
(6)Laboratori Nazionali di Frascati dell'INFN, Frascati (Roma), 00044, Italy
(7)Laboratori Nazionali del Gran Sasso dell'INFN, Assergi (L'Aquila), 67010, Italy
(8)Departments of Physics and of Astronomy, Indiana University, Bloomington, Indiana 47405
(9)Dipartimento di Fisica dell'Università dell'Aquila and INFN, L'Aquila, 67100, Italy
(10)Dipartimento di Fisica dell'Università di Lecce and INFN, Lecce, 73100, Italy
(11)Department of Physics, University of Michigan, Ann Arbor, Michigan 48109
(12)Dipartimento di Fisica dell'Università di Napoli and INFN, Napoli, 80125, Italy
(13)Dipartimento di Fisica dell'Università di Pisa and INFN, Pisa, 56010, Italy
(14)Dipartimento di Fisica dell'Università di Roma and INFN, Roma, 00185, Italy
(15)Physics Department, Texas A&M University, College Station, Texas 77843

(16)Dipartimento di Fisica dell'Università di Torino and INFN, Torino, 10125, Italy
(17)Bartol Research Institute, University of Delaware, Newark, Delaware 19716
(18)Sandia National Laboratory, Albuquerque, New Mexico 87185

* Current address
(a)Also at Università della Basilicata, Potenza, 85100, Italy
(b)Now at INFN, Milano, Italy
(c)Also at Istituto TESRE/CNR, Bologna, Italy
(d)Also at Faculty of Science, University Mohamed I, Oujda, Morocco
(e)Also at Università di Camerino, Camerino, Italy
(f)Now at Physics Department, Washington University, St. Louis, Missouri 63130
(g)Also at Università di Trieste and INFN, Trieste, 34100, Italy
(h)Also at Dipartimento di Energetica, Università di Roma, Roma, 00185, Italy
(i)Now at Department of Physics, University of California, Santa Cruz, California 95064
(j)Also at Institute for Nuclear Research, Russian Academy of Sciences, Moscow, Russia

Bibliography

[1] H. C. Oersted, "A Source Book in Physics" W. F. Magie, ed., Harvard University Press, Cambridge (1965) p. 437.

[2] A. M. Ampere, "A Source Book in Physics" W. F. Magie, ed., Harvard University Press, Cambridge (1965) p. 446.

[3] P. A. M. Dirac, *Proc. Roy. Soc.* **133**, 60 (1931).

[4] J. Preskill, *Ann. Rev. Nucl. Part. Sci.* **34**, 461 (1984).

[5] G.'t Hooft, *Nucl. Phys. B* **79,** 276 (1974).

[6] A. M. Polyakov, *JETP Lett.* **20**, 194 (1974).

[7] D. H. Perkins, *Introduction to High Energy Physics*, Addison-Wesley, 1986, p. 23.

[8] F. Halzen and A. D. Martin, *Quarks and Leptons*, John Wiley & Sons, New York, 1984.

[9] R. A. Carrigan, Jr., and W. P. Trower, ed., *Magnetic Monopoles*, Proceedings of a NATO Advanced Study Institute on Magnetic Monopoles, held October 14-17, 1982, in Wingspread, Wisconsin, Plenum Press, New York (1983).

[10] C. R. Dokos and T. N. Tomaras, *Phys. Rev. D* **21**, 2940 (1980).

[11] C. G. Callan, Jr., *Phys. Rev. D* **25** 2141 (1982); *Phys. Rev. D* **26** 2058 (1982).

[12] V. Robakov, *Nucl. Phys. B* **203** 311 (1982).

[13] E. W. Kolb and M. S. Turner, *The Early Universe*, Addison-Wesley Publishing (1990).

[14] T. W. B. Kibble, *J. Phys. A* **9** 1387 (1976).

[15] J. Preskill, *Phys. Rev. Lett.* **43** 1365 (1979).

[16] A. H. Guth, *Phys. Rev. D* **23** 347 (1981).

[17] K. A. Olive, *Phys. Reports* **190** 307 (1990).

[18] M. J. Longo, *Phys. Rev. D* **25** 2399 (1982).

[19] M. S. Turner, E. N. Parker, and T. J. Bogdan, *Phys. Rev. D* **26** 1296 (1982).

[20] D. E. Groom, *Phys. Reports* **140** (1986).

[21] S. L. Shapiro and S. A. Teukolsky, *Balck Holes, White dwarfs, and Neutron Stars,* Jon Wiley and Sons (1983).

[22] J. L. Stone, *Monopole '83*, Proceedings of a NATO Advanced Research Workshop entitled Monopole '83, held October 6-9, 1983, in Ann Arbor, Michgan, Plenum Press, New York (1984).

[23] J. D. Jackson, *Classical Electrodynamics,* John Wiley & Sons (1975).

[24] R. R. Ross, P. H. Eberhard, L. W. Alvarez, and R. D. Watt, *Phys. Rev. D.* **8** 698 (1973).

[25] P. B. Price, J. Guiru, and K. Kinoshita, *Phys. Rev. Lett.* **65** 143 (1990) p. 251.

[26] D. Fryberger, T. Coan, K. Kinoshita, and P. B. Price, *Phys. Rev. D.* **29** 1524 (1984).

[27] See, for example, K. Kinoshita, *Phys. Rev. D* **46** 881 (1992).

[28] B. Cabrera, M. Taber, R. Gardner, and J. Bourg, *Phys. Rev. Lett.* **51** 1933 (1983).

[29] C. D. Tesche, C. C. Chi, C. C. Tsuei, and P. Chaudhari, *Appl. Phys. Lett.* **43** 384 (1983).

[30] J. R. Incandela, M. Campbell, H. Frisch, S. Somalwar, M. Kuchnir, and H. R. Gustafson, *Phys. Rev. Lett.* **53** 2067 (1984).

[31] B. Cabrera, *Phys. Rev. Lett.* **48** 1378 (1982).

[32] S. Bermon *et al., Phys. Rev. Lett.* **64** 839 (1990); M. E. Huber *et al., Phys. Rev. Lett.* **64**, 835 (1990).

[33] S. D. Drell *et al., Phys. Rev. Lett.* **50** 644 (1983).

[34] See, for example, F. Kajino, S. Matsuno, Y. K. Yuan, and T. Kitamura, *Phys. Rev. Lett.* **52** 1373 (1983).

[35] E. N. Alexeyev, M. M. Boliev, A. E. Chudakov, and S. P. Mikheyev, *Proc, 21st Intern. Cosmic Ray Conf.* (Adelaide, 1990), edited by R. J. Protheroe, **v.10,** p.83.

[36] G. Tarlé, S. P. Ahlen, and T. M. Liss, *in Monopole '83* (ref[22]), p.551.

[37] P. Galeotti *et al., in Monopole '83* (ref[22]), p.561.

[38] R. I. Steinberg *et al., in Monopole '83* (ref[22]), p.567.

[39] R. C. Webb *et al., in Monopole '83* (ref[22]), p.581.

[40] B. C. Barish, G. Liu, and C. Lane, *Phys. Rev. D.* **36** 2641 (1987).

[41] Private communication with A. E. Chudakov.

[42] K. N. Buckland, G. E. Masek, L. M. Knapp, and J. P. Stronski, *Phys. Rev. D* **41** 2726 (1990).

[43] J. L. Thron *et al.* (Soudan 2 Collaboration), *Phys. Rev. D* **46** 4846 (1992).

[44] P. Eschstruth, *in Monopole '83*, (ref[22]), p. 611.

[45] R. L. Fleischer, P. B. Price, and R. M. Walker, *Nuclear Tracks in Solida*, University of California Press, Berkeley (1975).

[46] D. P. Snowden-Ifft and P. B. Price, *Phys. Lett. B* **288** 250 (1992).

[47] S. W. Burwick, K. Kinoshita, and P. B. Price *Phys. Rev. D* **28** 2338 (1983).

[48] T. Doke, *et al., Proc. 1983 int. Symp. on Lepton and Photon Interactions at High Energies,* Cornell University (1983).

[49] S. Orito, *et al., Phys. Rev. Lett.* **66** 1951 (1992).

[50] P. B. Price and M. H. Salamon, *Phys. Rev. Lett.* **56** 1226 (1986).

[51] D. Ghosh and S. Xhatterjea, *Europhys. Lett* **12** 25 (1990).

[52] S. Ahlen *et al.* (MACRO Collaboration), *Nucl. Instrum. & Methods* **324** 337 (1993).

[53] MACRO Collaboration, "MACRO Proposal" (1985).

[54] E. Bellotti, *Nucl. Instrum. & Methods* A 264 1 (1988).

[55] I. B. Berlman, *Handbook of Fluorescence Spectra of Aromatic Molecules,* 2nd ed. Academic Press (1971).

[56] G. Ludlam *et al.*, MACRO internal Memo 1012/93 (1993) (unpublished).

[57] S. Ahlen *et al.* (MACRO Collaboration), Astroparticle Phys. **1** 11 (1992).

[58] J. T. Hong, "Search for GUT Magnetic Monopoles," Ph.D. thesis, Caltech (1993).

[59] G. Auriemma *et al., Nucl. Instrum. & Methods* **263** 249 (1988).

[60] S. Ahlen *et al.* (MACRO Collaboration), *Phys. Rev. D* **46** 895 (1992).

[61] S. Ahlen *et al.* (MACRO Collaboration), *Phys. Rev. D* **46** 4836 (1992).

[62] S. Ahlen *et al.* (MACRO Collaboration), *Nucl. Phys. B* **370** 432 (1992).

[63] S. Ahlen *et al.* (MACRO Collaboration), *Astrophysical Journal* **412** 301 (1993).

[64] E. Diehl, *Limits on Neutralino Dark Matter by Search for Upward Muons in the* MACRO *Detector,* Ph.D. thesis.

[65] D. Michael *et al.* (MACRO Collaboration), *Nucl. Phys. B* (Proc. Suppl.), **35** 235 (1994).

[66] S. Ahlen *et al.* (MACRO Collaboration), *Phys. Rev. Lett.* **69** 1860 (1992).

[67] H. J. D. Cole, *Proc. Cambridge Philos. Soc.* **47** 196 (1951).

[68] E. Bauer, *Proc. Cambridge Philos. Soc.* **47** 777 (1951).

[69] V. P. Martim'yanov and S. Kh. Khakimov, *Sov. Phys. JETP* **25** 20 (1972).

[70] S. P. Ahlen, *Phys. Rev. D* **14** 2935 (1976).

[71] S. P. Ahlen, *Phys. Rev. D* **17** 229 (1978).

[72] U. Fano, *Ann. Rev. Nucl. Sci.* **13** 1 (1963).

[73] A. Crispin and G. N. Fowler, *Rev. Mod. Phys.* **42** 290 (1970).

[74] S. P. Ahlen and K. Kinoshita, *Phys. Rev. D* **26** 2347 (1982).

[75] E. Fermi and E. Teller, *Phys. Rev.* **72** 399 (1947).

[76] J. Lindhard, *Mat Fys. Medd. Dan. Vid. Selsk.* **28** No. 8 (1954).

[77] S. P. Ahlen and G. Tarlé, *Phys. Rev. D* **27** 688 (1983).

[78] J. B. Birks, *Proc. Phys. Soc. A* **64** 874 (1951).

[79] R. Liu, MACRO Inter Memo., 1018/93 (1993) (unpublished).

[80] C. Bloise, MACRO Internal Memo 8/91 (1991) (unpublished).

[81] M. Spurio, MACRO Internal Memo., 32/92 (1992) (unpublished).

[82] J. Ellis, D. V. Nanopoulos and K. A. Olive, "Baryon number violation catalyzed by Grand Unified Monopoles," Preprint TH 3383 CERN (1982).

[83] R. Rossi, "High-Energy Physics", 2nd Ed., Prentice-Hall Inc. (1956).

[84] W. Peter Trower, *et al.*, "High Energy Particle Data", UC Berkeley (1965-1966).